Crystal Growth and Magnetic Property Study of layered honeycomb materials with Kitaev-like interactions

Kavita Mehlawat

A thesis submitted for the partial fulfilment of the degree of Doctor of Philosophy

Indian Institute of Science Education and Research, Mohali

January 2018

Dedicated to my parents and my brother:
B.S. Mehlawat,
Manoj Mehlawat, and
Krishan Mehlawat

Certificate of Examination

This is to certify that the dissertation titled *"Crystal Growth and Magnetic Property Study of layered honeycomb materials with Kitaev-like interaction"* submitted by **Ms. Kavita Mehlawat** (Reg. No. Ph12136) for the partial fulfillment of Doctor of Philosophy programme of the Institute, has been examined by the thesis committee duly appointed by the Institute. The committee finds the work done by the candidate satisfactory and recommends that the report be accepted.

Dr. Sanjeev Kumar | Dr. Abhishek Chaudhuri | Dr. Yogesh Singh (Supervisor)

Declaration

The work presented in this dissertation has been carried out by me under the guidance of Dr. Yogesh Singh at the Indian Institute of Science Education and Research Mohali. This work has not been submitted in part or in full for a degree, a diploma, or a fellowship to any other university or institute. Whenever contributions of others are involved, every effort is made to indicate this clearly, with due acknowledgement of collaborative research and discussions. This thesis is a bonafide record of original work done by me and all sources listed within have been detailed in the bibliography.

Kavita Mehlawat

In my capacity as the supervisor of the candidates doctoral thesis, I certify that the above statements by the candidate are true to the best of my knowledge.

Dr. Yogesh Singh

(Supervisor)

Department of Physical Sciences

IISER Mohali

India

Abstract

Kitaev-like bond-directional exchange interactions are novel and quite different from the ubiquitous Heisenberg interactions found in most magnets. These kind of interactions open up new possibilities in the exploration and designing of new quantum magnets which can host novel quantum ground states like spin-liquids. However, Kitaev-like interactions have remained only a theoretical construct until recently. Honeycomb iridates A_2IrO_3 (A = Na, Li), offer potential realizations of such novel exchange coupling. In this thesis I have synthesized single crystals of A_2TO_3 (A = Na, Li, K, and T = Ir, Ru) and studied their electrical transport, magnetic, and thermal properties. Our work provides several new results: (i) the first thermodynamic evidence of possible fractionalization of electrons in Na_2IrO_3 because of proximity to the Kitaev spin-liquid state, (ii) evidence through magnetic impurity doping, of fragile magnetic order and importance of nearest-neighbour interactions and spin-orbit coupling in deciding the magnetic ground state in Na_2IrO_3, (iii) a novel method (reactive ion etching) of surface doping Na_2IrO_3 and possibly other layered oxides has been discovered. The surface conductivity of Na_2IrO_3 crystals could be increased by 11 orders of magnitude by varying etching times. The samples which turned metallic show transport anomalies consistent with charge density wave or structural instabilities, (iv) first crystal growth of Li_2RuO_3 is reported where the Xtals crystallize in the $P2_1/m$ structure and show the expected high temperature magneto-structural transition, and (v) design and crystal growth of a new layered honeycomb lattice iridate K_2IrO_3 with an interlayer separation between Ir honeycomb planes which is more than a factor of 2 larger than in Na_2IrO_3. Magnetic measurements on crystals reveal localized effective spin $S = 1/2$ interacting strongly $\theta = -210$ K but without magnetic order down to 1.8 K. Thus K_2IrO_3 is a new Kitaev spin liquid candidate.

List of Publications

1. *Heat capacity evidence for proximity to the Kitaev QSL in A_2IrO_3 (A = Na, Li)*
   Kavita Mehlawat, A. Thamizhavel, and Yogesh Singh
   Phys. Rev. B. **95**, 144406 (2017).

2. *First-order magneto-structural transition in single crystals of the honeycomb lattice Ruthenate Li_2RuO_3*
   Kavita Mehlawat and Yogesh Singh
   Phys. Rev. B. **95**, 075105 (2017).

3. *First-order density-wave-like transitions in surface-doped Na_2IrO_3*
   Kavita Mehlawat and Yogesh Singh
   Phys. Rev. B **94**, 041109(R) (2016).

4. *Raman signatures of strong Kitaev exchange correlations in $(Na_{1-x}Li_x)_2IrO_3$: Experiments and theory*
   S. N. Gupta, P. V. Sriluckshmy, **Kavita Mehlawat**, A. Balodhi, D. K. Mishra, S. R. Hassan, T. V. Ramakrishnan, D. V. S. Muthu, Y. Singh and A. K. Sood
   Euro. Phys. Latt. **114**, 47004 (2016).

5. *Fragile magnetic order in the honeycomb lattice Iridate Na_2IrO_3 revealed by magnetic impurity doping*
   Kavita Mehlawat, G. Sharma and Yogesh Singh
   Phys. Rev. B **92**, 134412 (2015).

6. *Direct evidence for dominant bond-directional interactions in a honeycomb lattice iridate Na_2IrO_3*
   S. H. Chun, J.-W. Kim, J. Kim, H. Zheng, C. C. Stoumpos, C. D. Malliakas, J. F. Mitchell, **Kavita Mehlawat**, Y. Singh, Y. Choi, T. Gog, A. Al-Zein, M. M. Sala, M. Krisch, J. Chaloupka, G. Jackeli, G. Khaliullin and B. J. Kim
   Nat. Phys. **11**, 462 (2015).

Refereed Conference Proceedings

7. *Density wave like transport anomalies in surface doped Na_2IrO_3*
   Kavita Mehlawat and Yogesh Singh
   AIP Advances 7, 055710 (2017) **7**, 055710 (2017).

8. *Evolution of magnetism in Ru doped Na_2IrO_3*
   Kavita Mehlawat and Yogesh Singh
   AIP Conf. Proc. **1731**, 140036 (2016).

Acknowledgment

First and foremost, I would like to express my heartfelt gratitude to my supervisor, Dr. Yogesh Singh for his guidance and innovative support. I genuinely appreciate him for giving me an opportunity to work on the exciting problem in the field of strongly correlated material. I am grateful to him for the efforts he made during scientific discussion related to my project. His constant reassurance, endless encouragement, moral and emotional support in the difficult phase, and valuable suggestion boosted me at each and every step of my research work.

I would also like to express my sincere gratitude to my doctoral committee members, Dr. Sanjeev Kumar and Dr. Abhishek Chaudhuri for their valuable comments.

I would like to acknowledge XRD facility, GISAXS facility, Clean room facility and SEM facility of IISER Mohali. I am grateful to Inderjit that helps us to used RIE-Plasma and EDX facility.

I appreciate the financial support provided by IISER Mohali and for attending the HFM-2016 in Taiwan. I would also like to acknowledge DST India providing financial support for attending the MMM-2016 in the USA. I am grateful to University Grants Commission (UGC), India for the research fellowship during Ph.D.

I am grateful to all members of Novel Material Lab:- Ashiwini, Jaskaran, Amit, Anzar, Ankit, Shama and former members as well: Dr. Gyaneshwar, Anooja, Prins, and Kavita. They help me in during experimental measurement, scientific discussion, operating software and infinity of other things.

I would like to thanks to my friends Nidhi, Monika, Anshu, Gopal, Jyoti, Akanksha, Amandeep, Shubhendu, Sandeep, Deepak, Aslam, Balal, Leena, Suman, Ritesh, Soumya, for making my years enjoyable at IISER Mohali. Special thanks go to Mrityunjay and Shekhar. From outside the IISER Harish, Keerti, and Parul who have always motivated me. My sincere appreciation to my friends, seniors, and all who contributed to the completion of my doctoral dissertation. Mess staff of Hostel-5, Lala Bhaiya canteen and Bishvjeet Bhaiya also deserve big thanks for providing meals day in and day out.

My deepest appreciation to my niece Tannu, Prevash, nephew Rahul, Ojas, Vaidhvik, and my younger brother Krishan for making crazy and joyful moment at home.

This Ph.D. work would not have been possible without blessing and encouragement of my parents. They have always made sure their children gets the best possible opportunities at every step. I would never be able to return their unconditional love and support.

Above all, I would like to express my deepest gratitude to the Almighty for his blessing.

Contents

List of Figures

List of Tables

Chapter 1

General Introduction

1.1 Introduction

For the last several decades, transition metal oxides (TMO) have been attracting special attention in the condensed matter community due to novel phenomenon including the Mott insulating state, high temperature superconductivity, metal-insulator transitions, giant and collossal magnetoresistance, and quantum spin liquid states which have been discovered in TMO's [16–19]. Such a large variety of novel physical phenomenon arises from the mutual interplay of the bandwidth (W), the on-site coulomb potential (U), the crystalline electric field (CEF), and the spin-orbit (SO) coupling (λ) [20].

In 3d TMO's, the CEF splits the degenerate d-band. Then, the hierarchy of energy scales is: $U > W >>$ SO. This leads to materials having even partially occupied d-orbitals becoming insulators. These correlation driven insulators are called Mott insulators.

As one goes to 4d- and 5d- TM compounds the size of the d-orbital and hence the band-width W increases and U relatively decreases. Additionally, SO-coupling, which is a small perturbation in 3d-TMO's, grows as Z^4 and becomes an important energy scale for heavier (high Z) materials.

Thus in 5d-TMO's, the three energy scales-bandwidth (W), on-site Coulomb potential (U) and spin-orbit coupling (λ)-become comparable, opening up the possibility of novel physical phenomena due to the interplay between these energy scales.

Iridium is a 5d-transition metal element and Ir-based TMO's would be an ideal platform to search for novel behaviour arising from an interplay between electronic correlations, band width, SO-coupling, and lattice topology.

Indeed, iridium based oxides, such as the square lattice materials A_2IrO_4 (A = Sr, Ba)[3, 20–22], pyrochlore lattice based materials $R_2Ir_2O_7$ (R = Y, Eu, Sm) [23–25], the perovskite materials $Sr_3Ir_2O_7$ and $SrIrO_3$ [26], the honeycomb lattice Iridates A_2IrO_3 (A = Na, Li) [1, 4, 5], and the hyperkagome lattice material $Na_4Ir_3O_8$ [27, 28] have been compounds of intensive recent investigations. The 5d transition-metal oxides are expected to be wide-band weakly correlated metals due to the large spatial extent of their d orbitals. However, the above-mentioned iridates belong to a new class of spin-orbit-assisted Mott insulators where the insulating state arises from the combined effect of strong spin-orbit coupling and Coulomb correlation [3, 4, 20, 29]. Additionally, Mott insulators with strong spin-orbit coupling can realize novel types of magnetic exchanges and low energy Hamiltonians [4, 5, 29, 30]. We will elaborate on the effect of strong SO-coupling on the band structure of iridates in a later section.

The iridium-based honeycomb lattice family A_2IrO_3 (A = Na, Li) has been studied extensively because of the possibility of realisation of the Kitaev-Heisenberg model. It was shown by Jackeli and Khaliullin [4] that in materials with strongly spin-orbit entangled effective moments, the low energy magnetic Hamiltonian would depend on the lattice geometry and could interpolate between purely isotropic Heisenberg-like for corner shared octahedra with a 180° transition metal-oxygen-transition metal (TM-O-TM) bond, to a bond-dependent quantum compass model for edge shared octahedra with a 90° TM-O-TM bond. For the specific case of a honeycomb lattice, the quantum compass model becomes the Kitaev model. The Kitaev model is one of the simplest Hamiltonians for spins $S = \frac{1}{2}$ on a honeycomb lattice which involves bond-dependent nearest-neighbor interactions, is exactly solvable, and harbors a quantum spin liquid ground (QSL) state with Majorana fermion excitations [31]. The suggestion that the Kitaev Hamiltonian and the related Kitaev-Heisenberg Hamiltonian [4, 5, 31, 32] could be realized in a family of honeycomb lattice iridates A_2IrO_3 (A = Na, Li) has led to a flurry of activity on these materials [1, 2, 7, 33–41] as well as more recent work on the honeycomb lattice ruthenate α-$RuCl_3$ [42–48].

1.2 Crystal structure of A_2IrO_3

The crystal structure of A_2IrO_3 (A = Na, Li) materials is shown in the Figure 1.1. The structure is made up of layers containing only the A atoms alternating with AIr_2O_6 layers stacked along the c-axis [1]. Within the AIr_2O_6 layers the edge sharing IrO_6 octahedra form a honeycomb lattice and A atoms sit at the center of the honeycomb. Each of the IrO_6 octahedra are connected with three other neighboring octahedra as shown in the Figure 1.1 panel (a). One of the AIr_2O_6 slabs viewed along the c axis to highlight the honeycomb lattice of Ir atoms within the layer shown in the Figure 1.1 panel (b).

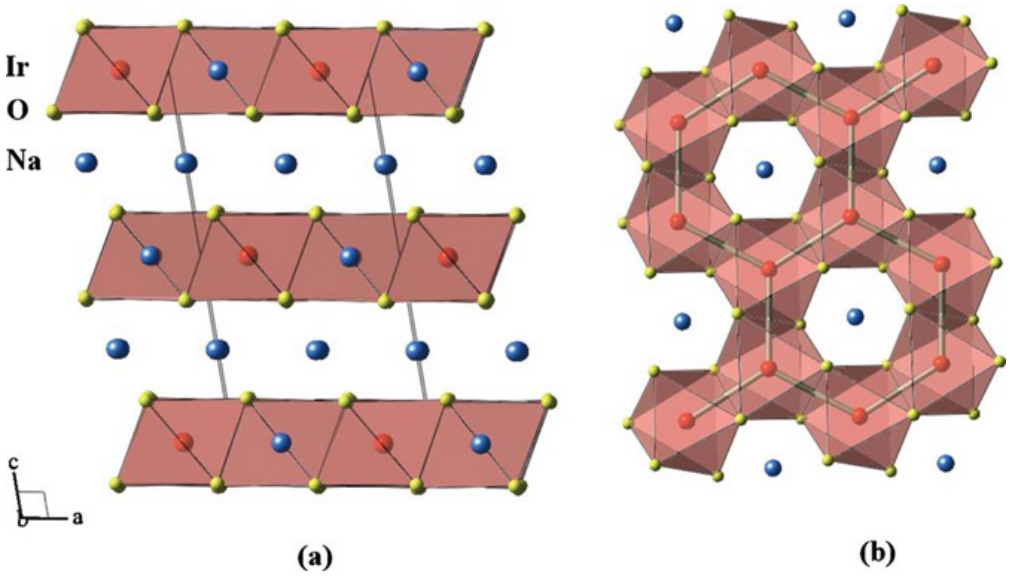

FIGURE 1.1: The crystallographic structure of Na_2IrO_3. The Na, Ir and O atoms are shown as blue, red, and yellow spheres, respectively. (a) The view perpendicular to the c axis showing the layered structure with layers containing only Na atoms alternating with slabs of $NaIr_2O_6$ stacked along the c axis. (b) One of the $NaIr_2O_6$ slabs viewed along the c axis to highlight the honeycomb lattice of Ir atoms within the layer. The Na atoms occupy voids between the IrO_6 octahedra. (Reprinted from [1]).

An idealized crystal structure of this kind corresponds to having all nearest neighbour Ir-Ir and Ir-O distances equal and Ir-O-Ir bond angles of 90°. The experimental structure of Na_2IrO_3 shows a few distortions compared to this idealized structure:

▶ The three O-Ir-O bond angles perpendicular to the basal plane are all greater than 90°.

▶ An orthorhombic distortion introduces inequality among nearest neighbour Ir-Ir distances and among nearest neighbour Ir-O distances.

► The structural distortion indicates the presence of a trigonal crystal field in addition to the cubic crystal field, due to the repulsion of neighboring Ir atoms across the edge-shared octahedra

► IrO_6 octahedra rotations that place O atoms on the faces of a cube containing an Ir hexagon.

► Trigonal distortion which is a compression of the IrO_6 octahedra in the c-direction that induces a departure from 90 degrees of the Ir-O-Ir angles as shown in the Figure 1.2.

Thus the experimental structure of A_2IrO_3 has some departures from the idealized theoretical structure for which the Kitaev-Heisenberg model is written. This may lead to additional exchange interactions which could alter the predicted magnetic phase diagram.

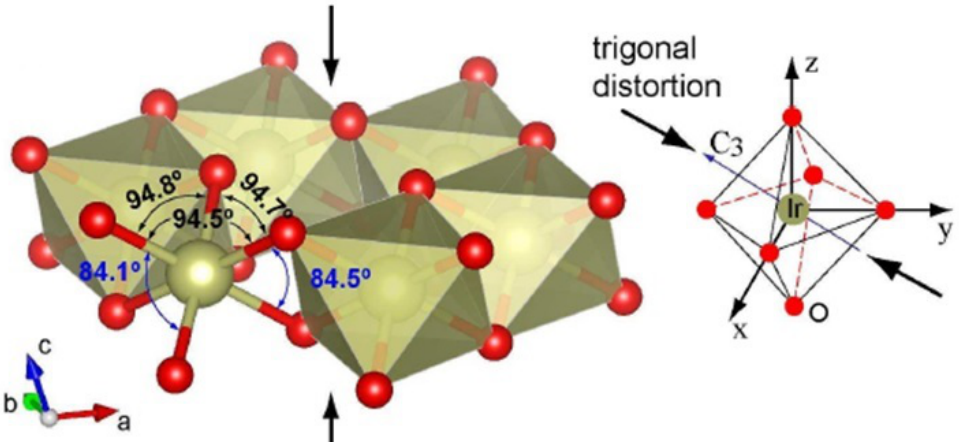

FIGURE 1.2: Local structure within the basal plane: the compression of IrO_6 octahedra along the stacking leads to the decrease of O-Ir-O bond angles across the shared edges. Measurement was done by Ye et. al [2].

1.3 Honeycomb lattice Iridates under strong SOC

Spin orbit coupling (SOC) is defined as the interaction between orbital angular momentum (L) and spin angular momentum (S) of an electron. The spin-orbit (SO) Hamiltonian is given by:

$$H_{SO} = \lambda L.S \quad , \tag{1.1}$$

where λ is the energy scale of spin-orbit coupling (SOC) between the nucleus and the electrons and it increases as $\propto Z^4$ [49]. Therefore, λ becomes an important factor in determining the electronic state of a solid comprising of heavy elements.

In honeycomb lattice iridates A_2IrO_3 (A = Na, Li), under strong spin-orbit coupling (SOC) limit, H_{SO} can not be treated as a perturbation. Thus, S and L do not commute with the atomic Hamiltonian and the total angular momentum J = L + S becomes a good quantum number in the strong SOC limit. J can take values from $|L-S|$ to $|L+S|$. In A_2IrO_3 (A = Na, Li), Sr_2IrO_4 and IrO_2 iridates, the Ir ions are in the oxidation state 4+ giving the d-orbital electronic configuration of $5d^5$. Crystal fields from O^{2-} ligands split the degenerate 5d-states into two sets of states, triply degenerate t_{2g} and doubly degenerate e_g levels. Since Hund's coupling energy in 5d transition metal is similar to 0.5 eV, which is much smaller than CF splitting (2-3 eV), the 5 electrons occupy the lower t_{2g} level. If we turn on the SOC, we have to define the orbital angular momentum $|L|$ of the t_{2g} orbital. Angular momentum matrix elements for all 5 electrons in t_{2g} will be given by $< t_{2g}|L|t_{2g} >$. The resulting angular momentum matrix elements are the same as for the p orbital. Hence orbital angular moment of 5d-orbital $L = 2$ is quenched to an effective value $L_{eff} = 1$ in iridates. The effective spin angular momentum is then $S_{eff} = \frac{1}{2}$ arising from one t_{2g} hole. By LS coupling, the 3-fold degenerate t_{2g} level is thus split into a higher energy $J_{eff} = \frac{1}{2}$ state and a lower energy doubly degenerate $J_{eff} = \frac{3}{2}$ state due to strong SOC [3].

Out of the 5 electrons of Ir^4+ 4 electrons occupy in the $J_{eff} = \frac{3}{2}$ orbital and the remaining one is in the $J_{eff} = \frac{1}{2}$ orbital. The partially filled $J_{eff} = \frac{1}{2}$ band is split from $J_{eff} = \frac{3}{2}$ by a spin-orbit coupling term $\lambda \approx 0.5$ eV. In this interpretation, the system is expected to be a metal because it has a partially filled highest occupied level or band. With the inclusion of Coulomb interaction ($U \sim$ 1–2 eV), there occurs a further split of

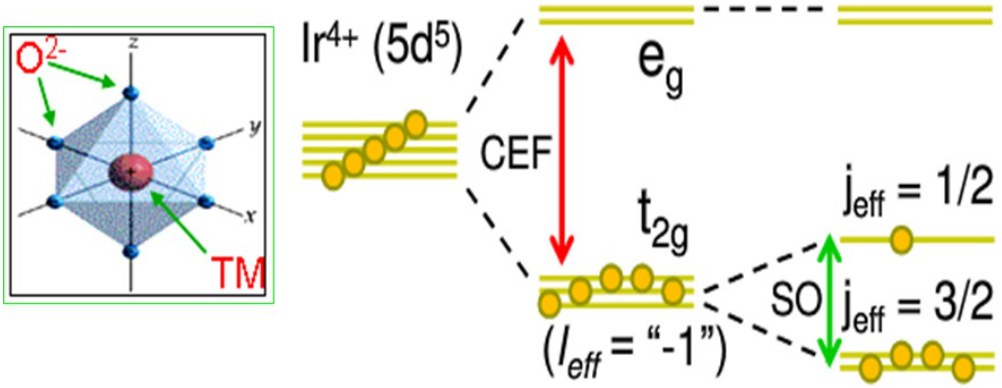

FIGURE 1.3: Splitting of $5d^5$ state under octahedral crystal electric field (CEF) and spin orbit coupling (SOC). Schematics of electronic level splitting of $J_{eff} = \frac{1}{2}$ spin-orbit Mott insulating state. Yellow solid circles represent five spins. Adopted from [3]

the partially filled $J_{eff} = \frac{1}{2}$ band into a lower energy, lower Hubbard band (LHB), and a higher energy upper Hubbard band (UHB), separated by U. In this way $J_{eff} = \frac{1}{2}$ LHB will be filled and $J_{eff} = \frac{1}{2}$ UHB will be empty and the system becomes an insulator. In Figure 1.3 a schematic is shown of how this $J_{eff} = \frac{1}{2}$ picture emerges starting from an atomic picture. Viewed in the band picture, one starts with an electron in the spatially extended 5d orbital which experiences a very small U which is unable to split the t_{2g} band on its own. However, even this small U is sufficient to split the much narrower $J_{eff} = \frac{1}{2}$ band which emerges after SO has been taken into account. Hence, this insulating state is mainly due to strong SOC acting together with the onsite U. This equivalent band structure view is shown in Figure 1.4.

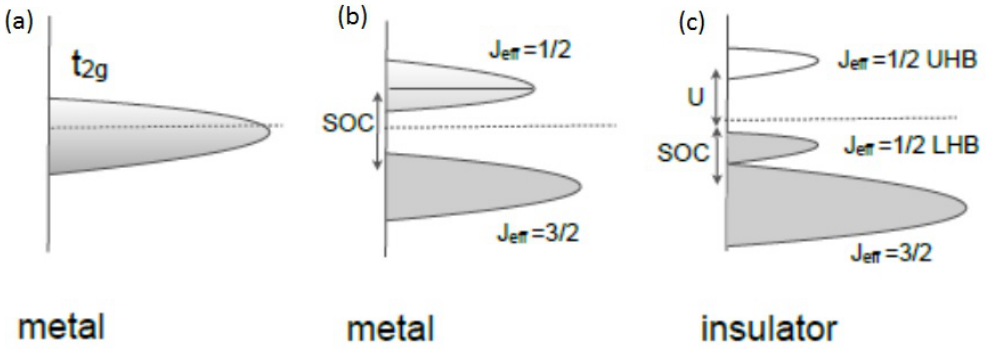

FIGURE 1.4: A schematic illustration of a partially filled t_{2g} orbital is shown in (a) and it's splitting is shown in (b) by a strong spin orbit coupling (SOC) into partially filled $J_{eff} = \frac{1}{2}$ and filled $J_{eff} = \frac{3}{2}$ state with SOC splitting. (c) Further splitting of the partially filled $J_{eff} = \frac{1}{2}$ band into filled LHB and empty UHB. The last two band splittings of the electronic state are shown in Fig. 1.3. This schematic drawing is based upon Ref. [3]

1.4 Electronic structure of A_2IrO_3 under SOC

In the strong SOC limit picture described above, the localized J_{eff} states are obtained by assuming the following hierarchy of energy scales $W < \lambda \leq U$, where $W \approx 4t$ is the d-electron bandwidth, t is the effective hopping parameter, λ is the SOC parameter and U is the on-site Coulomb repulsion. In this limit the electrons are localized. Resonant inelastic x-ray scattering (RIXS) and angle resolved photoemmission spectroscopy (ARPES) measurements have determined the band-structure of Na_2IrO_3 and have concluded that the $J_{eff} = 1/2$ picture is valid and that correlation effects and SOC have to be treated on an equal footing to understand the insulating state in this material [35, 36]. However the single electron hopping t and the bandwidth W for 5d orbitals is large $\sim$ 1.5 - 2 eV [50, 51] and an alternate itinerant description of the band structure of Na_2IrO_3 derived from the formation of quasi-molecular orbitals (QMOs) has also been put forward [50].

1.5 Honeycomb lattice compounds: theoretical aspects

In honeycomb lattice A_2TO_3 (A = Na, Li and T = Ir, Ru) materials, edge sharing octahedra TO_6 generate the honeycomb lattice having A-ions at the center of the octahedra as shown in Figure 1.5 [4]. Every T ion is surrounded by six oxygen ions, and edge sharing octahedra form a nearly 90° $T-O-T$ bond. Each TO_6 octahedra is connected to three neighbouring octahedra, thus t_{2g} orbitals of T ions participate in three different oxygen mediated hoppings with the three neighbouring T-ions. These three $T-T$ bonds xx, yy, and zz are different due to the different $T-O-T$ hopping and each are perpendicular to one of the local cubic axis x, y, and z, respectively.

Along the xx bond hopping takes place between the two neighbouring T orbitals $|xy>$ and $|xz>$ via an oxygen p_x orbital resulting in an Ising-like $S_i^x S_j^x$ spin coupling, similarly, $S_i^y S_j^y$ coupling for yy bond hopping happens between $|xy>$ and $|yz>$ orbitals via oxygen p_y and $S_i^z S_j^z$ coupling results from hopping between $|xz>$ and $|yz>$ orbitals via oxygen p_z. Thus, a strong spin-orbit coupling has introduced new physics to the honeycomb lattice: the isotropic part of the Hamiltonian completely vanishes whereas a bond-dependent Ising-like coupling survives. The finite anisotropic exchange interaction term left in the Hamiltonian depends on the spatial orientation of a given bond. The

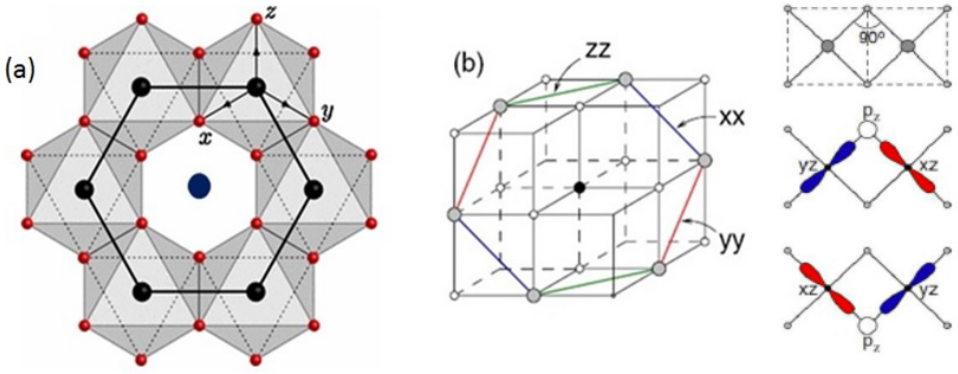

FIGURE 1.5: (a) View perpendicular to the c-axis of A_2TO_3-type layered compound, where the large blue circle represent the non magnetic ion (A = Na, Li), the black circles represent the transition metal magnetic ion (T = Ir,Ru) and the small red circles represent the oxygen ions. (b) The hexagonal unit cell of A $_2TO$ $_3$, in which T-ions form honeycomb lattice with three different bond xx, yy, and zz perpendicular to one of the cubic axes x, y, z, and 90°-bond formed by edge sharing octahedra reprint from [4]

Heisenberg model is thus converted into the Kitaev model which has a quantum spin liquid ground state [4]. The final exchange Hamiltonian can be written as:

$$H_{ij}^{\gamma} = -JS_i^{\gamma}S_j^{\gamma} \tag{1.2}$$

1.5.1 Kitaev-Heisenberg Model

The Kitaev-Hesienberg (KH) model for the honeycomb lattice iridates A_2IrO_3 (A = Na, Li) was introduced by Chaloupka et al. [5]. For the isotropic part of the super-exchange to cancel exactly, a 90° Ir-O-Ir bond geometry is required. If there are any deviations in the crystal structure leading to departures from 90° Ir-O-Ir bond geometry, then the cancellation is not exact and some part of the isotropic exchange will survive. Even for 90° Ir-O-Ir bond geometry, in addition to the anisotropic Kitaev ineractions, there will be direct Ir-Ir exchange interaction via overlap of their extended d-orbitals leading to an isotropic Heisenberg-like exchange. Thus the total spin Hamiltonian for A_2IrO_3 with nearest neighbour (NN) interaction will be given as:

$$H = -K\sum_{<i,j>\gamma} S_i^{\gamma}S_j^{\gamma} + J\sum_{<i,j>} S_i.S_j \tag{1.3}$$

The first term represents the Kitaev exchange via three different NN bonds labeled as γ (= x, y, z) and K is the Ising-like ferromagnetic coupling between the NN Ir-spins.

The second term represents the antiferrmagnetic (AF) Heisenberg exchange between NN spins where J is the AF spin-coupling. To determine the phase diagram, Equation 1.3 was parametrized as K = 2α and J =1-α, where α quantifies the relative strengths of the two exchange terms [5]. The parametrized KH model is given in Equation 1.4. The complete phase diagram was studied in the parameter range 0 $< \alpha <$ 1.

$$H = -2\alpha \sum_{<i,j>\gamma} S_i^\gamma S_j^\gamma + (1-\alpha) \sum_{<i,j>} S_i.S_j \tag{1.4}$$

At $\alpha = 0$ only the Heisenberg term contributes and one obtains a Néel ordered ground state. In the opposite limit of $\alpha = 1$, Eqn. 1.4 corresponds to the exactly solvable Kitaev model which has a quantum spin liquid ground state [31]. There is also an intermediate state at $\alpha = \frac{1}{2}$ where the model is exactly solvable and the ground state is an AF state called the stripy antiferromagnet, with spins polarized in the direction of one of the crystallographic axis. Hence, the KH model gives the phase diagram shown in the Figure 1.6. The dotted vertical line in the phase diagram indicates the boundary between different ordered phases. Which of these predicted phases is realized in the actual materials became a topic of intense experimental investigations.

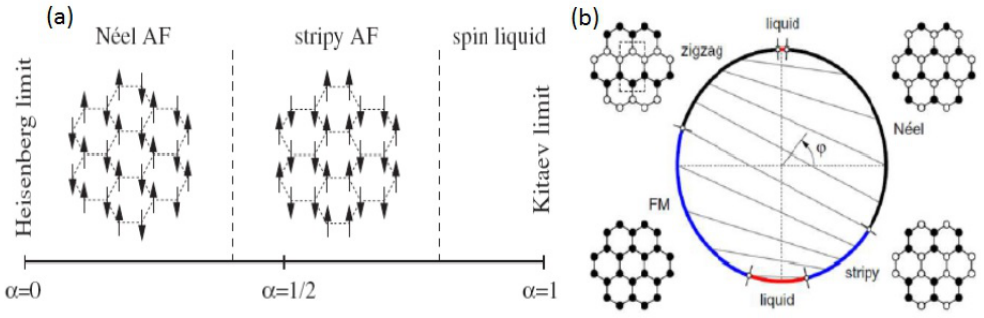

FIGURE 1.6: (a)Phase diagram of Heisenberg-Kitaev (HK) model with AF Heisenberg and FM Kitaev, reprinted from [5]. (b) Phase diagram of the generalized HK model containing all four combinations of FM and AF; Kitaev and Heisenberg interaction, reprinted from [6].

1.6 Magnetic structure of A_2IrO_3

The first measurements of magnetic susceptibility and heat capacity on single crystals of Na_2IrO_3 [1] and polycrystals of A_2IrO_3 [34] showed that both materials have long-range magnetic order below $T_N \approx 15$ K and hence were not situated in the strong Kitaev limit where a QSL state was expected. There are two predicted magnetic states in the KH

model, the stripy antiferromagnet and the Néel antiferromagnet and it was left to be explored as to which of these was realized in actual materials. The magnetic structure for Na_2IrO_3, was first studied using resonant x-ray magnetic scattering (RXMS) measurements performed by Liu et al. [41]. The results confirmed that Na_2IrO_3 has an antiferromagnetic long-range ordered ground state below $T_N \approx 15$ K. From the azimuthal dependence of the magnetic peaks, the ordered magnetic moment was determined to point along the crystallographic a axis. The experimental results were consistent with two candidate magnetic structures: the zig-zag antiferromagnet and the stripy antiferromagnet. Combining the experimental data with first-principles calculations, Liu et al. proposed that the zig-zag phase was the most likely ground state [41].

In Fig. 1.7, schematics of the three candidate antiferromagnetic spin structures are shown: (a) Néel (b) zig-zag (c) stripy. The difference between the zig-zag and stripy structures is that the zig-zag structure can be viewed as antiferromagnetically coupled ferromagnetic spin chains and stripy structure can be viewed as ferromagnetically coupled antiferromagnetic spin chains, viewed along the crystallographic a-axis of honeycomb lattice [7].

The zig-zag magnetic structure was confirmed by a neutron diffraction study by Ye et al. [2]. This study also estimated an ordered moment of about 0.2 μ_B/Ir [2] consistent with bulk heat capacity measurements [1, 34].

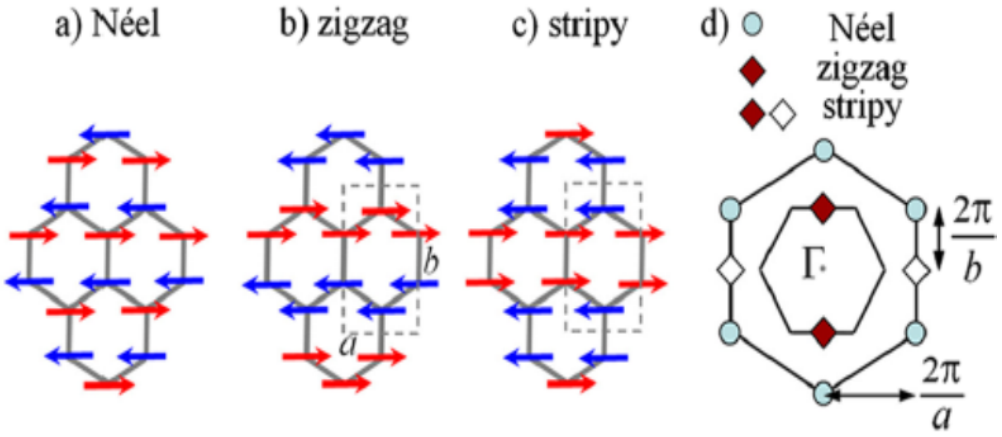

FIGURE 1.7: (a) Néel (b) zig-zag (c) stripy spin structure in honeycomb lattice. (d) position of the magnetic Bragg peaks in reciprocal space for various magnetic phase reprinted from [7].

Magnetic excitations in Na_2IrO_3 were first studied by Choi et al. who used inelastic neutron scattering to study spin wave excitations of the magnetically ordered state.

The magnetic dispersion could be quantitatively accounted for by including substantial further-neighbour in-plane exchanges which were found to stabilize zig-zag order. This hints at the possibility of additional exchange terms present for the real A_2IrO_3 materials compared to the terms in the nearest-neighbour KH model.

1.7 Dimerized structure in Li_2RuO_3

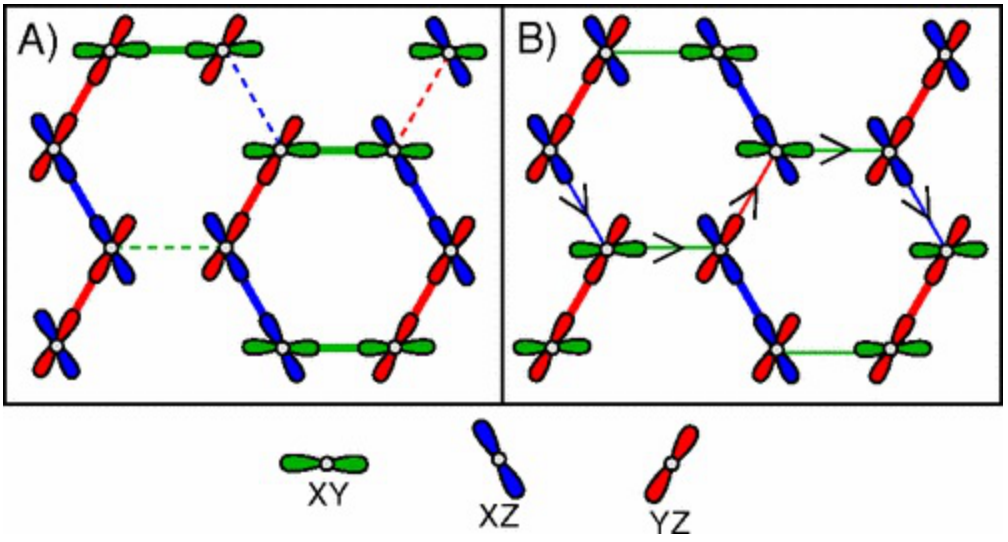

FIGURE 1.8: Examples of orbital and spin-coupling patterns on the honeycomb lattice of Ru ions. (a) Decoupled AF chain and ring with corresponding orbital pattern. (b) An example of the spin-singlet dimer covering minimizing the energy at zero Hund's coupling. Thick (thin) lines denote AF (FM) intra-(inter-)dimer bonds, respectively. Dashed lines stand for the noninteracting bonds. reprint from [8]

Replacing Ir in A_2IrO_3 by Ru to make A_2RuO_3 would be interesting as it leads to a reduced SO-coupling and is also equivalent to applying chemical pressure since Ru^{4+} is smaller than Ir^{4+}. Indeed the honeycomb-lattice ruthenate compounds A_2RuO_3 (A = Li, Na) exist with S = 1 originating from Ru^{4+} in the low-spin state [8, 52, 53]. In contrast to A_2IrO_3 (A = Li, Na), work on polycrystalline Li_2RuO_3 has shown an unusual phase transition at $T_d \approx 540$ K from a nearly perfect honeycomb lattice C2/m structure at high temperature to a low temperature distorted honeycomb lattice $P2_1/m$ structure [12, 54]. This structural transition is accompanied by a strong decrease of the magnetic susceptibility and increase in the resistance. The undistorted honeycomb lattice C2/m present at high temperature undergoes a strong distortion, leading to a low temperature structure with shortening of one of the three distinct Ru-Ru bonds in the Ru hexagon [12]. Based on density functional theory (DFT) it was proposed that

Li_2RuO_3 undergoes a transition from a highly correlated metal to a molecular orbital insulator involving Ru-Ru dimers and spin-singlet formation [12, 54]. In the Li_2RuO_3 crystal structure, three distinct bonds of honeycomb lattice are in xy, xz, and yz planes as shown in the Figure 1.8 [8].

All of this is based on experimental work that has been on polycrystalline materials. When single crystals were produced recently [55], they were found to have magnetic properties completely different from all known polycrysatlline work [12, 56–58]. Thus, the sample dependence of the ground state and magnetic properties of A_2RuO_3 is some thing which deserves more careful work.

1.8 Motivation and purpose

The focus in this thesis is on the family of quasi-two-dimensional honeycomb lattice iridates A_2IrO_3 (A = Na, Li) and related materials. Although these materials have been studied extensively through the last 5 years or so, there are several open questions which we have aimed to address in our work.

(i) The minimal model required to describe the observed magnetic behavior is still debated. For example, the observed zig-zag magnetic order[2, 7] can result either from a competition of nearest neighbour Kitaev and Heisenberg terms, or it could be stabilized from purely Heisenberg exchange upto the third nearest neighbour. So the nature and range of magnetic exchange interactions is still unclear.

(ii) For both A_2IrO_3 materials, while the role of the Kitaev term in stabilizing the unusual magnetic orders [2, 7, 59, 60] is accepted, it is still unclear as to how close or far they are from the Kitaev's QSL state. The lack of experimental evidence in this regard mostly stems from a lack of testable predictions made for the real materials. Recently, however, there have been specific theoretical criteria proposed to test proximity to the Kitaev limit and we have performed experiments to test these predictions.

(iii) The difference in the Weiss temperatures between Na_2IrO_3 and Li_2IrO_3 is a factor a 3–4, yet the magnetic ordering happens at the same temperature. This difference in magnetic scales between the two materials is not understood currently.

(iv) These iridates are half-filled Mott insulators, much like the cuprates which are parent compounds for high-T_c superconductors. A natural question to ask is whether it is possible to get superconductivity on doping the iridates too. There are recent predictions of unconventional superconductivity as well as charge/spin density wave orders in the doped Kitaev-Heisenberg model [10]. However, doping of these materials has not been realized experimentally before our work.

(v) Finally, since the A_2IrO_3 materials are both magnetically ordered and not strictly quantum spin liquids, can new materials with similar structures be designed and synthesized which would be better realizations for Kitaev physics and might host a QSL state.

All these open problems and predictions motivated us to study in detail the materials A_2TO_3(A = Li, Na, K, T = Ir, Ru). In this thesis, we have studied the evolution of magnetic properties of A_2IrO_3 in response to various perturbations like chemical doping, external pressure, and surface doping. Additionally, we have grown single crystals of a new material K_2IrO_3 which has never been studied before. We report its preliminary structure and magnetic properties which strongly suggest that it could be a new QSL candidate.

1.9 Structure of the thesis

The thesis is organized as follows:

► Chapter 2 describes the techniques that are used for synthesis and characterization of the samples studied in this thesis. Polycrystalline and single crystalline materials have been synthesized using solid-state reaction method and self-flux growth method, respectively. The powder X-ray diffraction (PXRD) and single crystal X-ray diffraction techniques are performed for confirmation of structure and phase purity. The chemical composition and morphology of the resulting samples are checked using energy dispersive x-ray (EDX) spectroscopy on a scanning electron microscope (SEM). We also briefly describe how magnetic susceptibility and magnetization, electrical and thermal transport, and heat capacity measurements were performed using a Quantum Design physical property measurement system (PPMS).

► Chapter 3 deals with the honeycomb lattice iridate materials A_2IrO_3 (A = Na, Li). We first set out to discover the optimal synthesis conditions which would give us high quality single crystals of Na_2IrO_3 and polycrystals of A_2IrO_3 (A = Na, Li). We then measured the magnetic susceptibility χ up to 1000 K with the aim of estimating the Weiss temperatures θ in the true paramagnetic state for both materials. This gave the first surprise when we found $\theta = -120$ K for Na_2IrO_3 and $\theta = -100$ K for Li_2IrO_3, respectively. The value for Na_2IrO_3 is close to that reported from low temperature ($T <$ 300 K) χ data. However, the θ for Li_2IrO_3 is a factor of 3 larger than reported previously [1]. This means that the magnetic energy scales for the two materials, contrary to what was believed earlier, could be quite similar. This is significant and will help constrain exchange parameters used in future theoretical modelling of these materials.

First thermodynamic evidence for proximity to the Kitaev's QSL is found in our heat capacity $C(T)$ measurements. The $C(T)$ shows a two-peak structure and the magnetic entropy shows a half plateau between the peaks with a value close to $\frac{1}{2}$Rln2. This is evidence for the fractionalization of spins into Majorana Fermions as predicted recently [61]. Additionally, our low temperature $C(T)$ data show a conventional $C \sim T^3$ for Na_2IrO_3 but an unusual $C \sim T^2$ behavior for Li_2IrO_3. This suggests 2-dimensional magnetic excitations in Li_2IrO_3 which is quite unexpected.

► Chapter 4 describes our attempts to try to perturb Na_2IrO_3 by chemical doping and to track the evolution of magnetism. We investigated iso-electronic doping at both the Na and Ir sites by partially replacing Na by Li and partial replacement of Ir by Ru, respectively. The motivation was to track the magnetic order as doping beyond the percolation threshold was done. We were able to produce single crystals of doped compositions and study their physical properties using electrical transport, magnetic susceptibility, AC susceptibility, and heat capacity measurements. As we were starting this study, a Li doping study appeared in literature [38] and hence we did not pursue this part any further in the thesis. We only note here that we were able to confirm the suppression of the magnetic ordering temperature on increasing Li substitution in $(Na_{1-x}\ Li_x)_2IrO_3$ up to x $\sim$ 0.25 where a miscibility gap was found and mixed phase samples were obtained for larger x.

The investigation of $Na_2Ir_{1-x}Ru_xO_3$ gave the following results: (i) Ru has one less electron than Ir and hence a partial substitution of Ir by Ru should lead to hole doping. However, we found, rather surprisingly, that the electrical transport on crystals remains highly insulating with no sign of the charge gap reducing up to $x = 50\%$. (ii) The long ranged magnetic order at $T_N = 15$ K is immediately suppressed and a spin-glass state that appears below $T_g \sim 5.5$ K even for the smallest Ru concentration ($x = 5$ %). This clearly demonstrates the fragile nature of the magnetic order in Na_2IrO_3 [62]. Even 5% magnetic impurity is enough to induce a frozen spin state, suggesting that disturbing the short-ranged magnetic exchange pathways lead to drastic modification of the magnetic ground state. These results highlight the importance of nearest-neighbor magnetic exchange in Na_2IrO_3. This is in contrast to a similar study on $Li_2Ir_{1-x}Ru_xO_3$ which found that magnetic order persist up to much larger doping levels ($x \approx 20$ %) [63].

► Chapter 5 describes our attempts to try to dope charge carriers into Na_2IrO_3. The conventional routes like chemical substitutions, electrochemical intercalation, removal of oxygen in reducing conditions, were all attempted but were not successful. We were finally able to tune the electrical transport in Na_2IrO_3 crystals by reactive ion plasma etching of the surface of as grown crystals. We found that etching resulted in the removal of Na from the surface without the surface structure being modified. We were able to tune the electrical transport in Na_2IrO_3 all the way from insulating to metallic (a change of 11 orders of magnitude) by varying the etching times. The samples etched for various

times showed anomalous temperature dependencies including behavior consistent with Topological insulators, charge or spin density wave transitions, and structural transitions [64, 65]. Remarkably, some of these features had been predicted for the doped Kitaev-Heisenberg model [10] and a comparison with theory would suggest a specific sign for the Kitaev interaction in this material. This work also provides a new method of doping the surface of other layered materials like Mott insulators or Topological materials.

► Chapter 6 describes our work in trying to understand conflicting reports on the magnetic behaviors of the related honeycomb lattice ruthenate Li_2RuO_3. Polycrystalline Li_2RuO_3 has been reported to show an unusual phase transition below $T_d \approx 540$ K from a nearly perfect honeycomb lattice C2/m structure at high temperature to a low temperature $P2_1/m$ structure with a distorted honeycomb lattice [12]. Below T_d one of the three inequivalent Ru-Ru bond in the honeycomb hexagon became significantly shorter than the other two [54]. This structural dimerization is also accompanied by Ru-Ru spin singlet formation leading to a strong decrease of the magnetization at T_d [12, 54]. These experimental observations have led to many theoretical efforts to understand the nature of the transition and the role of electronic correlations. Based on DFT calculations it was proposed that Li_2RuO_3 undergoes a transition from a highly correlated metal to a molecular orbital insulator involving Ru-Ru dimerization and spin-singlet formation [12, 54]. An alternative mechanism of spin-singlet formation driven by magnetoelastic coupling has also been proposed [8]. An electronic structure study has highlighted the importance of electronic correlations and proposed that a combination of local-moment behavior and molecular orbital formation could be the correct picture for this material [66]. Broad transitions and sample dependent magnetic properties of the polycrystalline samples have plagued efforts to understand these materials fully and ideally high quality single crystals are required. Single crystals of Li_2RuO_3 were indeed recently synthesized. However, these have added to the prevailing confusion. The crystals were found to crystallize at room temperature in either the C2/m or the $P2_1/m$ structures depending on synthesis conditions. However, in complete contrast to all existing polycrystalline work [12, 56–58] neither of these crystals show the coupled magneto-structural transitions at high temperature. They instead show Curie-Weiss behavior below 300 K and magnetic ordering at low temperatures into supposedly antiferromagnetic states [53].

We have synthesized single crystals of Li_2RuO_3 for the first time. These crystallize at

room temperature in the target $P2_1/m$ structure and show the expected high temperature magneto-structural transition. We are thus able to investigate for the first time the anisotropic properties of Li_2RuO_3 across this high temperature coupled transition. Our magnetic measurements between 2 and 1000 K reveal that the transition is first-order in nature and most likely occurs in two steps with the structural transition occurring first at a higher $T_d \simeq 570$ K and then drives the magnetic transition around $T_m \simeq 540$ K. The $\chi(T)$ behaviour above T_d is consistent with quasi-2-dimensional magnetism.

► We have also attempted to discover and synthesize new previously unknown materials in related structures and to study their magnetic properties in search of novel behaviors including Kitaev's QSL state. One direction in search of such a material is to synthesize materials where the Iridium oxide layers are separated by a larger distance compared to the A_2IrO_3 materials to enhance the two-dimensionality. In Chapter 7, we report that we have succeeded in producing single crystals of a new, layered, honeycomb iridate K_2IrO_3. Our preliminary structural determination studies suggest that this new material is isostructural to the above studied iridates A_2IrO_3 but with a larger c-axis lattice parameter which matches our design goal. Measurements of the magnetic susceptibility indicate Mott insulating behavior with localized $S = 1/2$ moment magnetism. An estimate of the Weiss temperature gave $\theta \approx -200$ K suggesting strong antiferromagnetic interactions. However, no signature of magnetic ordering was observed down to 1.8 K, a temperature smaller than $\theta/100$. This strongly points to the possibility of a quantum spin liquid state in this new material. The properties of this possible QSL phase and its relation to Kitaev's QSL will have to be explored in future measurements possibly on larger crystals.

► Appendix A.1 Resonant X-Ray Scattering (RIXS) employed on single crystal of Na_2IrO_3:

Honeycomb lattice iridates, A_2IrO_3 (A= Na, Li), offer potential realizations of the Kitaev magnetic exchange coupling. However, direct evidence of the same has been lacking. Direct consequences of the existence of Kitaev coupling would be bond-directional magnetic interactions and real space-momentum space locking. In this collaboration we performed diffuse magnetic X-ray scattering which reveals broken spin rotational symmetry even above the Néel temperature, with the three spin components exhibiting short-range correlations along different crystallographic directions. This spin and real-space entanglement directly uncovers the bond-directional nature of these interactions,

thus, providing a direct connection between honeycomb iridates and Kitaev physics [13].

► Appendix A.2 Experiments and theory of Raman response of $(Na_{1-x}Li_x)_2IrO_3$:
Inelastic light scattering studies on single crystals of $(Na_{1-x}Li_x)_2IrO_3$ (x = 0, 0.05 and 0.15) show a polarization-independent broad band at ~ 2750 cm^{-1} with a large bandwidth ~ 1800 cm^{-1}. For Na_2IrO_3 the broad band is seen for temperatures $\leqslant 200$ K and persists inside the magnetically ordered state. Such a mode has recently been predicted (by Knolle et al.) [67] as a signature of the Kitaev spin liquid. We assign the observation of the broad band to be a signature of strong Kitaev exchange correlations. The broad band persists even inside the magnetically ordered state below T_N. The Raman response calculated in mean-field theory shows that the broad band predicted for the SL state survives in the magnetically ordered state near the zigzag-spin liquid phase boundary. A comparison with the theoretical model gives an estimate of the Kitaev exchange interaction parameter to be $J_K \approx 57$meV [14].

► Appendix A.3 High Pressure measurement on A_2IrO_3 (A= Na, Li):
The novel magneto-structural transition involving dimerization and spin-singlet formation in Li_2RuO_3 are very different from the magnetic behavior in A_2IrO_3. Since Li_2RuO_3 has smaller lattice parameters than A_2IrO_3 it would be interesting to ask if A_2IrO_3 might also show such magneto-structural transitions if their lattice parameters are reduced. To this end, we have studied the structural properties under high pressure of the honeycomb lattice iridates A_2IrO_3 (A= Na, Li) in collaboration with the high pressure X-ray group at Tel Aviv University, Israel. We find that at pressures $\sim 3-4$ GPa both Na_2IrO_3 and Li_2IrO_3 shows structural transition very similar to the dimerized phase transition which occurs in Li_2RuO_3 [12]

Chapter 2

Experimental Techniques

In this chapter we describe the synthesis and measurement techniques that are used for preparing, characterizing, and performing physical property measurements on samples used in this thesis. Both polycrystalline and single crystalline materials have been used in our work and we start by describing the methods to synthesize both types of samples.

2.1 Sample Synthesis

The polycrystalline samples of the transition metal oxides A_2TO_3(A = Na, Li, T = Ir, Ru) were synthesized using the solid state reaction method which we describe below.

2.1.1 Solid State Reaction Method

The most widely used technique to synthesize polycrystalline samples is the solid state reaction method. As the name suggests, this method involves a reaction of two or more solid components. It is probably obvious that such a reaction will not be completed in any reasonable time scale at room temperature. It is therefore required to heat them at high temperatures, typically $\sim$ 1200 °C [68]. At these high temperatures, the reaction, between the thoroughly mixed starting materials, happens through diffusion and still takes several days and requires several such heat treatments to get a final sample which is phase pure.

One needs to keep the following in mind in preparing for a solid state reaction method: (1) Stoichiometric amounts of reagents must be used. (2) Based upon the reactivity of reagents, different crucible and environment need to be considered. (3) The starting materials have to be mixed thoroughly in an agate mortar and pestle typically for about an hour. (4) To promote proximity of reagents, we press the starting mixture into 5–10 mm pellets by applying a pressure of ~ 6 tonnes. (5) Mixed materials/pellets have to be given high temperature heat treatments for several days with intermediate grinding.

We now describe the synthesis details of the specific materials studied in this thesis.

2.1.1.1 A_2TO_3 (A = Na, Li, T = Ir, Ru) Polycrystal

The polycrystalline sample of Na_2IrO_3 was synthesized using solid state reaction method following a protocol described previously [1]. The starting materials, Na_2CO_3 (99.995% Alfa Aesar) and anhydrous IrO_2 (99.99% Alfa Aesar) or Ir powder (99.99% Alfa Aesar), were taken in the ratio 1.05 : 1 and were mixed thoroughly in an agate mortar-pestle. The mixture was placed in an alumina (Al_2O_3) crucible with a lid and loaded into a box furnace. Since the melting point of $Na_2CO_3 \simeq 823°C$ is relatively low, the first heat treatment was given at 750°C for 24 hours. During this step, Na_2CO_3 gives off CO_2 and the following reaction is initiated.

$$Na_2CO_3 + Ir \setminus IrO_2 \longrightarrow Na_2IrO_3 + CO_2 \tag{2.1}$$

After this calcination (giving off CO_2) step, the resulting material was thoroughly mixed, pelletized and given heat treatments between 950 °C and 1050 °C in 50 °C steps with intermediate grinding, mixing and pelletizing, after each step. In each step the material is heated (sintered) for 48 hours after which the furnace is turned off and allowed to cool to room temperature.

Polycrystalline Li_2IrO_3 samples are synthesized similarly. The starting materials Li_2CO_3 (99.99% Alfa Aesar) and anhydrous IrO_2 (99.99% Alfa Aesar) or Ir powder (99.99% Alfa Aesar) are taken in the ratio 1.05 : 1 and mixed well for an hour before initial heat treatment. The melting point of $Li_2CO_3 \simeq 723°C$ is lower than Na_2CO_3. Therefore, the calcination reaction was done at 700 °C and the following reaction is initiated in this

step,

$$Li_2CO_3 + Ir \setminus IrO_2 \longrightarrow Li_2IrO_3 + CO_2 \tag{2.2}$$

After this first step, the resultant material was ground and mixed in acetone and pelletized for further sintering. Sintering was done at temperatures between 900°C - 1000°C, in 50 $^{\circ}C$ steps for 48 hours each. For Li_2IrO_3 polycrystals it is known that the magnetic properties depend critically on quality of sample, It is is therefore important to get high quality samples to study the intrinsic magnetic properties. The above protocol was found to produce high quality samples of Li_2IrO_3 with sharp anomalies in thermodynamic measurements at the magnetic transition. The magnetic properties for both Li_2IrO_3 and Na_2IrO_3 and their dependence on synthesis conditions will be discussed in detail in the next chapter.

Polycrystalline samples of Li_2RuO_3, $Na_2Ir_{1-x}Ru_xO_3$, and $(Li_{1-x}Na_x)_2RuO_3$ have also been investigated in this thesis and these have been synthesized using a solid state reaction method with protocols similar to the ones described above.

We next describe the methods used for the growth of single crystals studied in this thesis.

2.1.2 Self-Flux Growth Method

The single crystal growth method we have used for materials studied in this thesis is the self-flux growth method. In the usual flux method, or solution growth method, the target material is dissolved in a solvent upto super-saturation, and then the solvent is allowed to evaporate, or the temperature is lowered, and dissolved material crystallizes out of the solvent. This can be used to grow for example crystals of table salt (NaCl) out of a flux or solvent of water. In the self-flux method, one of the starting material itself acts as the flux in which the target material is grown. In this process, one starts with an off-stoichiometric amount of starting materials with an excess of the component which is going to be used as the flux. A mixture of starting materials is heated to a temperature which is higher than the melting point of the flux and then the mixture if cooled slowly (typically 1–5 °C/hr). Crystals grow during this slow cooling stage. Thermal strain free single crystal can be grown using this method [69, 70].

Due to the long duration of the growth process the choice of crucible material is very important. The crucible should be made of highly stable, non-reactive material which has high thermal conductivity. The crucibles most commonly used are ceramics such as alumina (Al_2O_3), zirconia (ZrO_2), silicon carbide (SiC), and boron nitride (BN). The other main challenge in the flux growth method is to separate out the crystal from the flux. The common methods used to remove flux from the crystals is to either decant the flux while it is still molten or to dissolve the flux in some convenient solvent which hopefully doesn't attack the crystals themselves.

We now give details of the growth of materials studied in this thesis.

2.1.2.1 A_2TO_3 (A = Na, Li T = Ir, Ru) Single Crystal

Single crystals of Na_2IrO_3 were grown using self-flux method. The starting materials used were Na_2CO_3 (99.995% Alfa Aesar) and anhydrous IrO_2 (99.99% Alfa Aesar) or Ir powder (99.99% Alfa Aesar). Materials were taken in the ratio 1.05 : 1, mixed thoroughly in an agate mortar, and the mixed powder was placed in an alumina crucible and calcined at 750 °C for 24 hours. After this initial heat treatment, the sample was ground and pelletized and then heated at 900 °C for 48 hours before cooling to room temperature. This process gave us polycrystalline powder of Na_2IrO_3.

In the next step, 10 % (atomic) IrO_2 was added to the above obtained black powder and mixed thoroughly under acetone to promote homogeneity. This homogeneous mixture was then heated to 1050 °C in 6 hours and held at this temperature for 72 hours after which it was furnace cooled to 900 °C at 10 °C /hr). The furnace is then switched off and the crucible was air quenched. Shiny plate-like crystals were found standing vertically in a semi-melted polycrystalline bed. The separation of the crystals is very tricky, as they are randomly stacked and found to grow into each other and are very thin. Nevertheless, crystals were carefully separated with fine tip tweezers. The largest crystals obtained have the dimensions 6 mm×3 mm×0.2 mm as shown in the given Figure 2.1.
Single crystals of $Na_2Ir_{1-x}Ru_xO_3$, Li_2RuO_3, and $(Li_{1-x}Na_x)_2RuO_3$ were grown similarly using a self-flux method.

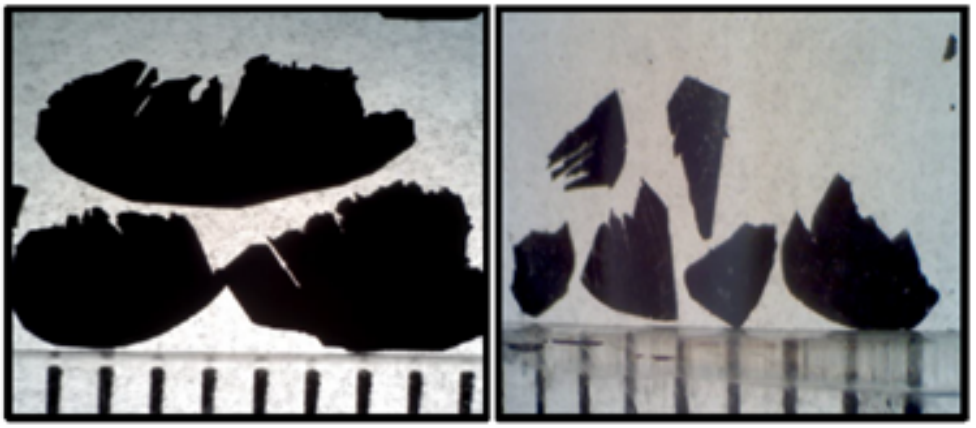

FIGURE 2.1: A few large crystals obtained after separation are shown placed next to a millimeter scale.

2.2 Structure characterization : X-ray diffraction

X-ray diffraction is a well known and widely used technique which reveals the arrangement of atoms or molecules inside the crystal. Before investigating the physical properties of any material synthesized in this thesis we have first investigated their crystal structure and confirmed phase purity and chemical composition. X-rays are electromagnetic radiation having wavelength comparable to inter-atomic distances in the crystalline solids [71, 72]. A single crystal can act as a three dimensional natural grating for x-rays [71]. Therefore x-ray diffraction experiment provides an invaluable tool for studying the structures of crystals.

W. L. Bragg and W. H. Bragg put forward a pioneering theory of x-ray diffraction which is known as Bragg's law. According to this theory, a crystal may be divided into various sets of parallel atomic planes. X-rays incident on the crystal are reflected by sets of parallel planes in the crystal followed by constructive interference of the resulting reflected rays. Based on this considerations, the Braggs derived a simple mathematical relation which gives the condition for observing a Bragg reflection,

$$2d \sin\theta = n\lambda \tag{2.3}$$

where d is the inter-planar distance between the (hkl) planes, λ is the wavelength of the incident x-ray beam, θ is the scattering angle and n is a positive integer giving the

order of reflection, $n \epsilon [1, 2, ..]$. So in a typical diffraction experiment with a fixed λ one makes an intensity versus 2θ scan. One obtains Bragg reflections at all the different 2θ for which the Bragg condition is satisfied. The full set of reflections are a characteristic of the crystal structure. The positions of the Bragg peaks give the unit cell parameters and the intensity of the peaks are given by the structure factor and hence arrangement of the various atoms inside the unit cell [71]. After recording experimental x-ray data of synthesized materials, we analyse the phase purity by qualitatively matching the obtained x-ray pattern with the expected pattern found in the International Centre for Diffraction Data (ICDD) data base using X′PERT Highscore software. After phase purity identification, a more quantitative analysis is done by fitting the obtained data with the expected structural model. This Rietveld refinement is performed using General Structure Analysis Software (GSAS) [73, 74].

2.3 Chemical Analysis : Energy-dispersive x-ray

To determine the chemical composition of the grown materials one quantifies the atomic fractions of each of the elements present in the material. This has been done using energy dispersive x-ray spectroscopy (EDS) on a JEOL scanning electron microscope (SEM). The principle of the method relies on the fact that each element has a unique atomic structure. When a sample is bombarded with a focused high energy electron beam ($E = 40$ keV), electrons from elements comprising the surface of the sample are excited from their ground state to higher levels. The resulting electron vacancies in the lower level are filled by the electrons in higher state and the energy difference is emitted as x-rays. Each element has a characteristic x-ray spectrum and individual elements in the samples are traced by the detection of this characteristic x-ray spectrum. The composition of the material can be quantified very accurately. In principle by the EDS analysis, all elements from atomic number Z = 4 (Be) to 92 (U) can be detected.

2.4 Magnetic Measurement : Vibrating sample magnetometer

An efficient experimental apparatus to measure the magnetization is the vibrating sample magnetometer (VSM). This unique technique is credited to S. Foner [75]. A VSM measures the net magnetic moment of the sample. A VSM consists of a linear motor to oscillate the sample at some desired frequency, a pick-up coil for signal detection, a lock-in amplifier, and electronics to control the linear motor. In this magnetometer, the sample is placed at the center of pick-up coil and made to vibrate sinusoidally up and down through the coil. A voltage is induced in the pick-up coil by the changing magnetic moment due to the movement of the sample.

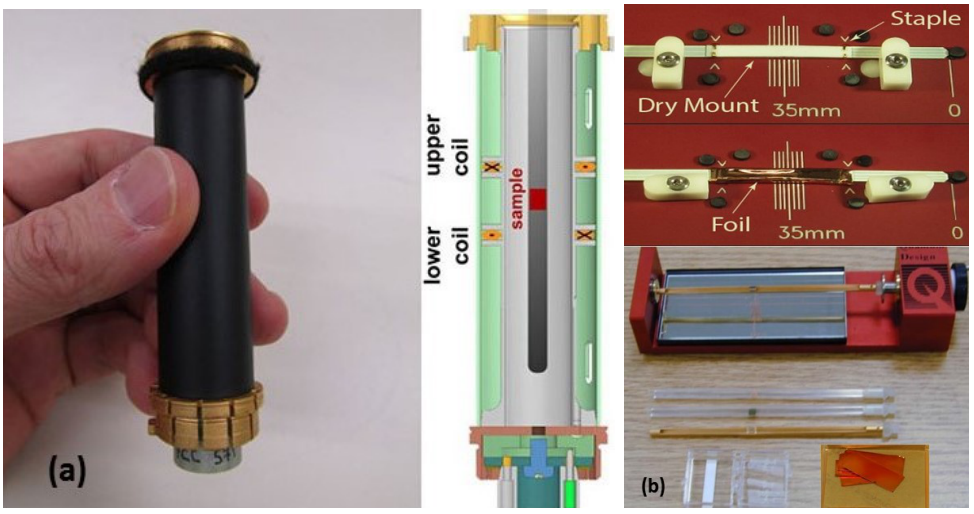

FIGURE 2.2: Left) VSM pick-up coil. Middle) schematic representation of VSM pick up coil, and Left) sample mounting platform.

The pick-up coil has two counter-wound coils arranged as shown in the given Figure 2.2(a). The sample sits in one of the coils and the other coil is used to cancel out the voltage generated due to the background, or sample holder. Thus, only the signal from the sample is measured and is proportional to the magnetic moment M. We have used a commercial physical property measurement system (PPMS) by Quantum Design (QD) for the VSM measurements [76].

The molar magnetic susceptibility χ in units of cm^3/mol is obtained from M measured in the units $G\ cm^3$, using the relation,

$$\chi = \frac{M M_w}{H m} \tag{2.4}$$

where M_w is the molecular mass of the sample, m is the mass of the sample in grams and H is the applied magnetic field in Gauss.

2.5 AC Susceptibility

AC susceptibility measures the magnetic moment of a material induced by the application of the small oscillating magnetic field. The technique is sensitive to small changes in magnetization and is an important method for the characterization of the dynamic magnetism of a material which is not obtained in the DC magnetic measurement described above. In an AC measurement, the oscillating magnetic field induces a time-dependent magnetic moment in the specimen which in turn induces a proportionate time-dependent signal in the pickup coil. Frequency dependent AC susceptibility measurements are therefore important for materials where dynamic magnetic responses are expected. For example spin glasses and ferromagnets. The behavior of AC magnetization for very low frequency f is expected to be most similar to a DC ($f = 0$) measurement. We have measured the AC susceptibility for some materials by applying a low amplitude of the ac field (~ 5 Oe) and varying frequency in the range 10–10000 Hz using a QD-PPMS.

2.6 Heat Capacity

Heat capacity of a material $C = \Delta Q/\Delta T$ is the amount of heat ΔQ required to raise the temperature of the material by ΔT. It is a unique thermodynamic technique to investigate structural and magnetic phase transitions in materials. The heat capacity measurement option of the QD-PPMS was used for all our temperature T and magnetic field H dependent C measurements. The PPMS uses a relaxation technique to determine the heat capacity [77].

In this method, the sample is placed on a platform which is connected with a weak thermal link to a constant temperature bath (puck), at a temperature T_0 a small amount of heat raises the temperature of the sample by ΔT (typically $\Delta T/T \approx 1\%$) and then it decays exponentially down to the puck temperature [78]. The exponentially decaying

temperature of the sample T_s is given by

$$T_s = T_0 + \Delta T exp(-t/\tau_1) \tag{2.5}$$

where t is the time and τ_1 is sample to bath relaxation time constant. The heat capacity C is determined from the measurement of τ_1 and the known thermal conductivity κ of the weak thermal link as

$$C = \tau_1 \kappa \tag{2.6}$$

The sample holder or puck and a schematic of the sample platform are shown in Fig. 2.3. A thermometer and resistive heater are attached to the bottom of the platform. The puck thermometer is attached within the sample puck. The platform thermometer and heater are connected with four small thermally conducting wires which provide both structural and thermal support to the platform. The sample was mounted on the platform using a thin layer of grease (Apiezon-N). The grease provides the thermal connection for the sample to the platform of the puck. During the measurement in the PPMS, the temperature of the sample platform is measured by the platform thermometer and this is taken as the temperature of a sample. The puck thermometer measures the temperature of the whole puck which serves as the heat sink. The adiabatic condition required for such measurements is achieved inside a high vacuum chamber with a lowest pressure 10^{-6} mbar using the cryopump high-vacuum option. The heat capacity measured is therefore at constant pressure.

The heat capacity measurement of solid materials can provide crucial information about the lattice, electronic, and magnetic properties of materials. Contributions to heat capacity for a solid crystalline material can come from three sources: (1) lattice contribution which is theoretically explained by the Debye theory (at low temperature $C \propto \beta T^3$), (2) electronic contribution ($C_{el} \propto T$), and (3) magnetic contribution ($C_m \propto T^\delta$). Hence the total heat capacity is given by:

$$C_p = \gamma T + \beta T^3 + A T^\delta \tag{2.7}$$

where γ is the Sommerfeld coefficient which represents the electronic heat capacity

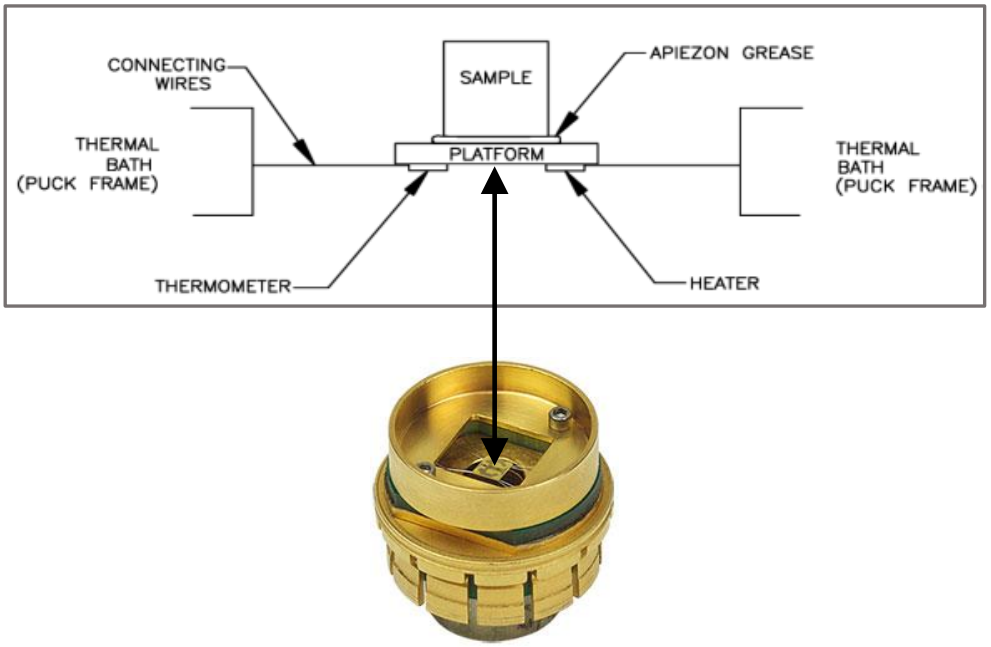

FIGURE 2.3: Schematic representation of the thermal connection to the sample and the sample platform in the heat capacity puck.

contribution, β is the Debye constant and gives the lattice heat capacity, and the third term represents the magnetic heat capacity where the exponent δ depends on the details of the magnetic state of the solid.

2.7 Resistivity

Temperature dependent resistivity ρ measurement of a material demonstrates whether it as an insulator or metal. Both DC and AC resistivity of various samples have been measured in a four-probe geometry in the temperature range 2 K to 400 K using the QD-PPMS [9]. In a four probe measurement, a constant current I is applied to the outer probes and potential difference V is measured across the inner probes. The inner probes draw very small current (ideally no current) because of the high impedance of the voltmeter. Thus unwanted voltage drop at the contacts due to contact resistance between probes and the sample is eliminated from the voltage measurement. The resistivity ρ of the sample is obtained from a voltage V measurement at constant current I using the Ohm's law:

$$\rho = (\frac{VA}{IL}). \tag{2.8}$$

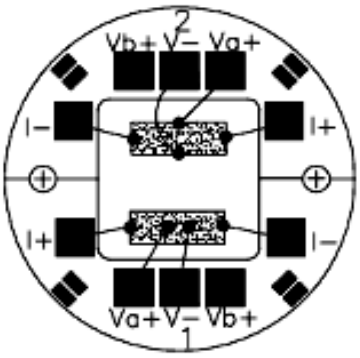

FIGURE 2.4: Schematic representation of electrical connections made to samples on an AC resistivity puck. Channel 1 is set-up for a 4-probe resistivity measurement while channel 2 is set-up for a 4-wire Hall effect measurement [9]. The dark squares represent the current I and voltage V contact pads.

Here A is the cross-sectional area of the sample through which current passes, and L is the distance between the two voltage leads. The resistivity measurements were carried out in either the DC and AC transport mode. In DC transport a DC current I is used while in an AC transport measurement an AC current I is used. Typical 4-probe resistivity (channel 1) or Hall effect (channel 2) connections made on samples are shown in the schematic diagram in 2.4. Silver paint or silver epoxy and Cu or Au wires (diameter ≈ 50 μm) were used for electrical contact between the sample and the contact pads on the puck.

Chapter 3

Thermodynamic properties study of A_2IrO_3 (A = Na, Li)

3.1 Introduction

The honeycomb lattice iridate family A_2IrO_3 (A = Na, Li) have been studied intensively for the last 5 years or so because of their potential as candidates for realization of the Kiteav-Heisenberg model [1, 2, 4–7, 34–37, 39, 41, 79–82]. These materials were experimentally found to be Mott insulators where the Mott insulating state arises from a co-operation between electron correlation and strong spin-orbit coupling. Both materials have been shown to be long ranged magnetically ordered at low temperature $T \leq 15\ K$ with strong antiferromagnetic interaction $\theta \approx -120\ K$ for Na_2IrO_3 and a smaller $\theta \approx -33\ K$ for Li_2IrO_3 [1, 2, 7, 34]. Thus, both materials are not the spin liquids that one expects in the pure Kitaev limit. However, there is growing evidence of the importance of Kitaev interactions for understanding the magnetic behaviours of both materials. Direct evidence of bond-directional magnetic exchange and real-space and momentum-space locking, both consequences of dominant Kitaev interactions, were recently found in Na_2IrO_3 using diffuse resonant x-ray scattering (RIXS) measurements on Na_2IrO_3 [13]. Large Kitaev exchange has also been concluded from first principles *ab initio* estimations of the exchange parameters [39, 80, 81], and recently, a novel prediction for signatures of Kitaev's QSL in Raman scattering experiment on Na_2IrO_3 have been made[67] and have been observed experimentally on Na_2IrO_3 and $(Na_{1-x}Li_x)_2IrO_3$

[14]. Optical spectroscopy measurements on Na_2IrO_3 also claimed to observe signatures consistent with proximity to a QSL state [83]. However, how close or far the real materials are to the Quantum Spin Liquid (QSL) state in the dominant Kitaev limit it is still debated in the community. The absence of direct evidence is in part due unavailability of clear criteria applicable to the real materials.

Recently, quantum Monte-Carlo calculations have been reported by Nasu et al. to investigate the thermodynamic properties of the Kitaev model on a honeycomb lattice [84]. It was predicted that for the Kitaev model the temperature dependent heat capacity would show two peaks coming from the fractionalization of a single quantum spin into two kinds of Majorana fermions: one itinerant (dispersive) and other one localized (dispersionless) [84]. The two peaks in the heat capacity can be understood to come from thermal excitation of these two kinds of Majorana fermions. In between these peaks, a plateau pinned at $\frac{1}{2}$Rln2 in the temperature dependent magnetic entropy S_{mag} was also predicted. These predictions for the Kitaev model are however still not applicable to the real materials which are magnetically ordered [1, 2, 34] and most likely have other exchange terms in their Hamiltonian [39, 80, 81]. More recently, thermodynamic properties for the generalized Kitaev-Heisenberg model and for the *ab initio* Hamiltonian for Na_2IrO_3 have been calculated [81]. It was predicted that even for the real (magnetically ordered) material proximate to Kitaev's QSL, the two-peak structure in heat capacity will survive and the plateau observed for the pure Kitaev model would smear out into a shoulder in S_{mag} but would still be pinned at $\frac{1}{2}$Rln2 [61]. These features were shown to vanish when the material is deep into the magnetically ordered state away from the QSL state [61]. Thus, a well separated two-peak structure observed in the magnetic heat capacity and a shoulder in S_{mag} pinned in between the two peaks with a value close to $\frac{1}{2}$Rln2 is the predicted "smoking-gun" hallmark to place A_2IrO_3 materials proximate to Kitaev's QSL [61].

Additionally, the *ab initio* estimations of the exchange parameters [39, 80, 81] and inelastic scattering measurements like Raman [14] and RIXS [13, 35] suggest a large magnetic energy scale, for A_2IrO_3.

In this chapter, we report the magnetic susceptibility χ versus temperature up to 1000 K and heat capacity measurements in the temperature range 0.075 K $\leq T \leq$ 155 K on polycrystalline samples of the honeycomb lattice iridates A_2IrO_3.

3.2 Experimental Details

Polycrystalline samples of A_2IrO_3 were synthesized using a solid state reaction method starting with high purity chemicals and heating the pelletized mixtures between 900 and 1000 ^{o}C in 50 ^{0}C steps. The step-wise heating instead of going directly to 1000^o C was found to be essential for the formation of high quality samples. Powder X-ray diffraction on crushed pieces of the samples confirmed the formation of single phase samples with lattice parameters consistent with previous reports [34].

The magnetic susceptibility χ versus temperature data were measured in the temperature range $T = 2$ K to 400 K using the VSM option of a physical property measurement system from Quantum Design (QD-PPMS). The $\chi(T)$ data between $T = 300$ K and 1000 K were measured using the VSM oven option of the QD-PPMS. The heat capacity C data were measured in the temperature range 2 K to 155 K using a QD-PPMS. The C data from 75 mK to 3 K was measured using the dilution refrigerator (DR) option of a QD-PPMS.

3.3 Magnetic Susceptibility

The magnetic susceptibility χ versus T data measured for A_2IrO_3 (A = Na, Li) between 2 and 1000 K in an applied magnetic field of $H = 1$ T are shown in the given Figure 3.1. A sharp anomaly is observed at low temperature $T_N \approx 15$ K for both samples in agreement with previously reported data [1, 34]. The high temperature data ($T \geq 300$ K) for each sample plotted as $1/\chi(T)$ versus T is shown in the inset of Figure 3.1.

For Na_2IrO_3 high temperature $1/\chi(T)$ data are approximately linear as shown in the inset of Figure 3.1. The $\chi(T)$ data between $T = 750$ and 1000 K were fit by the Curie-Weiss expression $\chi(T) = \chi_0 + \frac{C}{T-\theta}$, where χ_0 , C, and θ are fitting parameters. The fitted parameters values were found to be $\chi_0 = 2.66(3) \times 10^{-5}$ cm^3/mol, $C = 0.395(1)$ cm^3 K/mol, and $\theta = -127(4)$ K. These values are similar to the previously reported values obtained from a fit to the $\chi(T)$ data for $T \leq 300$ K [1, 34]. In particular, the value of θ, which gives the overall scale of the magnetic interactions, comes out to be very close to the value $-125(6)$ K previously reported for polycrystalline Na_2IrO_3 [34].

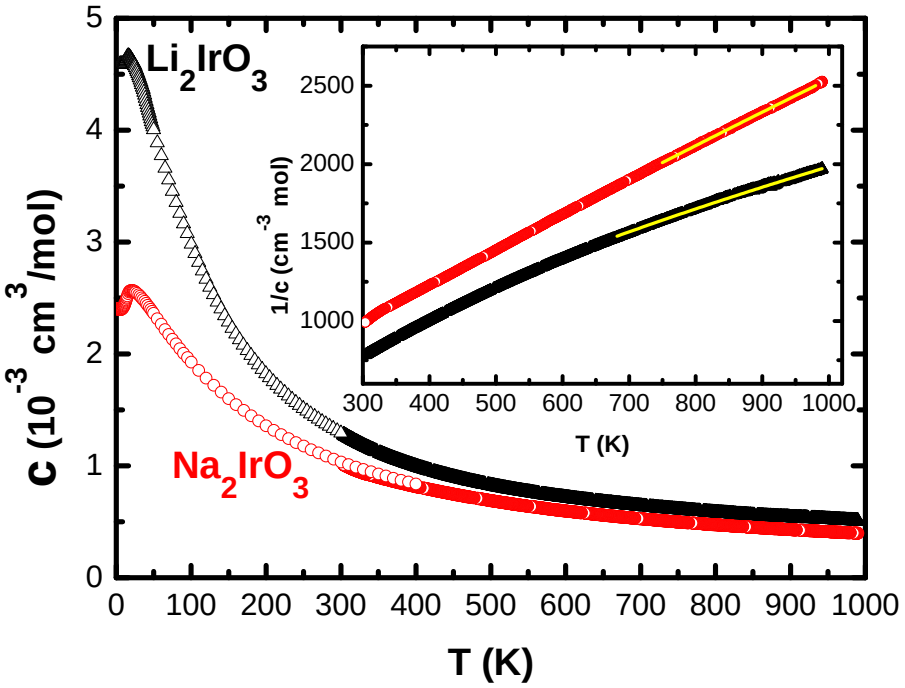

FIGURE 3.1: Magnetic susceptibility χ versus temperature T for A_2IrO_3 (A = Na, Li) measured between $T = 2$ K and 1000 K in a magnetic field of $H = 1$ T. Inset shows the $1/\chi(T)$ data above $T = 300$ K. The solid curves through the data are fits of the high temperature data to the Curie-Weiss behavior.

For Li_2IrO_3 the high temperature $1/\chi(T)$ data shows a prominent downward curvature as seen in the inset of Figure 3.1. This $1/\chi(T)$ behavior suggests a large and positive χ_0 and the large curvature also means that to obtain a reliable value of θ one needs to be well in the paramagnetic state. The $\chi(T)$ data between $T = 700$ and 1000 K were fit to the Curie-Weiss (CW) behavior. The fit gave the values $\chi_0 = 1.45(3) \times 10^{-4}$ cm^3/mol, $C = 0.403(2)$ cm^3 K/mol, and $\theta = -105(2)$ K. The value of χ_0 is slightly larger than obtained previously. The large χ_0 suggests a large Van Vleck paramagnetic contribution in susceptibility data for Li_2IrO_3. The most significant difference between the low temperature and high temperature fit parameters is the value of $\theta = -105(2)$ K which is larger by a factor of 3 in magnitude compared to the value -33 K obtained previously [1, 34]. This indicates that, in contrast to what was believed previously based on previous θ values, the magnetic energy scales for the two materials could be quite similar. This will help guide and constrain theoretical models written for Li_2IrO_3.

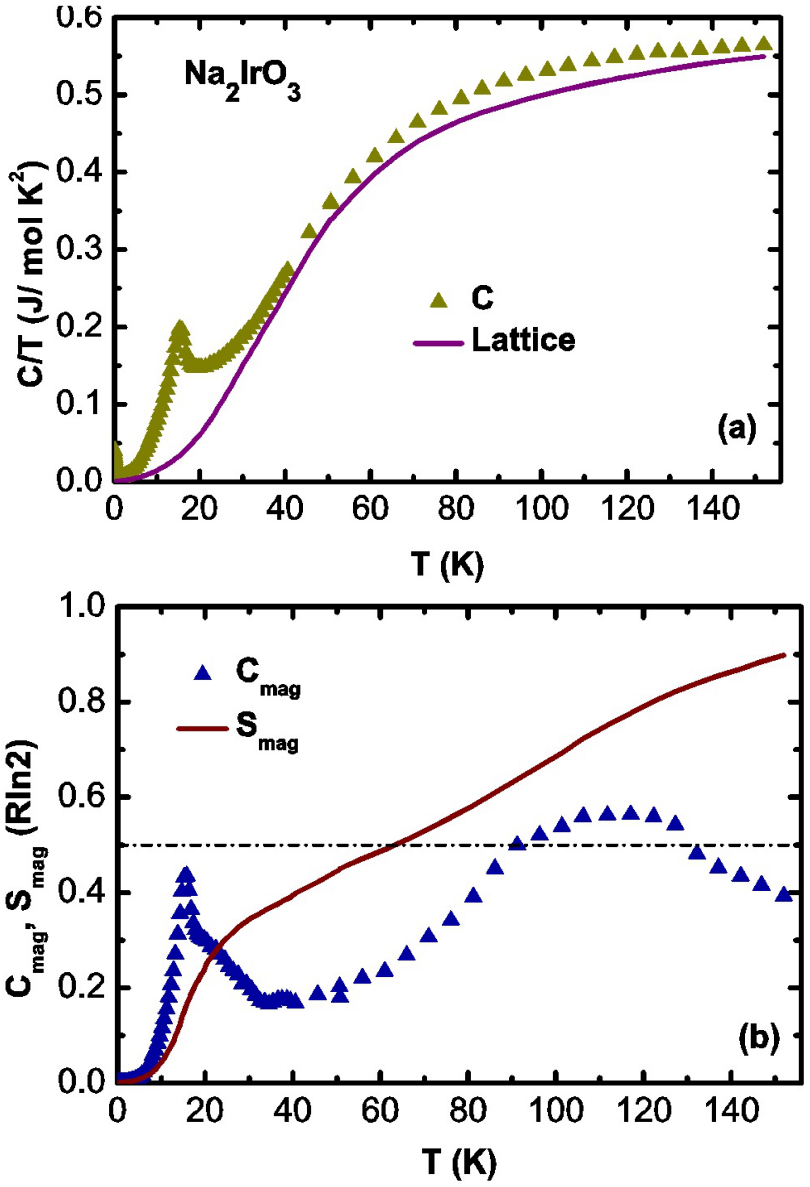

FIGURE 3.2: (a) Heat capacity divided by temperature C/T versus T for Na_2IrO_3. The lattice contribution to the heat capacity divided by temperature is shown as the solid curve. (b) Magnetic contribution to the heat capacity C_{mag} and the magnetic entropy S_{mag} in units of Rln2 versus T for Na_2IrO_3. The horizontal dash-dot line is the value $\frac{1}{2}$Rln2.

3.4 Heat Capacity

3.4.1 Na_2IrO_3

The heat capacity divided by temperature C/T versus T data for Na_2IrO_3 between T = 75 mK and 155 K are shown in Figure 3.2(a). A sharp λ type anomaly observed near 15 K confirms the antiferromagnetic transition for Na_2IrO_3 [1, 34] and indicates the high quality of sample used in the current measurements. An approximate estimation of

the lattice contribution to the heat capacity is obtained by measuring the heat capacity of non-magnetic analog Na_2SnO_3 and scaling the temperature (T) of it to account for the difference in molecular masses between the two compounds Na_2IrO_3 and Na_2SnO_3. The lattice heat capacity $C(T)$ for Na_2SnO_3 can be converted to the lattice $C(T)$ for Na_2IrO_3 by multiplying the T for $C(T)$ data of Na_2SnO_3 by the factor (θ_D of Na_2IrO_3 / θ_D of Na_2SnO_3)$^{1/2}$, where θ_D is Debye temperature.

The lattice contribution so obtained is shown in Figure 3.2(a). By subtracting this lattice contribution from the total C(T), we get the magnetic contribution to the heat capacity C_{mag}. This is shown in units of Rln2 in Figure 3.2(b). We first note that the low temperature lambda-type anomaly is sitting on a broad anomaly. In addition to this low temperature anomaly we find another broad peak centered around $\approx$ 110 K. Such a two-peak structure in the heat capacity has been predicted for the generalized Kitaev-Heisenberg Hamiltonian for parameters placing the material in the magnetic state proximate to Kitaev's QSL [61]. However a two peak structure is not unusual in frustrated and/or low-dimensional magnetic materials where a high temperature peak occurs at the onset of short ranged order while low temperature anomaly occurs due to long range order [85]. The definitive signature predicted for closeness to the Kitaev's QSL is that there must be a prominent plateau or shoulder in the T dependence of the magnetic entropy change S_{mag} data with a value pinned at $\frac{1}{2}$Rln2 between the temperatures of the two heat capacity peaks, [61, 84].

We have estimated the $S_{mag}(T)$ data by integrating $C_{mag}(T)/T$ vs T data. The T dependence of S_{mag} in units of Rln2 is shown in Figure 3.2(b). We note that there is a shoulder in $S_{mag}(T)$ between the temperatures of the two heat capacity peaks and its value is pinned close to the predicted value $\frac{1}{2}$Rln2 as shown by the horizontal dashed line in Figure 3.2(b). The high temperature anomaly in C_{mag} is quite broad and one can see a tail extending to even higher temperatures. Up to the highest temperature of our measurement, the value of the entropy change is $S_{mag} \approx 90\%$Rln2. It is evident that the full Rln2 entropy will be recovered at a slightly higher temperature. The two-peak structure in the magnetic heat capacity C_{mag} data and a shoulder pinned at $\frac{1}{2}$Rln2 are in excellent agreement with theoretical predictions and provide the first direct thermodynamic evidence that Na_2IrO_3 is situated in close proximity to Kitaev's QSL.

Low temperature C versus T data for Na_2IrO_3 measured down to T = 75 mK in the

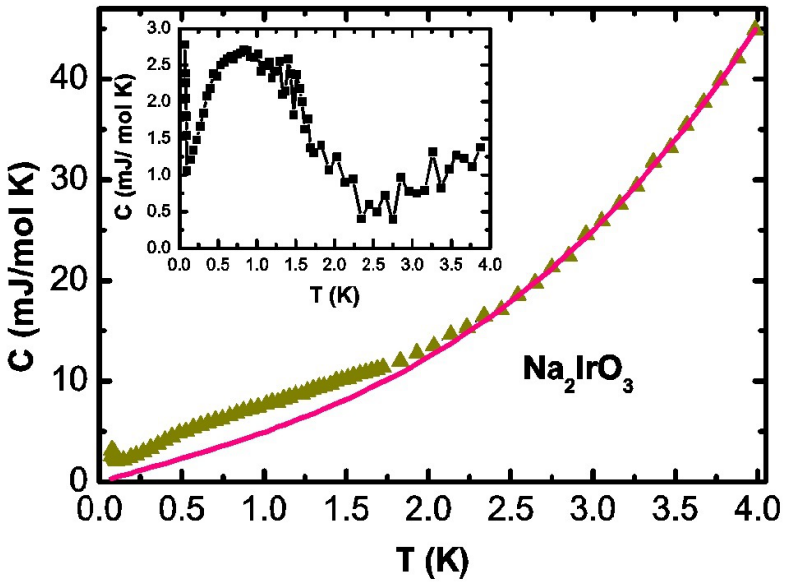

FIGURE 3.3: (a) Heat capacity C versus temperature T for Na_2IrO_3 below $T = 4$ K. The solid curve through the data shows the T^3 dependence. The inset shows the weak anomaly around 0.8 K and the upturn at lower T.

dilution refrigerator are shown in Figure 3.3. The data in temperature range 2 K to 4 K follow a T^3 behavior shown by the solid curve in Figure 3.3 as expected for a 3-dimensional insulator in the antiferromagnetic state. In this case the T^3 contribution to the heat capacity comes from a combination of phonons and antiferromagnetic spin-waves. If we subtract the T^3 contribution from the $C(T)$ data, a clear anomaly is observed at $\approx$ 0.8 K as shown in the inset of Figure 3.3. The entropy under this peak however, is quite small ($\leq$ 1%Rln2) suggesting it can be extrinsic in origin. The C/T versus T data at lower temperatures show an upturn below about 1 K shown in Figure 3.2(a). This upturn could be the start of a nuclear Schottky anomaly.

3.4.2 Li_2IrO_3

The heat capacity divided by temperature C/T versus T data for Li_2IrO_3 are shown in Figure 3.4(a) between T = 90 mK and 120 K. The lattice contribution, estimated by measuring the heat capacity of the isostructural non-magnetic material Li_2SnO_3 and rescaling the temperature (T) data to account for the difference in molecular masses of Li_2IrO_3 and Li_2SnO_3, is also shown in Figure 3.4(a). The 15 K anomaly signalling the onset of long-ranged zig-zag magnetic order is clearly visible as is a weak shoulder around 7 K. This shoulder below the main magnetic anomaly has been observed for

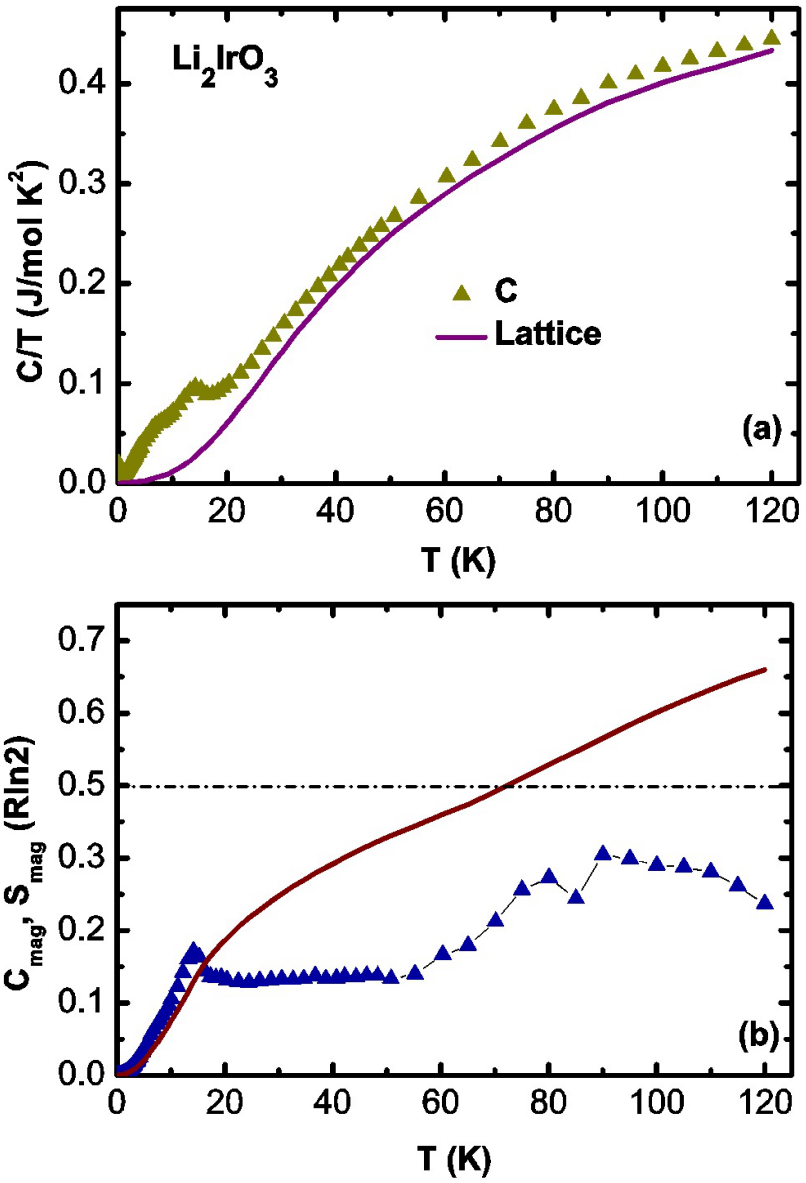

FIGURE 3.4: (a) Heat capacity divided by temperature C/T versus T for Li_2IrO_3. The lattice contribution to the heat capacity is shown as the solid curve. (b) Magnetic contribution to the heat capacity C_{mag} and the magnetic entropy S_{mag} in units of Rln2 versus T for Li_2IrO_3. The horizontal dash-dot line is the value $\frac{1}{2}$Rln2.

all previous polycrystalline samples as well [34, 86]. This second anomaly is most likely associated with disorder as its relative magnitude compared to the 15 K anomaly can be suppressed by improving the quality of the samples [86]. It must be noted however that the second anomaly cannot be completely suppressed even for the best samples (including single crystals [87]) and our current sample is at least as good as the best polycrystalline samples produced thus far [34, 86]. As for Na_2IrO_3, the low-T data for Li_2IrO_3 show an abrupt upturn below about 1 K. We will discuss the low temperature data for Li_2IrO_3 later.

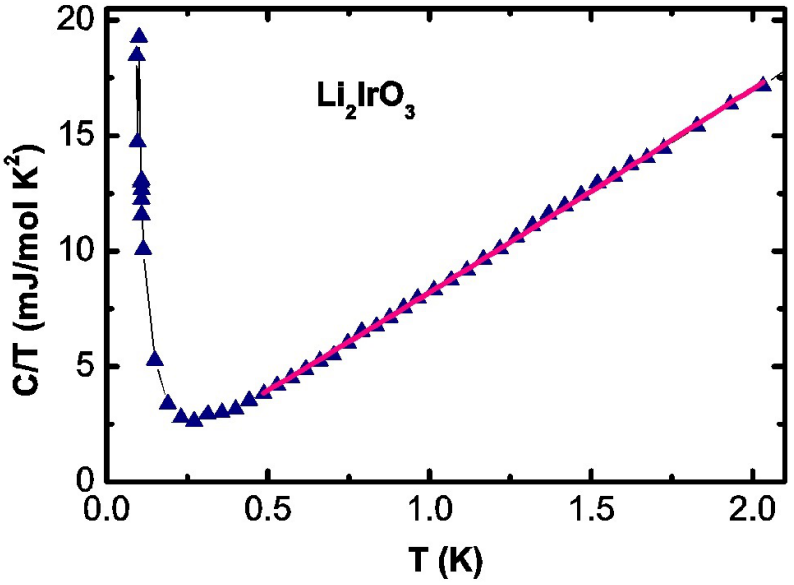

FIGURE 3.5: C/T vs T for Li_2IrO_3 below 2 K. The solid curve through the data shows the $C \sim T^2$ dependence.

The C_{mag} data for Li_2IrO_3 obtained by subtracting the lattice part from the total $C(T)$ is shown in Figure 3.4(b). Although there is more scatter in the obtained data compared to Na_2IrO_3, the two-peak structure in $C_{mag}(T)$ is clearly visible for Li_2IrO_3 too. The two peaks occur at 15 K and $\sim$ 90 K, respectively. The magnetic entropy change S_{mag} shown in Figure 3.4(b) also shows a shoulder between the two peaks although the quantitative match with predictions are not as strong as for Na_2IrO_3. Specifically, the S_{mag} value between the two heat capacity peaks reaches only about 35% Rln2 and the value $\frac{1}{2}$Rln2 is reached only close to the start of the high temperature peak. The value of S_{mag} up to 120 K is only about 65%Rln2 and it seems unlikely that the rest will be recovered under the tail of the high temperature peak beyond 120 K. The possibility that Li_2SnO_3 isn't a good approximation for the lattice heat capacity for Li_2IrO_3 presents itself. Nevertheless, the $C_{mag}(T)$ data with the two-peak structure and the $S_{mag}(T)$ with a plateau between the two peaks are qualitatively consistent with predictions for materials close to Kitaev's QSL [61].

Low temperature C/T versus T data for Li_2IrO_3 measured down to T = 90 mK are shown in Figure 3.5. Below 2 K the C/T data follow a linear in T behaviour down to about 0.3 K where an abrupt upturn is observed. This upturn could again be the high temperature tail of a nuclear Schottky anomaly. The $C \sim T^2$ behaviour for Li_2IrO_3 is unusual and suggests different magnetic excitations compared to Na_2IrO_3 which shows

a conventional $C \sim T^3$ behaviour.

3.5 High Pressure Magnetic Susceptibility of Na_2IrO_3

We have measured the magnetic susceptibility χ versus T for Na_2IrO_3 under externally applied pressure P of upto $P \approx 1$ GPa using an mcell piston-clamp kind of cell. The sample was loaded into a small teflon bucket filled with a pressure transmitting medium (Daphne oil). As a manometer, superconducting lead (Pb) was inserted into the cell with the sample and the change in its superconducting critical temperature with pressure was used to determine the pressure inside the cell. An example of the shift in the T_c for Pb on the application of pressure is shown in the magnetic moment m versus T plot shown in Fig. 3.6. The inset in Fig. 3.6 shows the dm/dT vs T data which shows sharp peaks at temperatures which were taken to be the T_c for Pb at the corresponding pressure.

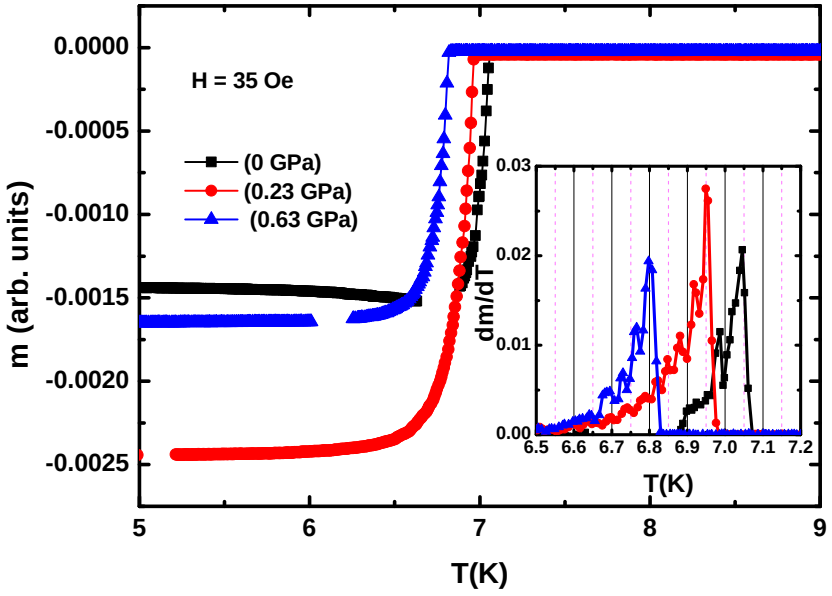

FIGURE 3.6: The magnetic moment versus temperature data for Pb at different pressures measured in a applied magnetic field of H = 35 Oe. The inset shows dm/dT versus T data.

The total magnetic susceptibility of the pressure cell and the polycrystalline Na_2IrO_3 sample $\chi(cell + sample)$ versus temperature T data measured at various pressures P are shown in Figure 3.7. The amount of sample that we can accommodate in the cell is small (m = 13.6 mg) therefore the data are noisy and most likely have significant contributions from the cell. However the paramagnetic behaviour at high temperature and a clear

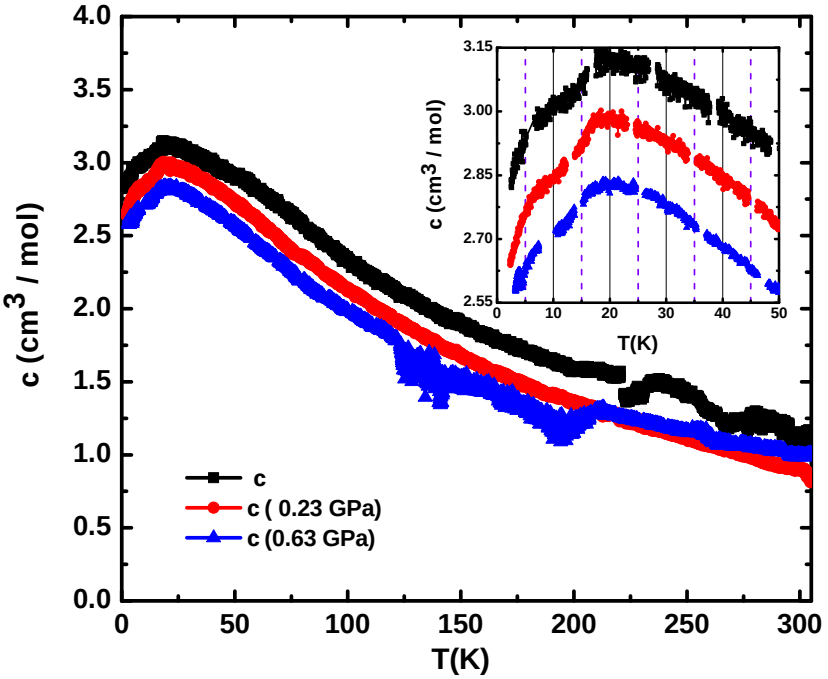

FIGURE 3.7: The susceptibility $\chi(cell + sample)$ versus temperature (T) data at different pressure measured in a applied magnetic field of H = 2 Tesla. The inset shows $\chi(cell + sample)$ v/s T data between $T = 2$ K and 50 K.

downturn in χ at the antiferromagnetic transition at $T_N = 15$ K can clearly be seen from the data. The transition temperature can be seen from the low temperature data shown in the inset in Fig. 3.7. Although the data at high temperatures are too noisy to analyse with a Curie-Weiss fit, the following qualitative conclusions can be drawn. The absolute intensity of magnetic susceptibility $\chi(cell + sample)$ quantitatively decreases with applied pressure although the local moment behaviour is maintained. This suggests that although the local moments are robust at the applied pressure, the magnetism may be weakening. Additionally, the maximum in the susceptibility data which we identify to be the T_N stays at ≈ 15 K up to $P \approx 0.65$ GPa as shown in Figure 3.7 inset. A recent high pressure study on γ-Li_2IrO_3 has also found that the transition temperature doesn't change upto $P = 1.5$ GPa but abruptly disappears above this pressure [88].

We have also studied the structural properties of A_2IrO_3 (A= Na, Li) under high pressure in collaboration with the University of Tel Aviv and these results are discussed in Appendix-A.3.

3.6 Summary and Discussion

We first set out to discover the optimal synthesis condition which gives us high quality polycrystals of A_2IrO_3 (A = Na, Li) and single crystal of Na_2IrO_3. We then measured the magnetic susceptibility χ versus temperature T between 2–1000 K and heat capacity measurement in temperature range 0.075 K $\leq T \leq$ 155 K.

Our measurements provide three new results:

▶ The high temperature $\chi(T)$ data gave the Weiss temperatures $\theta = -127(4)$ K and $-105(2)$ K for Na_2IrO_3 and Li_2IrO_3, respectively. While θ for Na_2IrO_3 is similar to values obtained previously using lower temperature (T = 2 K-300 K) $\chi(T)$ data [1, 34], the θ for Li_2IrO_3 is larger by a factor of 3 compared to the values found using lower temperature $\chi(T)$ data [34]. This indicates that, the magnetic energy scales for the two materials, contrary to what was believed earlier, could be quite similar. This is significant and will help constrain exchange parameters used in future theoretical modelling of these materials.

▶ The magnetic contribution to heat capacity C_{mag} shows a two-peak structure and the entropy change S_{mag} shows a plateau between the two peaks with a value close to $\frac{1}{2}$Rln2 for Na_2IrO_3. This is evidence for the fractionalization of spins into Majorana Fermions as predicted recently [61, 84] and provides the first thermodynamic evidence for the proximity of Na_2IrO_3 to Kitaev's QSL. The results for Li_2IrO_3 are qualitatively similar although quantitative agreement is not as strong.

▶ The low temperature C behaviour for Na_2IrO_3 and Li_2IrO_3 show very different T dependence. While $C(T)$ for Na_2IrO_3 shows a conventional T^3 behaviour, $C(T)$ for Li_2IrO_3 shows a clear T^2 dependence suggesting novel 2-dimensional magnetic excitations for this material which is quite unexpected.

▶ The magnetic susceptibility was measured at different pressure ($P = 0, 0.23, 0.63$ GPa). Local moment behaviour is robust and the Néel temperature also does not change in this pressure range.

Chapter 4

Magnetic impurity doping at Ir site of Na_2IrO_3

4.1 Introduction

The minimal Hamiltonian required to understand the magnetic properties is still under debate. The magnetism of Na_2IrO_3 has been discussed in terms of the Kitaev-Heisenberg model and various extensions. The zig-zag magnetic ordering observed in the Na_2IrO_3 can not be captured within a nearest-neighbor Kiteav-Heisenberg model [6], unless ferromagnetic (FM) Heisenberg and antiferromagnetic (AF) Kiteav exchange couplings are used [6, 7]. It has also been shown that an extended Heisenberg model including upto third nearest-neighbor interactions can give the zig-zag magnetic order [34]. Thus even the nature and range of magnetic exchange interactions is not settled.

Recently there is direct evidence of dominant bond directional exchange interactions in Na_2IrO_3 suggesting that Kitaev like exchanges maybe realized in this system [13]. It is of interest to ask how the novel exchanges in Na_2IrO_3 will change or respond under various perturbations like charge doping, externally applied pressure, etc. Recently there has been a theoretical study [89] predicting spin glass behavior in depleted honeycomb lattice iridates which was later experimentally confirmed by the non-magnetic dilution of A_2IrO_3 (A = Na, Li) by the partial replacement of Ir with non-magnetic Ti [38]. This study revealed the importance of near-neighbor exchange in Na_2IrO_3 while in Li_2IrO_3 further than nearest-neighbor interactions were found to be consistent

with their observations of a magnetic or spin-glass temperature which was suppressed at the percolation limit in the Na case but which persisted beyond this limit for the Li system [38]. Substituting Ir by another magnetic ion of a different spin and with different spin-orbit coupling strength might also shed light on the nature and range of exchange interactions. In a normal magnetic material one would expect the long ranged magnetic order to survive small substitution by another magnetic ion because one is not cutting the magnetic exchange pathways as in the case of site dilution by non-magnetic ions. However, for a Kitaev magnet, with bond directional exchange, substitution with an ion of a different SO coupling leads to cutting of the Kitaev exchange pathways. Thus, a magnetic impurity doping study in these materials would be interesting. A recent Ru substitution study in Li_2IrO_3 has been reported [63]. In Li_2IrO_3, the long ranged antiferromagnetic order observed at $T_N = 15$ K is suppressed to lower temperatures on increasing Ru content untill it is suppressed to below $T = 2$ K for a Ru content of $x = 0.30$ [63]. The LRO surviving for such large Ru substitutions suggests that nearest-neighbor exchange and spin-orbit coupling may not be the most important factors in deciding the magnetism of Li_2IrO_3.

In this chapter, we study the structural, magnetic, and thermal properties of Na_2IrO_3 where Ir was partially replaced by the magnetic ion (Ru^{4+}) of a different spin ($S = 1$). We particularly want to understand how the structural, magnetic, transport, and thermal properties change due to magnetic impurity doping. We have synthesized single crystalline and polycrystalline samples of $Na_2Ir_xRu_{1-x}O_3$ (x = 0, 0.05, 0.1, 0.15, 0.2, 0.3, 0.5) and investigated their crystal structure, electrical resistivity, dc magnetic susceptibility, ac magnetic susceptibility, and heat capacity.

We found that, the antiferromagnetic long-range magnetic ordering of the parent Na_2IrO_3 is replaced by a frozen spin glass state even for the smallest substitution of Ru ($x = 0.05$). These results suggest that the nature of magnetic ordering is extremely fragile with several competing magnetic states being most likely present. Additionally, this points to the importance of nearest-neighbor exchange and the role of strong spin-orbit coupling in determining the magnetic ground state in Na_2IrO_3.

4.2 Crystal structure and chemical analysis

The powder x-ray diffraction (PXRD) data of all single phase samples has been indexed with the C2/m space group were obtained at room temperature using a Rigaku diffractometer with Cu K_α radiation/ wavelength = 1.54056 $\mathring{A}$. The results of the Rietveld refinement for the x = 0.1, 0.5 polycrystalline samples are shown in the given Figure 4.1. The structural parameters obtained from these refinements are given in Table 6.1. For the single-crystalline samples, a full refinement of the single-crystal data was not possible because of presence of multiple twins rotating around the c^* axis in the crystal measured.

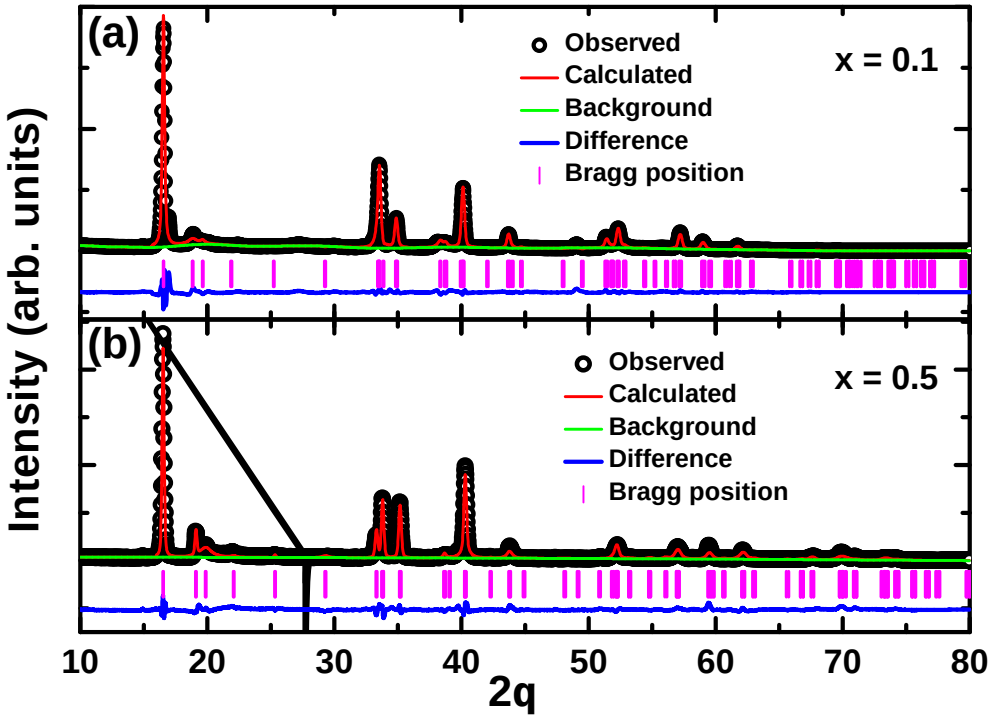

FIGURE 4.1: Rietveld refinements of powder x-ray diffraction data for the samples (a) x = 0.1 and (b) x = 0.5. The open symbols represent the observed data, the solid lines through the data represent the fitted pattern, the vertical bars represent the peak positions, and the solid curve below the vertical bars is the difference between the observed and the fitted patterns.

However, the space group and lattice parameters could be obtained. The unit cell parameters extracted from single crystal or powder x-ray diffraction are listed in the given Table 4.2. We found that the unit cell parameters do not change monotonically as increasing amounts of Ru are introduced into the $Na_2Ir_xRu_{1-x}O_3$ system. From the unit cell parameters for the $x = 0.05, 0.1$ it can be seen that, the a and b cell parameters reduce with increasing Ru concentration while the c-axis parameter does

TABLE 4.1: Wyckoff position for $Na_2Ir_{1-x}Ru_xO_3$ (x = 0.1, 0.5) obtained from Rietveld refinements of x-ray data at room temperature

.

x = 0.1	*Atom*	*Wyckoff*	*x*	*y*	*z*	*Occ*	*B* (Å)
	Ir	4g	0.000	0.0647(2)	0.000	0.9	0.285
	Ru	4g	0.000	0.860	0.000	0.1	0.285
	Na1	2a	0.000	0.000	0.000	1	0.072
	Na2	4h	0.000	0.186(3)	0.5	1	0.027
	Na3	2d	0.000	0.5	0.5	1	0.0403
	O1	8j	0.212(1)	0.357(1)	0.619(6)	1	1
	O2	4i	0.958(4)	0.000	0.198(1)	1	0.003
x = 0.5	*Atom*	*Wyckoff*	*x*	*y*	*z*	*Occ*	*B* (Å)
	Ir	4g	0.000	0.596(6)	0.000	0.5	0.500
	Ru	4g	0.000	0.812(7)	0.000	0.5	0.500
	Na1	2a	0.000	0.000	0.000	1	0.185
	Na2	4h	0.000	0.162(3)	0.5	1	0.028
	Na3	2d	0.000	0.5	0.5	1	0.033
	O1	8j	0.174(6)	0.359(5)	0.654(2)	1	0.21
	O2	4i	0.909(5)	0.000	0.252(3)	1	0.025

not change significantly. This, indicates that for small x the hexagon's shrinks in-plane in the honeycomb lattice while the inter-layer separation stays almost the same as Ru is partially substituted at the Ir site. However, for $x = 0.20$, a and b lattice parameters increase again. For $x = 0.50$ we found this trend for a and b reverses again. From the ionic sizes of Ru^{4+} and Ir^{4+} one expects the volume to shrink when the smaller Ru^{4+} is replacing the larger Ir^{4+}. Therefore the observed non-monotonic trend in the unit cell parameters is difficult to understand. A recent study reports the synthesis of single crystalline Na_2RuO_3 and they observe that the unit cell parameters are larger than those of single crystal Na_2IrO_3 contrary to expectation from ionic sizes [53]. Chemical analysis on our samples was performed using energy dispersive x-ray spectroscopy (EDX) on several spots of the same crystal and on several crystals. The measured atomic fractions were found to be approximately equal to the target substitutions for all samples.

4.3 DC Magnetic Susceptibility

The dc magnetic susceptibility $\chi = M/H$ versus T data for the single crystalline and polycrystalline samples of $Na_2Ir_xRu_{1-x}O_3$ between $T = 2$ K and 305 K measured in an applied magnetic field $H = 1$ T are shown in the given Figure 4.2. Figure 4.2 (a)

TABLE 4.2: Lattice Parameters of $Na_2Ir_xRu_{1-x}O_3$ from single crystal ($x \approx 0, 0.1, 0.2$) and powder diffraction ($x \approx 0.5$)

x	*Space Group*	*a*	*b*	*c*	β	Cell volume ($\AA(cm^3)$)
0	C2 /m	5.434(3)	9.406(7)	5.610(3)	109.049(4)	271.04
0.1	C2 /m	5.424(1)	9.373(1)	5.617(1)	108.706(5)	270.48
0.2	C2 /m	5.429(4)	9.384(1)	5.643(2)	108.514(3)	272.61
0.5	C2 /m	5.394(2)	9.333(5)	5.685(4)	108.40(6)	271.56

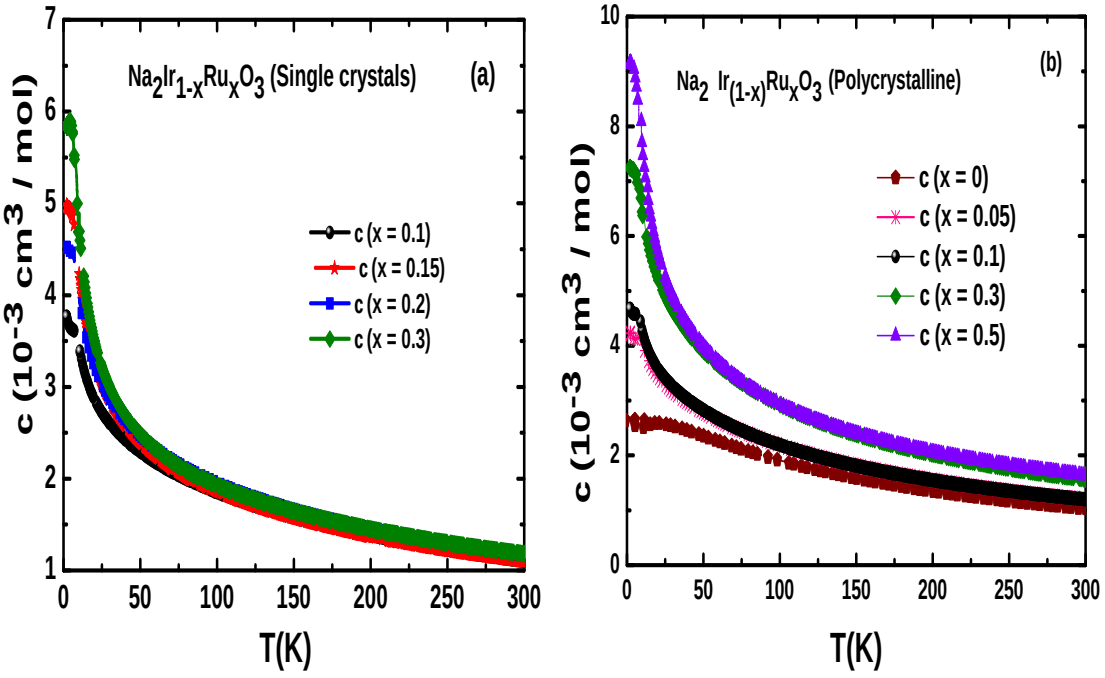

FIGURE 4.2: (a) dc magnetic susceptibility data of single-crystalline $Na_2Ir_{1-x}Ru_xO_3$ (x = 0.1, 0.15, 0.2, 0.3) at applied field H = 1 T and (b) dc magnetic susceptibility data of poly-crystalline $Na_2Ir_{1-x}Ru_xO_3$ (x = 0.1,0.15,0.2,0.3) at applied field H = 1 T.

shows the $\chi(T)$ data for single crystalline samples ($x = 0.10, 0.15, 0.20, 0.30$). The field was applied parallel to the *ab*-plane of the samples. Figure 4.2 (b) shows the $\chi(T)$ data for polycrystalline samples ($x = 0, 0.05, 0.10, 0.30, 0.50$). All samples show the behavior of a system with localized magnetic moments with paramagnetic behavior at high temperatures indicating that Ru substitution does not lead to charge carrier doping in the system. The magnitude of $\chi(T)$ increases with increasing Ru concentration as expected on substituting $S = 1/2$, Ir^{4+} localized moments with $S = 1$, Ru^{4+} localized moments.

The $\chi(T)$ data between $T = 200$ K and 305 K for the polycrystalline samples $Na_2Ir_xRu_{1-x}O_3$ ($x \approx 0, 0.1, 0.3, 0.5$) were fitted by the Curie-Weiss expression $\chi = \chi_0 + \frac{C}{T-\theta}$ where χ_0,

TABLE 4.3: Parameters extract from fits to the magnetic susceptibility data by the Curie-Weiss expression $\chi = \chi_0 + \frac{C}{T-\theta}$

x	χ_0 (10^{-5} cm^3/ mol)	C (cm^3 K/ mol)	θ (K)	μ_{eff} (μ_B)
0	3.1(4)	0.41(7)	-113(1)	1.81(1)
0.1	6.9(1)	0.47(8)	-124(2)	1.94(2)
0.3	18.4(6)	0.56(2)	-105(4)	2.12(4)
0.5	17.8(2)	0.64(4)	-138(1)	2.26(3)

C, and θ are the fitting parameters. The parameters obtained from fits to the data are shown in Table 4.3. Assuming a g-factor $g = 2$, the effective moment μ_{eff} calculated from the obtained value of the Curie constant C are also listed in given Table 4.3. For the parent sample ($x = 0$) the estimated $\mu_{eff} = 1.81(2)$ μ_B is close to the previously reported values [1]. The value of μ_{eff} monotonically increases with increasing Ru substitution. This is as expected if Ir^{4+} ($S = 1/2$) moments are replaced by Ru^{4+} ($S = 1$) local moments. The value of the Weiss temperature θ stays large and negative indicating persisting strong antiferromagnetic interactions for the Ru doped samples.

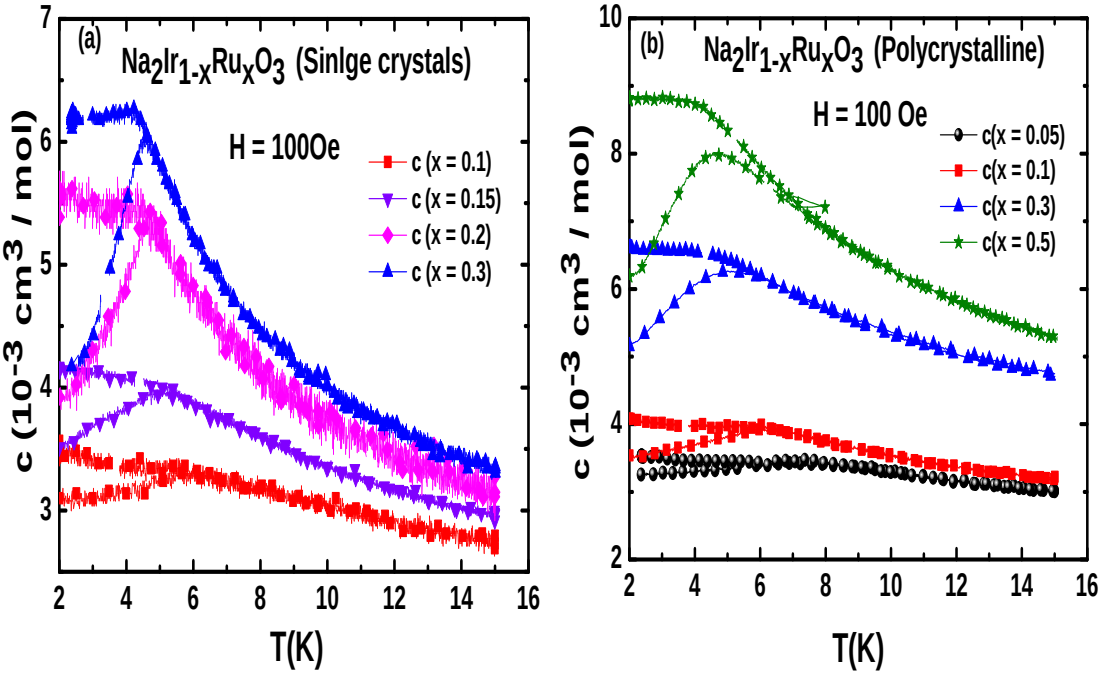

FIGURE 4.3: Zero-field-cooled (ZFC) and field-cooled (FC) magnetic susceptibility χ versus T curves of $Na_2Ir_{1-x}Ru_xO_3$ between T = 2 and 15 K at an applied magnetic field of H = 100 Oe. (a) shows ZFC-FC data of single-crystalline $Na_2Ir_{1-x}Ru_xO_3$ (x = 0.1,0.15,0.2,0.3) at an applied field of H = 100 Oe. (b) shows ZFC-FC data of polycrystalline $Na_2Ir_{1-x}Ru_xO_3$ (x = 0.05, 0.1, 0.3, 0.5) at an applied field of H = 100 Oe.

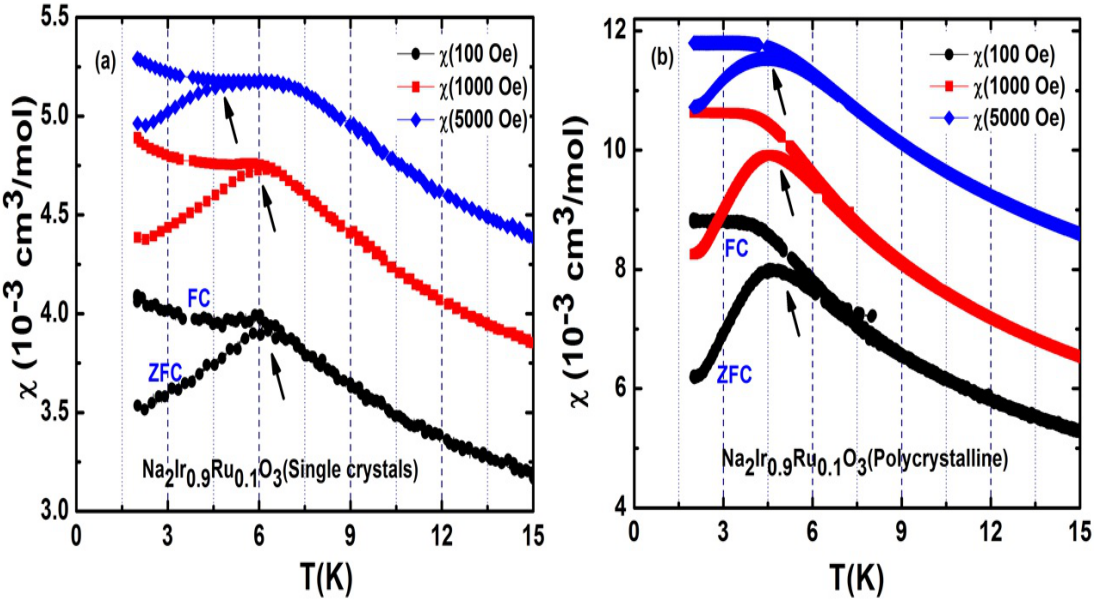

FIGURE 4.4: Zero-field-cooled (ZFC) and field-cooled (FC) magnetic susceptibility χ versus T curves of $Na_2Ir_{1-x}Ru_xO_3$ ($x = 0.1$) between T = 2 and 15 K at different applied magnetic field of (H = 100 Oe, 1000 Oe, 5000 Oe).

To check the effect of Ru substitution on the magnetic order we measured the low field DC magnetic susceptibility at low temperatures. We observe magnetic irreversibility in the ZFC-FC data as shown in Figure 4.3. Figures 4.3 (a) and (b) show the zero-field-cooled (ZFC) and field-cooled (FC) data between $T = 2$ K and 15 K measured in a small magnetic field of $H = 100$ Oe for single crystalline and polycrystalline samples, respectively. The single crystalline samples show a sharp cusp in the ZFC data around a freeing temperature $T_g = 5.5$ K for all Ru substituted samples and there is a bifurcation between the ZFC and FC data below this temperature. A similar behavior is observed for the polycrystalline samples also, although the cusps in the ZFC $\chi(T)$ data are not as sharp and they occur at a slightly higher temperature compared to the single crystalline samples. The rounding of the cusp in the polycrystals maybe due to microscopic inhomogeneity in the Ru substitution in the system. The sharpness of the cusp/anomaly, the extent of bifurcation and the freezing temperature T_g decrease with increasing applied magnetic field as shown in Figure 4.4.

These signatures observed in all Ru substituted samples can be taken as a first indication of a frozen spin glass like state for the doped samples. We track the freezing temperature $T_{\rm g}$, which we define as the peak temperature of the cusp in the low field DC susceptibility, with Ru concentration x for single crystalline and polycrystalline samples. These data

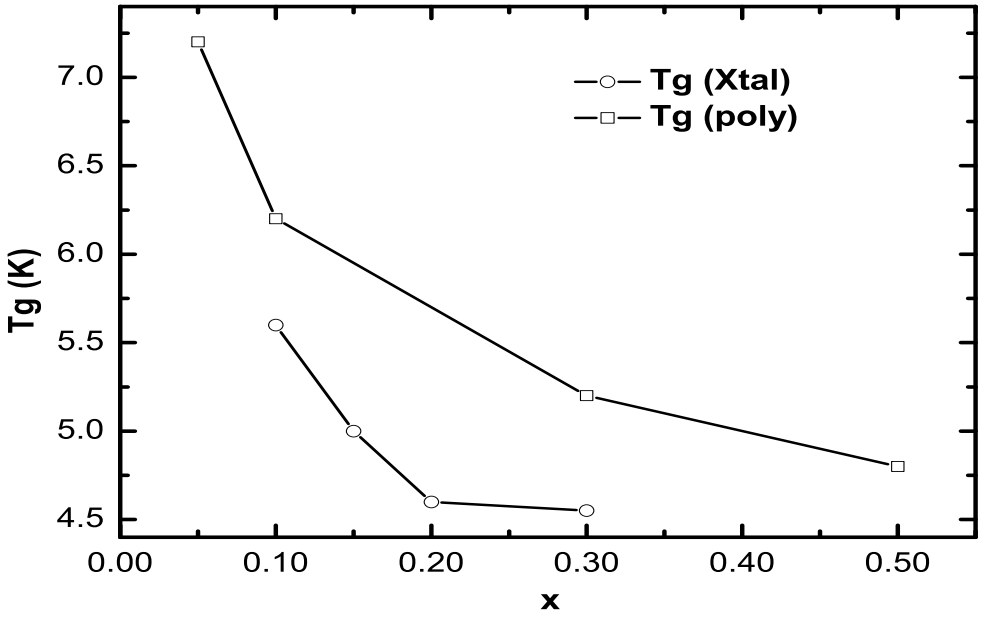

FIGURE 4.5: The freezing temperature T_g as a function of Ru concentration x for single crystalline and polycrystalline samples of $Na_2Ir_xRu_{1-x}O_3$ (x = 0.05, 0.1, 0.15, 0.2, 0.3, 0.5).

are shown in Fig. 4.5. It can be seen that T_g after reducing sharply for small x, tends to saturate to a value similar to $T_g \approx 4.5$ to 4.8 K for both kinds of samples, respectively.

4.4 AC Magnetic Susceptibility

To further support the possibility of spin glass like behavior we have measured ac susceptibility χ_{ac} at various excitation frequencies f for single crystalline and polycrystalline $Na_2Ir_xRu_{1-x}O_3$ samples. The real part of the ac susceptibility χ'_{ac} data between $T = 2$ K and 15 K measured at various f are shown in Figure 4.6 and Figure 4.7 for single crystalline and polycrystalline samples, respectively. A sharp cusp is observed at T_g for both single crystalline and polycrystalline samples at low frequency ($f = 100$ Hz) and match with the cusp temperature observed in the dc ($f = 0$) measurement. The position of this cusp monotonically shifts up in temperature with increasing frequency f as can be seen for all samples in Fig. 4.6 and in Figure 4.7. This shift of the cusp to higher temperatures with increasing frequency is a classic signature observed for example in canonical spin-glasses like Cu-Mn [90] and is strong evidence of a frozen spin-glass like state below T_g in our Ru substituted samples.

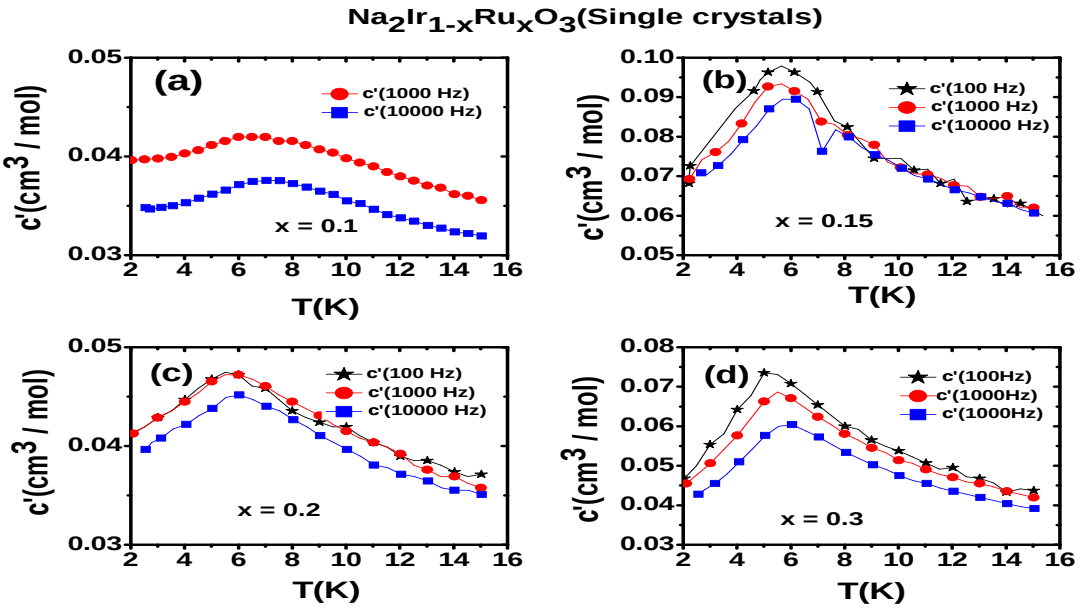

FIGURE 4.6: The real part of ac susceptibility χ'_{ac} as a function of temperatures T = 2 and 15 K at different frequencies for single-crystalline $Na_2Ir_{1-x}Ru_xO_3$ (x = 0.1,0.15,0.2,0.3

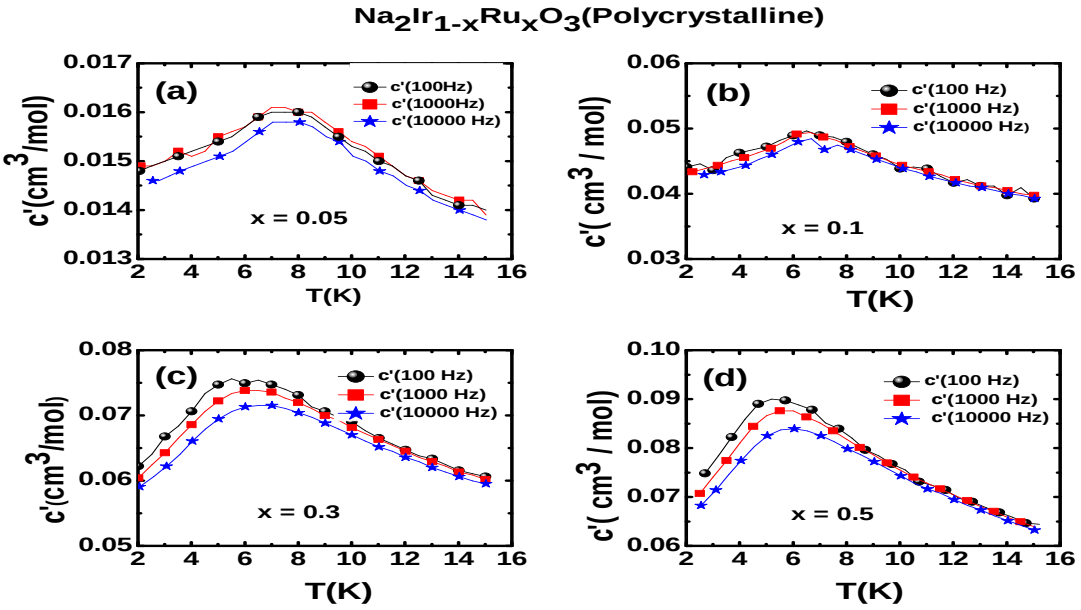

FIGURE 4.7: The real part of ac susceptibility χ'_{ac} as a function of temperatures T = 2 and 15 K at different frequencies for polycrystalline $Na_2Ir_{1-x}Ru_xO_3$ (x = 0.1,0.15,0.2,0.3

A quantitative measurement of the shift in the peak position with frequency is usually made using the ratio $\frac{\Delta T_g}{T_g \Delta log(f)}$, where ΔT_g is shift in the freezing temperature T_g and $\Delta log(f)$ is the decade change in the frequency f. The value of the ratio $\frac{\Delta T_g}{T_g \Delta log(f)}$ obtained for the single crystalline and polycrystalline samples of $Na_2Ir_xRu_{1-x}O_3$ ($x \approx 0, 0.05, 0.1, 0.15, 0.2, 0.3, 0.5$) are given in Table 4.4. These values are typical of what

TABLE 4.4: Parameters obtained from the calculation for $f = 100$ Hz and 10 kHz by using the ratio $\frac{\Delta T_g}{T_g \Delta log(f)}$

x	Polycrystalline ($\frac{\Delta T_g}{T_g \Delta log(f)}$)	Single crystals ($\frac{\Delta T_g}{T_g \Delta log(f)}$)
0		
0.05	0.039(3)	
0.1	0.014(3)	0.015(4)
0.15		0.055(5)
0.2		0.048(1)
0.3	0.09(1)	0.10(4)
0.5	0.16(5)	

has been observed for other insulating spin glasses like $Eu_xSr_{1-x}S$ ($\frac{\Delta T_g}{T_g \Delta log(f)} \approx 0.06$) and $Fe_xMg_{1-x}Cl_2$ ($\frac{\Delta T_g}{T_g \Delta log(f)} \approx 0.06$). But these values are much larger than the value observed in canonical metallic spin glass like CuMn ($\frac{\Delta T_g}{T_g \Delta log(f)} \approx 0.005$) [91].

4.5 Heat Capacity

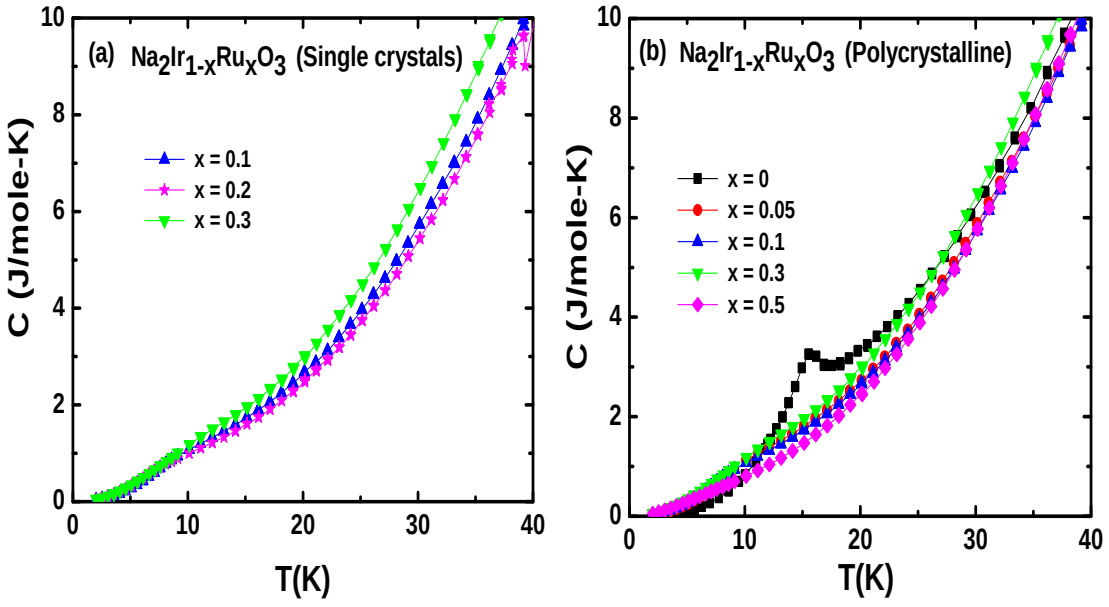

FIGURE 4.8: The heat capacity versus T for (a) crystalline $Na_2Ir_{1-x}Ru_xO_3$ (x = 0.1,0.2,0.3) and (b) polycrystalline $Na_2Ir_{1-x}Ru_xO_3$ (x = 0,0.1,0.3,0.5).

To rule out long range magnetic order as the reason for the sharp anomalies in the magnetic measurements we have measured the heat capacity for some samples. Figure 4.8 and Fig. 4.9 show the heat capacity C versus T data and heat capacity divided by temperature C/T versus T data between $T = 2$ K and $T = 40$ K for the some

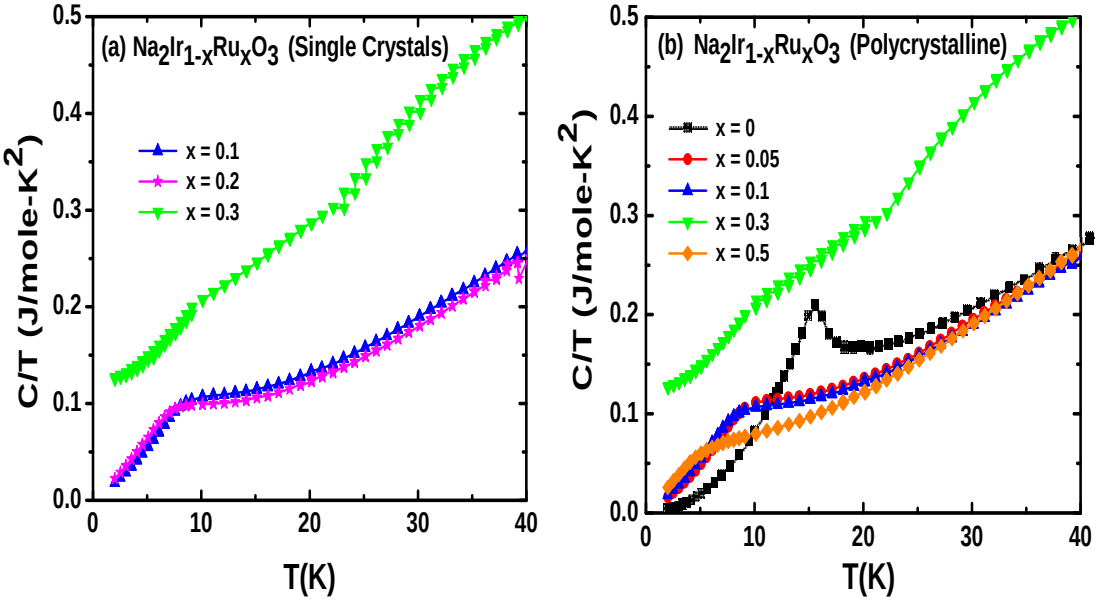

FIGURE 4.9: The heat capacity divided by temperature versus T for (a) crystalline $Na_2Ir_{1-x}Ru_xO_3$ (x = 0.1,0.2,0.3) and (b) polycrystalline $Na_2Ir_{1-x}Ru_xO_3$ (x = 0,0.1,0.3,0.5).

single crystalline and the polycrystalline samples. For comparison, the heat capacity of Na_2IrO_3 crystals are also plotted in these figures. For the Ru substituted samples, there is no signature of any phase transition in $C(T)$ data. Specifically, we do not observe any sharp anomaly at the temperatures at which we observed sharp cusps in the magnetic measurements. Instead, a broad hump is observed with a maximum at a higher temperature $T \approx 10$ K which is 1.4 time of freezing temperature T_g determined from the ZFC-FC magnetization and ac-susceptibility. From these observations we conclude that the anomaly at T_g seen in $\chi(T)$ data does not arise from a bulk magnetic phase transition and confirms absence of long range ordering.

Hence all the above results provide strong evidence for a frozen spin-glass like state below T_g for all Ru substituted samples.

4.6 Summary and Discussion

In summary, we have studied the effect of magnetic impurity substitution on the honeycomb lattice iridate Na_2IrO_3. We have successfully synthesized the single-crystalline and polycrystalline samples $Na_2Ir_xRu_{1-x}O_3(x = 0, 0.05, 0.1, 0.15, 0.2, 0.3, 0.5)$ having a honeycomb lattice of magnetic ions and measured and analyzed their magnetic and electric

properties using DC magnetic susceptibility, AC magnetic susceptibility, and electrical transport, and heat capacity measurements. All samples were found to be local moment insulators. This is in contrast with Ru substituted Sr_2IrO_4 where an insulator to metal change is found on increasing Ru content [92] but is similar to the behavior observed for Ru substituted Li_2IrO_3 [63].

The magnetic behavior of Ru substituted Na_2IrO_3 is however, very different from that of Ru substituted Li_2IrO_3 [63]. In Li_2IrO_3, the long range antiferromagnetic ordering observed at $T_N = 15$ K is suppressed to lower temperatures on increasing Ru content until it is suppressed to below $T = 2$ K for a Ru content of $x = 0.30$ [63]. In contrast, for Na_2IrO_3 we have found that even the smallest Ru substitution of $x = 0.05$ (5%) leads to the long range antiferromagnetic order ($T_N \approx 15$ K) of the parent compound to be replaced by a frozen spin-glass like state.

Hence, our results suggest that the magnetic order in Na_2IrO_3 is very fragile. Even 5% magnetic impurity is enough to introduce a frozen spin glass like state. The emergence of a spin glass state at such small substitutions suggests that modifications in the short ranged magnetic exchange pathways lead to drastic modification of the magnetic ground state. This also highlights an important difference between the Na_2IrO_3 and Li_2IrO_3 systems. Our results indicate that the magnetic behavior and the ground state is driven primarily by near-neighbor exchanges in Na_2IrO_3 since even a small disturbance in the Ir sublattice leads to disorder driven freezing of spins. On the other hand previous results for Ru substitution in Li_2IrO_3 suggest that much longer ranged interactions are at play and these exchange pathways are not affected as drastically by small Ru substitutions. Therefore, the magnetic order in Ru substituted Li_2IrO_3 survives at least upto $x = 0.2$ (20% Ru) while for Na_2IrO_3 even a 5% Ru substitution leads to a frozen spin-glassy state.

It is not completely obvious that a magnetic impurity should lead to a disruption of magnetic exchange pathways. If a non-magnetic impurity is doped into a magnetic lattice, then it becomes obvious that there will be interruptions in the magnetic exchange pathways and a weakening of the average exchange. However, if a magnetic impurity is doped, then the magnetic pathways are intact. So why does Ru substitution lead to a disruption in the NN magnetic exchange pathways. The magnetism in these materials is governed by strong spin-orbit coupling. Infact the local moments in Na_2IrO_3 themselves

have strong spin-orbital character and the superexchange is highly unconventional and Kitaev like because of this [13]. When Ir is replaced by Ru, we are introducing local moments which have reduced spin-orbit character. Thus, introduction of Ru into the lattice, which could have been either a reinforcer or a detterent in a normal magnetic system, leads to a disruption of the NN Kitaev exchange pathways in this Iridate system and leads to disorder driven spin-glassiness. Thus our results also suggest the importance of unconventional magnetic exchange in Na_2IrO_3.

We conclude by noting that there is one report on the magnetic properties and heat capacity measurement on one isolated Ru substitution ($x = 0.20$) in Na_2IrO_3 polycrystals [93]. They conclude that the long-range magnetic ordering shifts from 15 K for Na_2IrO_3 to $\approx$ 6 K for $Na_2Ir_{0.8}Ru_{0.20}$. This conclusion is based on the cusp in the DC magnetic susceptibility. However, we have shown conclusively from magnetic irreversibility in ZFC-FC magnetization and from frequency dependence of AC susceptibility, that this cusp is a signature of a frozen spin-glass-like state and not a signature of long ranged magnetic order.

Chapter 5

Density wave like phase transition in surface doped Na_2IrO_3

5.1 Introduction

The family of layered honeycomb lattice iridates $A_2IrO_3 (A = Na, Li)$ has garnered a lot of attention. In these materials spin-orbit entangled effective moments $J_{eff} = 1/2$ sit on a honeycomb lattice leading to novel magnetic properties [1, 4, 5, 7, 34]. Na_2IrO_3 was found a candidate of spin-orbit Mott insulator with a long range magnetic ordering temperature $T_N = 15$ K [1]. A large Weiss temperature $\theta = -120$ K indicates antiferromagnetic interactions are prominent between the $S_{eff} = 1/2$, Ir^{4+} local moments [1]. Electronic structure of Na_2IrO_3 reveal electrically insulating with a band gap of 340 meV [36]. The magnetic frustration observed in these materials are argued to arise from the presence of dominant bond-directional Kitaev-like exchange interactions with additional Heisenberg exchange present [7, 34, 94]. There is growing evidence of dominant Kitaev like exchanges interaction from inelastic Raman scattering measurement and from dominant bond directional exchange interactions in Na_2IrO_3 [13, 14].

Unconventional spin-triplet superconductivity and topological superconductivity, and spin-triplet pairing have been predicted to emerge with doping in the Kitaev-Heisenberg model on the honeycomb lattice [10, 95–98]. Additionally, spin and charge density wave, spin/charge bond-order instabilities, and electronic dimerization instabilities have been predicted with varying doping as shown in the given Figure 5.1 [10]. The honeycomb

lattice ruthenates and iridates are already close to coupled structural, magnetic, and orbital instabilities as evident by Ru-Ru dimerization in Li_2RuO_3 [12] and in A_2IrO_3 (A =Li, Na) under small pressures [15]. Conventional doping in these compounds has not been successful so far. We were able to tune the electrical transport in Na_2IrO_3 all the way from insulating to metallic (a change of 11 orders of magnitude) by varying the etching times. The samples etched for various times showed anomalous temperature dependence's including behavior consistent with Topological insulators, charge or spin density wave transitions, and structural transitions [64, 65]. Remarkably, some of these features has been predicted for the doped Kitaev-Heisenberg model [10] and a comparison with theory would suggest a specific sign for the Kitaev interaction in this material. This work also provides a new method of doping the surface of other layered materials like Mott insulators or Topological materials.

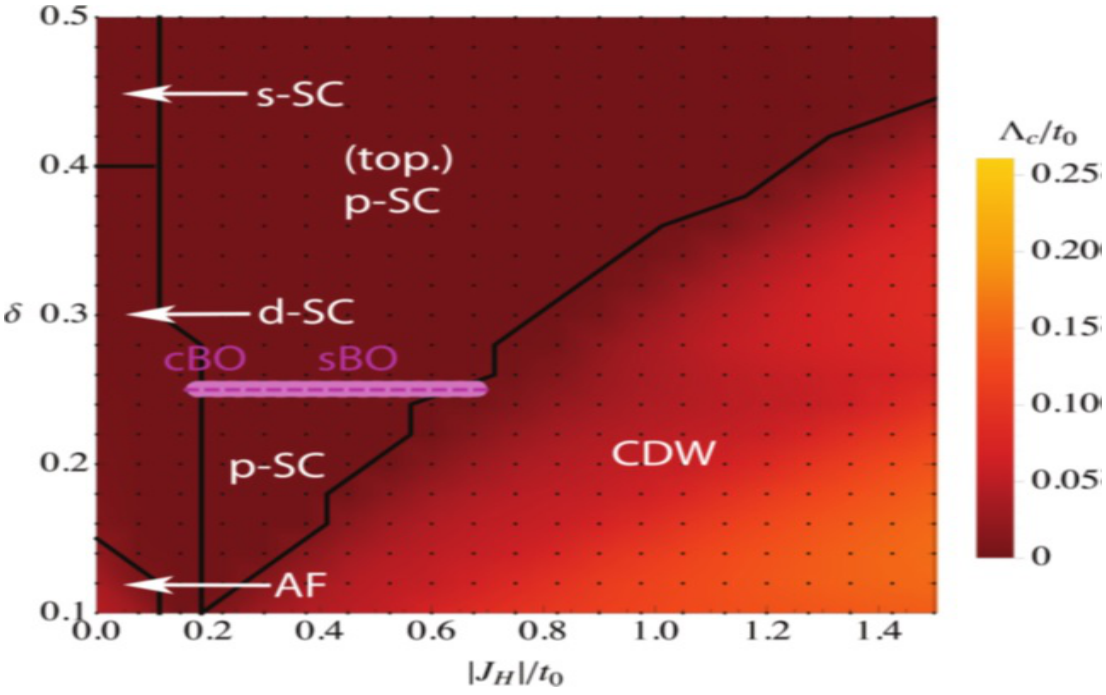

FIGURE 5.1: The phase diagram as obtained from the numerical solution of a (N = 24)-patching scheme with full fRG with $J_K/t_o = 1$. The horizontal axis gives the strength of the ferromagnetic Heisenberg coupling $J_H < 0$ in units of the bare hopping amplitude t_0, while the doping level δ is given on the vertical axis. The color code describes the magnitude of the critical scale Λ_c across the phase diagram. The dashed magenta line marks the van Hove singularity. The magenta shading represents the formation of charge (cBO) and spin bond-order (sBO) instabilities at van Hove filling, as obtained from a (N = 96)-patching scheme reprinted from [10].

In this chapter, we explore the properties of surface doped Na_2IrO_3 crystals. We have however, discovered that the surface of these crystals can be doped by Argon plasma etching [64]. We report temperature and magnetic field dependent electrical transport

studies on Na_2IrO_3 crystals where surface was modified by plasma etching. We have succeeded in turning the surface of Na_2IrO_3 metallic by Ar plasma etching which leads to the removal of Na from the surface. Surface doping was performed by the bombardment of high energy Ar ions on the single crystal of Na_2IrO_3. The surface of the Na_2IrO_3 single crystal is extremely tunable with plasma etching.

5.2 Experimental Details

Single crystals of Na_2IrO_3 were synthesized using self-flux method as described in detail in chapter 2. The surfaces of the platelike crystals were modified by bombarding a freshly cleaved surface with high-energy Ar plasma for varying amounts of time ranging from 0 to 40 min. Reactive Ion Etching technique was used for the modified the surface of the Na_2IrO_3 crystals.

5.2.1 Reactive ion etching (RIE)

Reactive ion etching (RIE) is a technique which is used for micro-fabrication on the wafer. RIE is a type of dry etching which uses chemically reactive plasma to remove material from the deposited on wafers. The plasma is generated under low pressure (vacuum) by an electromagnetic field. Accelerated high-energy ions from the plasma attack the wafer surface and knockout the atom or ion from the surface of the wafer.

RIE system consist of a vacuum chamber, where a wafer platter is situated in the bottom part of the chamber. Wafer platter is electrically isolated from the rest of the chamber. A particular gas enters through a small inlet at the top of the chamber and exits through vacuum pump of the bottom. The types and amount of gas used vary depending upon the etch process. Gas pressure is typically maintained in a range between a few mTorr and a few hundred mTorr by adjusting gas flow rates. The details of parameter used for the reactive ion etching treatment are given the table 5.1.

5.2.2 Grazing Incidence Small Angle X-ray Scattering (GISAXS)

The surface structure of the single crystal of Na_2IrO_3 measured using grazing incidence small angle x-ray scattering (GISAXS). GISAXS was performed before and after plasma

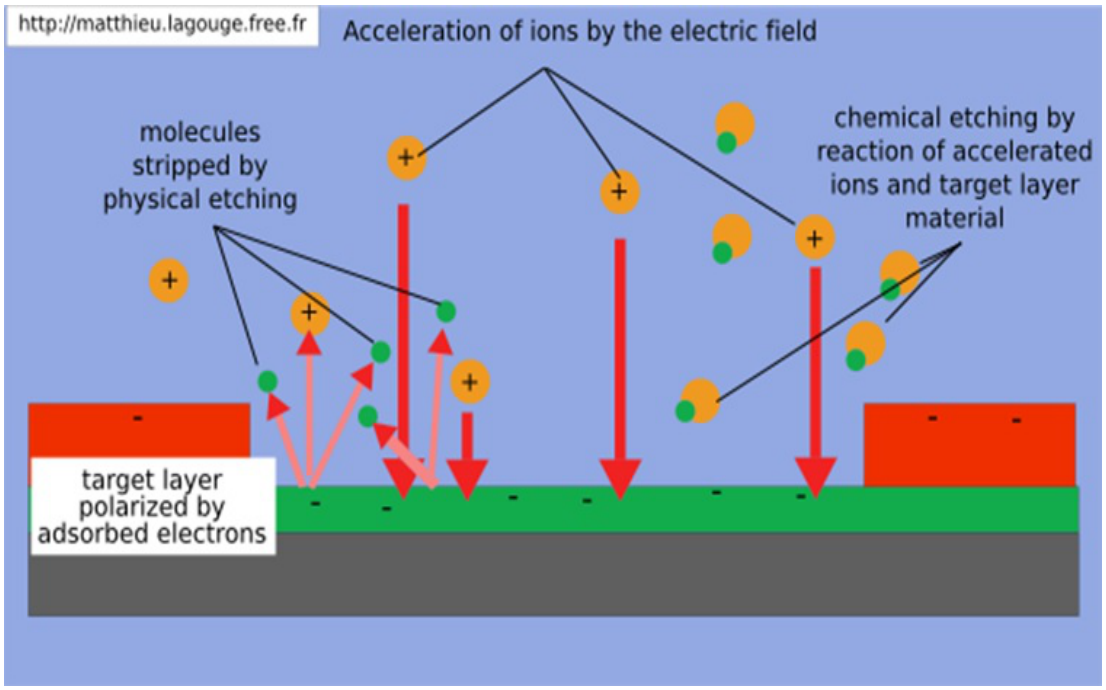

FIGURE 5.2: A schematic diagram of reactive ion etching setup reprinted from [11]

TABLE 5.1: Parameters from reactive-ion etching

Flow of Ar gas	80 SCCM
Chamber Pressure	80 mTorr
RF Power	200 W
RF Bias voltage	-500 V
Temperature	10 - 20 °C

etching of the crystals and suggests that the overall surface structure does not change after plasma treatment. The most significant change is for the peak at high angles (33–34^o) which shifts to slightly smaller angles after plasma etching. This shifted peak suggest that the unit cell parameter increases. Representative GISAXS analysis of two samples before and after the plasma etching are shown in Figure 5.3 and Figure 5.4. For all etched samples, the peak position is approximately the same and smaller (in angle) than the corresponding peak in the unexposed Na_2IrO_3 surface by $\approx 0.5^o$. We have looked at systematic evolution the surface structure of Na_2IrO_3 before and after the etching. The depth D probed by GISASX measurement is given as $D = dsin\theta$ where d is the attenuation length for this compound at the given x-ray energy and θ is the incidence angle measured from the surface. We estimated $D \approx 20$ nm with $d \approx 1.25 \times 10^{-3}$ cm at an x-ray energy of 15 keV and $\theta = 0.1^o$. Since the thickness of the surface layer modified by the RIE is unknown and probably depends on the exposure time of plasma etching,

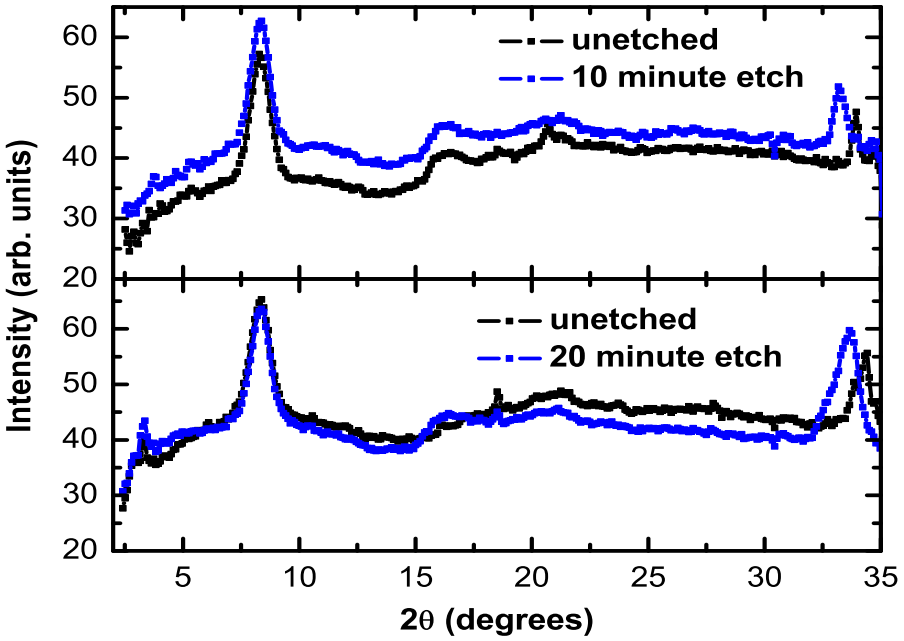

FIGURE 5.3: Grazing incidence small angle x-ray scattering patterns for Na_2IrO_3 before and after varying periods of 10 min and 20 min etching using an Ar plasma

D estimated above can be used as a lower limit.

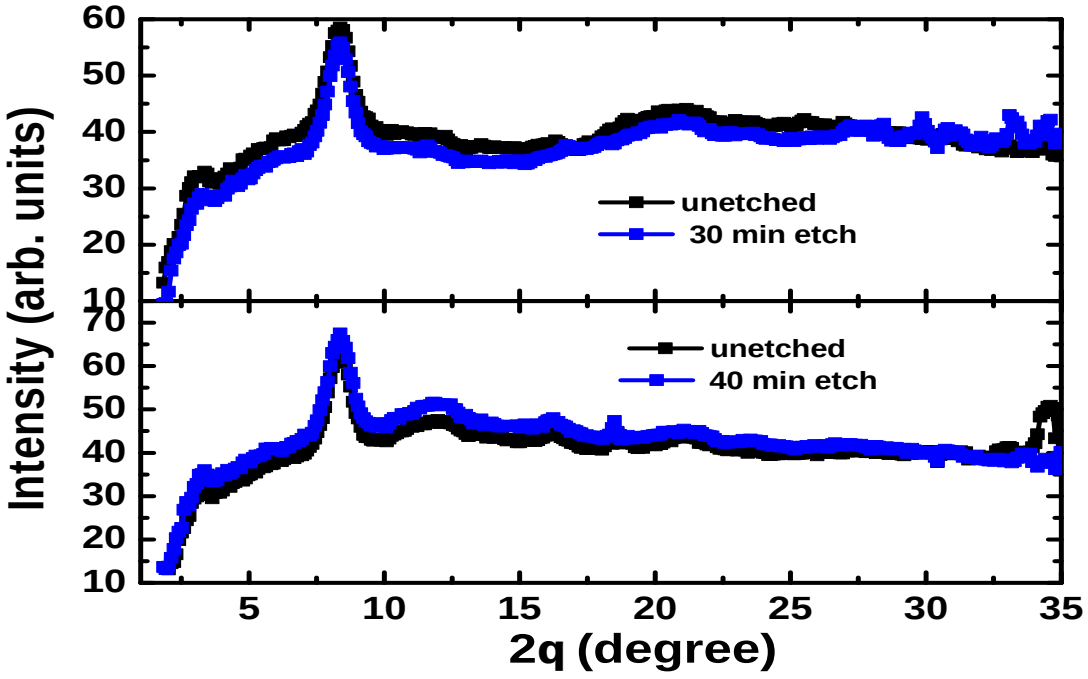

FIGURE 5.4: Grazing incidence small angle x-ray scattering patterns for Na_2IrO_3 before and after varying periods of 30 min and 40 min etching using an Ar plasma

The chemical composition of the sample surface before and after the plasma treatment was checked using energy dispersive x-ray (EDX) analysis with a JEOL scanning electron

microscope (SEM) as shown in the given table 5.2. from the EDX analysis it is clear that Na is progressively depleted from the crystals with increasing etching time. Thus, the plasma etching leads to hole doping in the crystals (atleast on the surface).

TABLE 5.2: Average ratio of desired elements from Energy dispersive x-ray analysis

Exposure time(min.)	Average Na	Average Ir
0	1.76	1
10	1.73	1
20	1.68	1
30	1.62	1
40	1.56	1

5.3 Result and Discussion

During the measurements and RIE of the Na_2IrO_3 samples, we followed lot of caution which are summarized in the following points. The surface of the etched samples is very sensitive to the ambient lab atmosphere. The change in the transport behaviour of etched sample samples are thus, temporary and revert back to their original (insulating) behaviour after exposure to lab atmosphere. The 10-minutes-etched samples degrade and revert back to insulating behaviour in about 1–2 days. The lab exposure time of the samples after which they degrade gets shorter and depends on the time they were etched for, the samples etched for a 30 minutes and 40 minutes degrade very fast, (within 1–2 hours). It was found that opposite surface of the etched sample does not change and remains highly insulating. Additionally, we found that if we cleave off the etched surface of the sample and then measured the transport behaviour, it showed insulating behaviour similar to undoped Na_2IrO_3 sample. These observation suggest that only small depth of the Na_2IrO_3 samples was affected by the plasma etching. This depth is varies with the time of plasma etching. The electrical transport for 10 min, 20 min, 30 min, and 40 min etched samples was measured using a Quantum Design physical property measurement system (PPMS) in the temperature range 2 K to 305 K.

5.3.1 Electrical transport 10 minute etched samples

We present electrical transport for the etched samples as sheet resistance R_s in the units Ω/sq. A square sheet with a sheet resistance of 10 Ω/sq will have a resistance 10 Ω. The resistivity ρ versus temperature T data of unetched samples and sheet resistance R_s versus temperature T data of the 10 minute etched samples shown in the Figure 5.5. Figure 5.5 show the ρ versus T data of the unetched Na_2IrO_3 single crystal between $T = 50$ and 305 K. The $\rho(T)$ data confirms the insulating behavior in the Na_2IrO_3 sample as has been reported in literature [1].

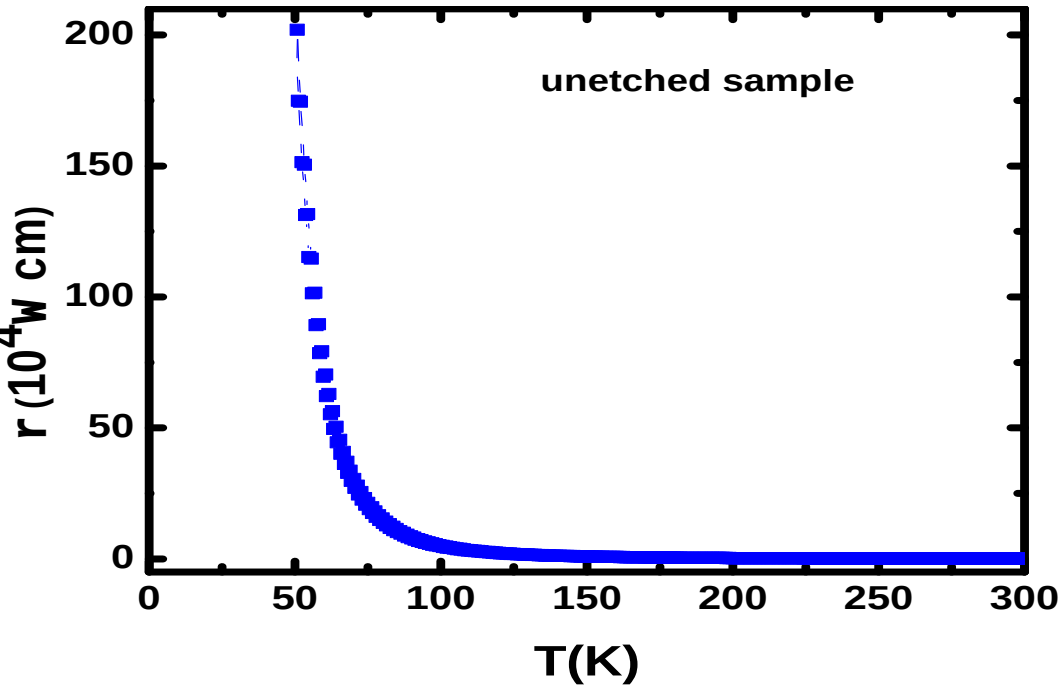

FIGURE 5.5: The electrical resistivity ρ versus temperature T for unetched Na_2IrO_3 crystal at zero magnetic field.

Figure 5.6 shows the sheet resistance R_s versus T data for the 10 minutes etched for two different single crystals recorded while cooling the sample down from $T = 305$ K to 2 K and while warming back up again. Although the R_s values for the two samples are different by about an order of magnitude, the qualitative T dependence is very similar with an increases on cooling from $T = 300$ K, and reaches at a broad maximum around 150–200 K, after which the R_s is very weakly T dependent. For the sample with the lower resistance, the behavior below the maximum is like metallic behavior. This type of transport behavior is consistent with expectation for topological insulators where the insulating bulk dominates the transport at high temperature and the surface states start contributing at lower temperatures when the bulk becomes sufficiently insulating.

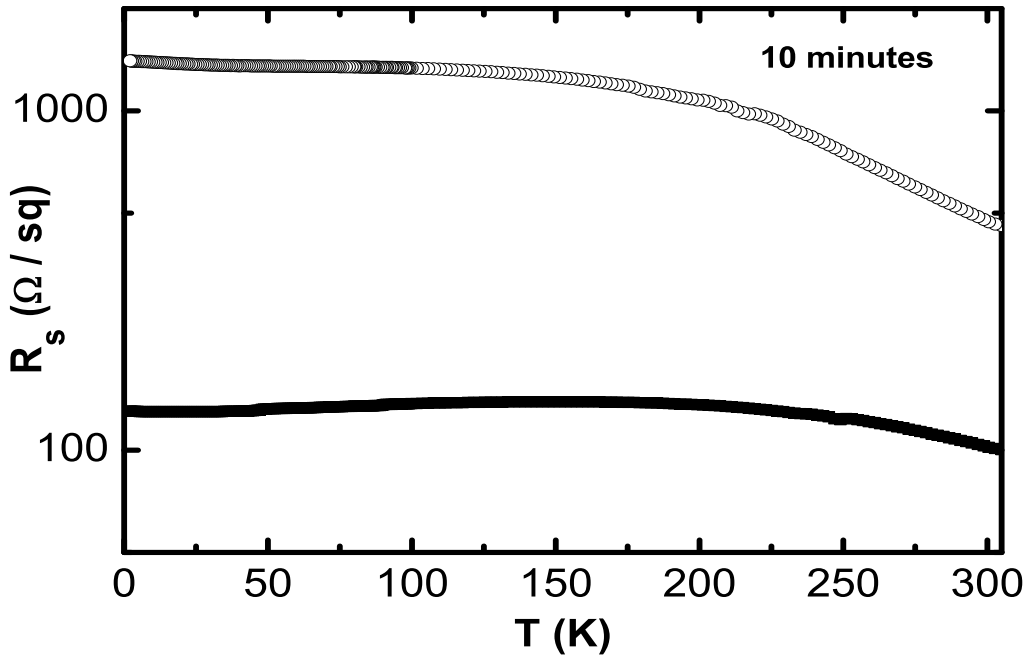

FIGURE 5.6: A semilogarithmic plot of electrical transport as sheet resistance R_s versus temperature T for two samples of Na_2IrO_3 after 10 minutes of plasma etching.

Such a topological insulating state has been predicted for the Na_2IrO_3 under certain conditions [33, 94]. We found there was a small increase in resistance at low temperature. We believe that this weak upturn is arises from weak localization of the doped carriers due to the disorder introduced by the plasma etching process. A non-monotonic electrical transport behaviour is also observed due to a crossover from a larger intrinsic gap at high temperatures to a smaller dopant gap at low temperatures in doped semiconductors or insulators. A prominent example of this is the correlated insulator $NiS_2 - xSe_x$ [99]. There is small hysteresis in the warming and cooling curve which is not understood at present. Whether this type of behaviour in doped Na_2IrO_3 has topological properties will have to be explored in more detailed surface sensitive studies in future.

5.3.2 Electrical transport 20 minute etched samples

Figure 5.7 shows the zero magnetic field $R_s(T)$ data measured while cooling and warming the sample exposed for 20 minutes. The sheet resistance increases on cooling below 300 K and reaches a maximum around 240 K. There is a transition involved an step like increase around at $T_o \approx 220$ K in the R_s. Below T_o, there is a rapid decrease in sheet resistance suggesting metallic behaviour down to 20 K, after which there is a

slight increase in R_s is observed again. This observed upturn is stronger than the upturn observed for the 10 min etched sample and which suggest that stronger localization due to the increased disorder introduced due to plasma etching for longer times. The step-like increase in sheet resistance at T_o is similar to the signature observed in electrical transport for charge density wave transitions. In this case of charge density wave increase in R_s results from a partial loss of density of states due to the opening a gap at the Fermi surface [100].

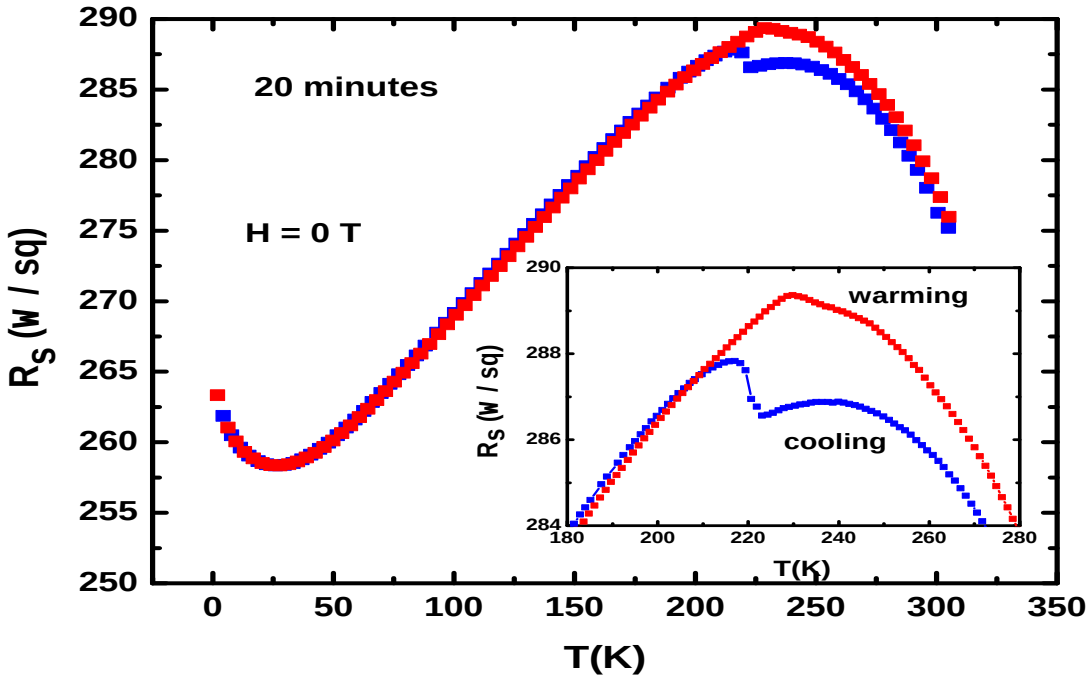

FIGURE 5.7: The electrical transport as sheet resistance R_s versus temperature T for 20 minutes plasma etched of the Na_2IrO_3 crystals at zero magnetic field while cooling from T = 305 K and warming from T = 2 K. The inset shows the cooling and warming data to highlight the thermal hysteresis which indicating the first-order nature of the phase transition.

The transition temperature at T_0 is first order as shown by the thermal hysteresis of $\approx$ 10 K between cooling and warming data shown in the Figure 5.7. This behaviour in transition at T_0 is robust in an applied magnetic field of up to $H = 9$ T as can be seen in the Figure 5.8. An additional feature which is not observed in conventional charge density wave systems is the magnetic field dependence. Figure 5.8 shows the sheet resistance data measured while cooling in various magnetic fields H. Above the transition temperature T_o, there is no H dependence and all data points fall on top of the each other. However, at and below the transition temperature T_o there is an increase in the magnitude of $R_s(T)$ on the application of field although the qualitative behaviour

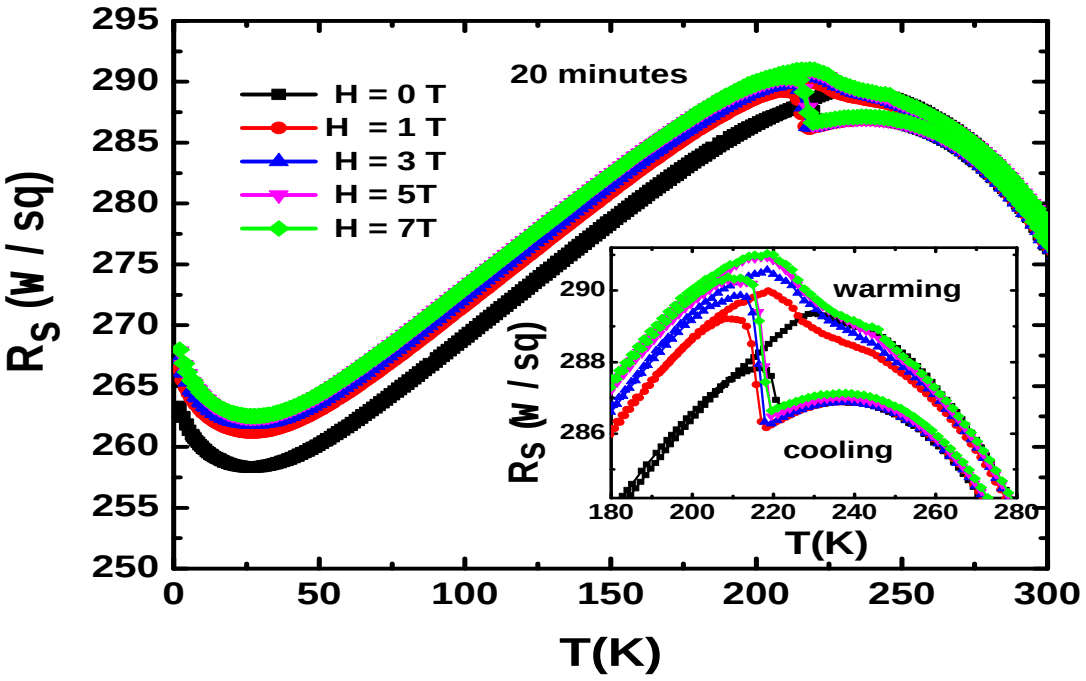

FIGURE 5.8: The electrical transport as sheet resistance R_s versus T for a 20-minute plasma-etched samples of Na_2IrO_3 crystals measured in different applied magnetic field H while cooling from T = 305 K and warming from T = 2 K. The inset shows the cooling and warming data of different applied magnetic field H to highlight the thermal hysteresis which indicating the first-order nature of the phase transition.

remains the same. The magnitude of the step-like increase in $R_s(T_o)$ also increases in applied magnetic fields as seen in the Figure 5.8 inset.

5.3.3 Electrical transport of 30 minute etched samples

Figure 5.9 (a) and Figure 5.10 show the sheet resistance $R_s(T)$ versus temperature T data, measured while cooling, for two crystals exposed for 30 minutes. While the details of the data are different, the qualitative behaviour for these two samples is the same. On cooling, one finds an increase in $R_s(T)$, a maximum around 250–275 K, after which it continuously decreases down to $T_0 = 95$ K where an abrupt step-like decrease in $R_s(T)$ by more than an order of magnitude occurs suggesting a density wave-like transition. There is again a thermal hysteresis between cooling and warming measurement indicating the first order nature of the transition about 10 K shown in Figure 5.9 (a) inset I. At low temperature $R_s(T)$ data follow a T^2 behaviour indicating Fermi liquid behaviour. The T^2 dependence fit through the data is shown in the Figure 5.9 (a) inset II and Figure 5.10 inset.

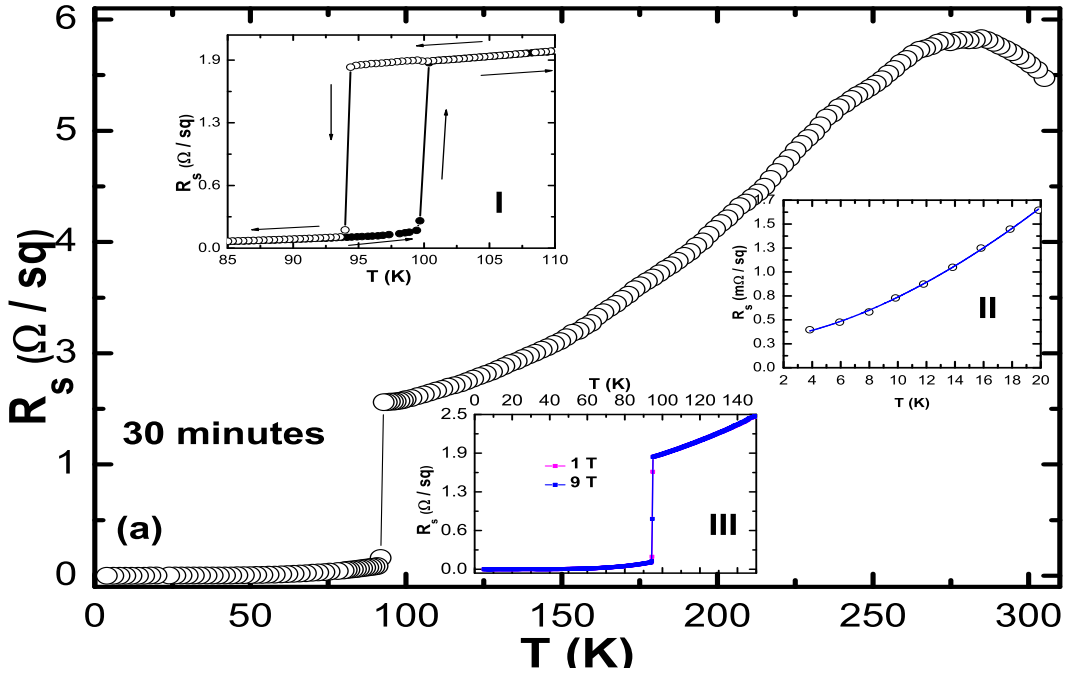

FIGURE 5.9: Sheet resistance R_s versus temperature T for two Na_2IrO_3 crystals after 30 minutes of Ar plasma etching. (a) R_s vs T of one crystal measured in zero magnetic field while cooling from $T = 305$ K. Inset I shows the cooling and warming data to highlight the thermal hysteresis indicating the first-order nature of the transition. Inset II shows the low temperature data below $T = 20$ K. The curve through the data is a fit to a T^2 dependence suggesting Fermi liquid behaviour. Inset III shows the $R_s(T)$ data measured in two magnetic fields to highlight the absence of any H dependence.

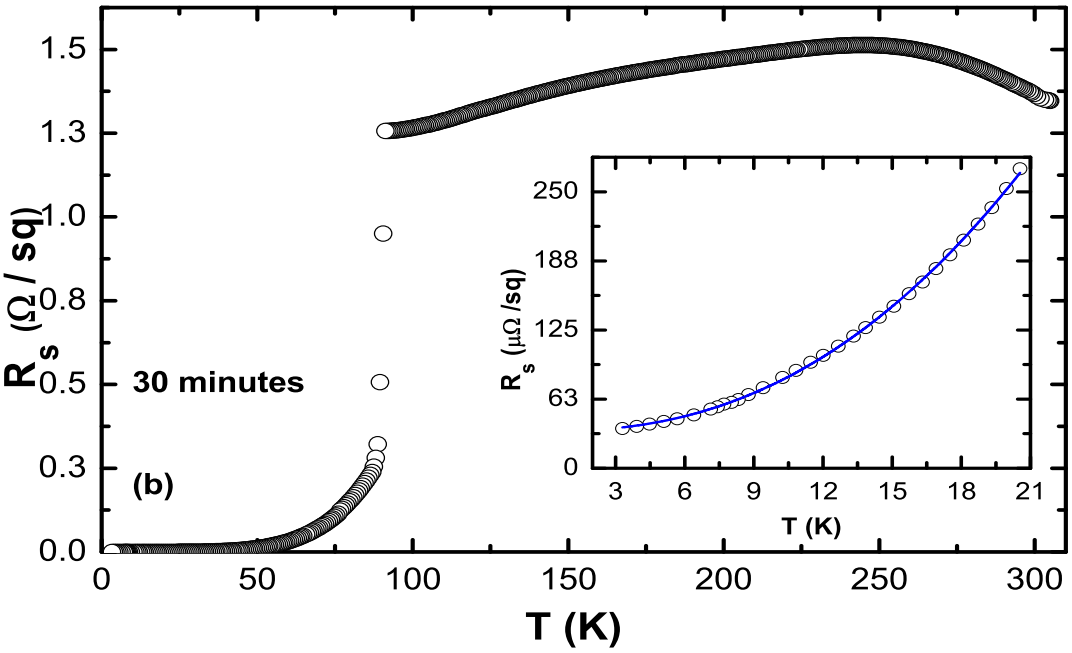

FIGURE 5.10: R_s vs T of the second crystal measured in zero magnetic field while cooling from $T = 305$ K. Inset shows the low temperature data below $T = 20$ K. The curve through the data is a fit to a T^2 dependence suggesting Fermi liquid behaviour.

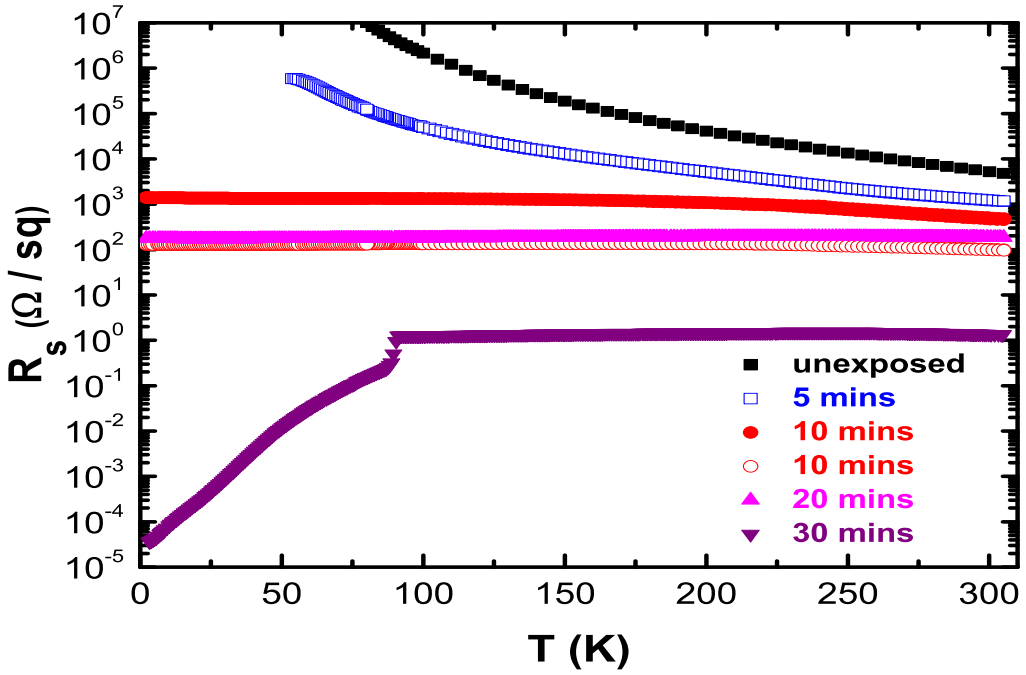

FIGURE 5.11: A semi-log plot of the sheet resistance R_s versus temperature T for Na_2IrO_3 after varying periods of etching using an Ar plasma.

If we consider complete crystal thickness ($\approx$ 0.1 mm) and use it in calculating the geometrical factor for converting sheet resistance into resistivity ρ then the coefficient of the T^2 dependence is estimated to be $A = 27$ $\mu\Omega$ cm/K^2. This value is comparable to values obtained for Ce-based heavy Fermion compounds [101]. There is no magnetic field dependence of the sheet resistance for the 30 minute sample like for the 20 minute sample as seen in Figure 5.9 (a) inset III which shows the $R_s(T)$ data between 2 K and 150 K in a applied magnetic field of 1 T and 9 T.

The sheet resistance R_s versus temperature T for all samples for $t = 0, 5, 10, 20, 30$ minutes are shown on a semi-log scale in Figure 5.11 to highlight the change in R_s by several orders of magnitude with increasing etching times. Transport for the sample etched for 40 minutes could not be measured as the sample surface degraded within an hour before contacts could be made.

5.3.4 Magnetic susceptibility of etched and unetched sample

We measured magnetic susceptibility χ versus temperature T for unetched (parent) Na_2IrO_3 crystals and 20 min plasma etched of Na_2IrO_3 crystals shown in the given Figure 5.12. The magnetic susceptibility of unetched samples show sharp drop below T_N =

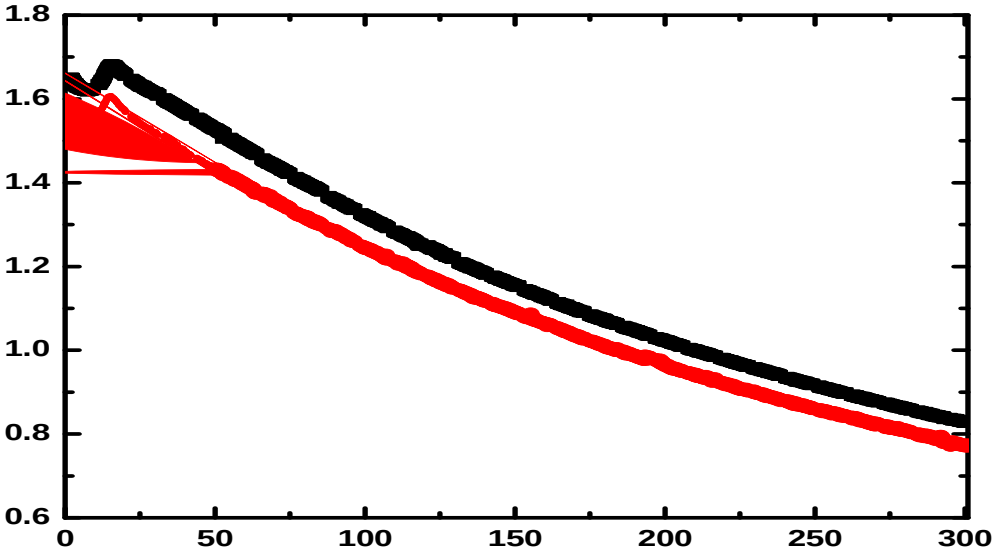

FIGURE 5.12: The magnetic susceptibility χ versus temperature T of unetched Na_2IrO_3 crystals and 20 minute etched crystals between T = 2 and 305 K.

15 K indicate long-ranged antiferromagnetic ordering in Na_2IrO_3 [1]. This long range ordering is present at a slightly lower temperature in 20 min plasma etched samples. The magnetic measurements suggest that there is no significant change in the bulk characteristics of the Na_2IrO_3 crystals when etched using a plasma. The $1/\chi$ data between T = 150 K and 300 K were fitted by the Curie-Weiss fit using expression $\chi = \chi_0 + \frac{C}{T-\theta}$ shown in the Figure 5.13.

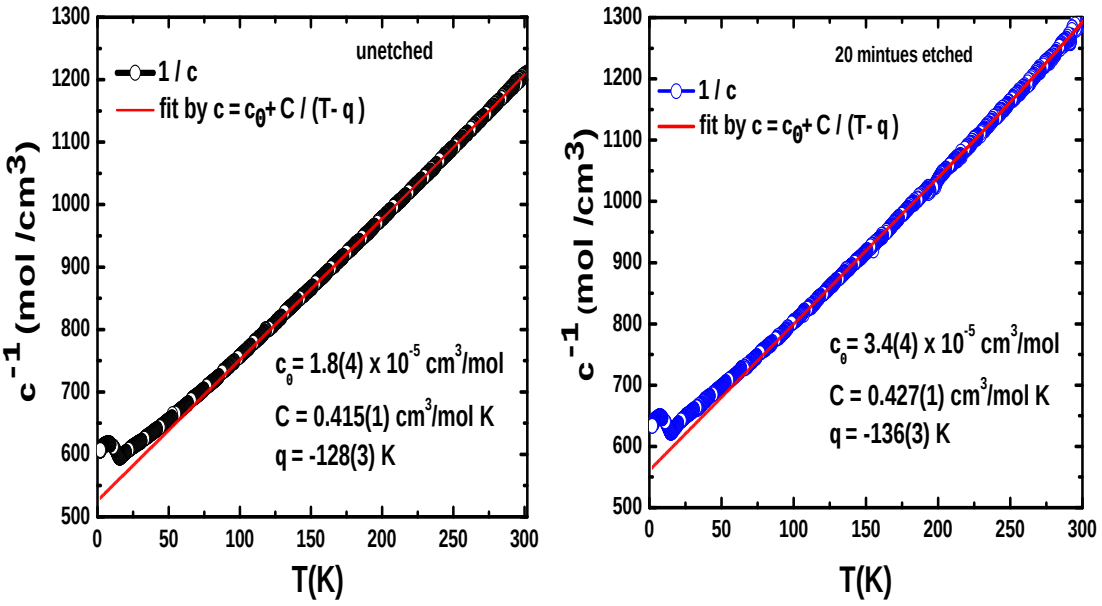

FIGURE 5.13: Curie-Weiss fitting of unetched crystals of Na_2IrO_3 and 20 minute etched crystals.

5.4 Summary and Discussion

We have successfully shown that surface of Na_2IrO_3 crystals are highly tunable using plasma etching. Ar plasma etching can be used to effectively dope the surface of Na_2IrO_3 crystals and change in their electrical conductivity by several order of magnitude by varying the plasma exposure time. The surface structure of Na_2IrO_3 did not change by plasma etching as revealed by grazing incidence small angle x-ray scattering (GISAXS) and EDS chemical analysis revealed that Na was being progressively removed on increasing the etching time. The electrical transport signatures consistent with those observed for density wave or structural transitions. Specifically, temperature dependent sheet resistance R_s(T) for 20 and 30 minutes etched samples show charge density wave like phase transitions with an abrupt change in R_s at T_0 = 220 and 95 K, respectively as shown in the Figure 5.8 and Figure 5.9.

Such transport anomalies have been observed previously for charge density wave transitions in many other compounds [102–104]. The phase transition is first order as revealed by a 10 K thermal hysteresis between cooling and warming measurements. The 30 minutes etched sample follows a T^2 Fermi liquid behavior at low temperature. Remarkably such spin/charge density waves, electronic dimerization instabilities, and bond order instabilities have been predicted on doping for antiferromagnetic Kitaev and ferromagnetic Heisenberg interaction[10, 95, 97].

However, surface sensitive probes like scanning tunneling microscopy (STM) or electron diffraction will be required to confirm the coupled electron density and structural modulations expected below a CDW transition [100]. The samples etched for 10 minutes revealed unusual transport behavior with an increase in sheet resistance R_s on cooling from 300 K down to 150–200 K below which $R_s(T)$ became almost T-independent (see Fig. 5.6). This behavior is consistent with that expected for topological insulators where at low temperatures surface conductivity starts contributing after the bulk becomes sufficiently insulating. It must be noted that topological insulating state has been predicted for Na_2IrO_3 under certain conditions [33, 94]. Whether this behaviour in doped Na_2IrO_3 has any topological properties will have to be explored in more detailed surface sensitive studies in future.

Chapter 6

First-order magnetostructural transition in single crystalline honeycomb lattice ruthenate Li_2RuO_3

6.1 Introduction

Like the iridates A_2IrO_3, the ruthenate family A_2RuO_3 (A = Na,Li) is also known to adopt a honeycomb lattice structure but with nominal S = 1 moments arising from the low-spin state of Ru^{4+}. Polycrystalline Li_2RuO_3 has been reported to show an unusual phase transition below $T_d \approx 540$ K from a nearly perfect honeycomb lattice C2/m structure at high temperature to a low temperature $P2_1/m$ structure with a distorted honeycomb lattice [12]. Below T_d one of the three inequivalent Ru-Ru bonds in the honeycomb hexagon becomes significantly shorter than the other two [54]. This structural dimerization is also accompanied by Ru-Ru spin singlet formation leading to a strong decrease of the magnetization at T_d [12, 54]. These experimental observations have motivated several theoretical studies to understand the nature of the transition and the role of electronic correlations. Based on DFT calculations it was proposed that Li_2RuO_3 undergoes a transition from a highly correlated metal to a molecular orbital insulator involving Ru-Ru dimerization and spin-singlet formation [12, 54]. An

alternative mechanism of spin-singlet formation driven by magnetoelastic coupling has also been proposed [8]. An electronic structure study has highlighted the importance of electronic correlations and proposed that a combination of local-moment behavior and molecular orbital formation could be the correct picture for this material [66].

Broad transitions and sample dependent magnetic properties of polycrystalline samples have plagued efforts to understand these materials fully and ideally high quality single crystals are required. Single crystals of Li_2RuO_3 were indeed recently synthesized. However, these have added to the prevailing confusion. The crystals were found to crystallize at room temperature in either the C2/m or the $P2_1/m$ structures depending on synthesis conditions. However, in complete contrast to all existing polycrystalline work [12, 56–58] neither of these crystals show the coupled magneto-structural transitions at high temperature. They instead show Curie-Weiss behavior below 300 K and magnetic ordering at low temperatures into supposedly antiferromagnetic states [53].

We wanted to understand conflicting reports on the magnetic behaviors of the honeycomb lattice ruthenate Li_2RuO_3 and whether the unusual magneto-structural transition could only be observed in polycrystalline samples suggesting it was somehow linked to the poor quality of samples. In this chapter we report the first growth of single crystals of Li_2RuO_3 which crystallize at room temperature in $P2_1/m$ structure and show the expected high temperature magneto-structural transition. We are thus able to investigate for the first time the anisotropic properties of Li_2RuO_3 across this high temperature coupled transition. Our magnetic measurements between 2 and 1000 K reveal that the transition is first-order in nature and most likely occurs in two steps with the structural transition occurring first at a higher $T_d \simeq 570$ K and then drives the magnetic transition around $T_m \simeq 540$ K. χ above T_d is consistent with quasi-2-dimensional magnetism.

6.2 Experimental Details

The single crystalline samples of $(Li_{1-x}Na_x)_2RuO_3$ ($x = 0, 0.05$) have been synthesized. The starting materials were Li_2CO_3 (99.995% Alfa Aesar), Na_2CO_3 (99.995% Alfa Aesar) and Ru metal powder (99.95% Alfa Aesar). Single crystals were grown using a self flux growth method. Off-stoichiometric amounts of starting materials were mixed thoroughly in the ratio 1 : 1.2 and placed in an alumina crucible with a lid, heated to 750 °C

in 10 h and kept for 24 h for calcination and then furnace cooled to room temperature. The resulting powder was ground in an agate motor pestle for about an hour and press into a pellet and given a further heat treatment at 950 °C for 48 h. Crystal growth was done by keeping the resulting powder for long periods (70–80 h) at temperatures between 1050 °C – 1080 °C, and cooling to 900 °C at 5 °C/hr after which the furnace is turned off and allowed to cool to room temperature. Shiny plate like single crystals (size $\sim 0.5 \times 0.5 \times 0.03\ mm^3$) were found to grow on top of semi-melted polycrystalline powder. Growth of single crystals with higher Na concentrations ($x = 0.1, 0.2, 0.3$) were tried but were not successful. The structure and composition of the resulting samples were checked by single-crystal and powder x-ray diffraction (PXRD), and chemical analysis using energy dispersive x-ray (EDX) analysis with a JEOL scanning electron microscope (SEM). The PXRD was obtained by a Rigaku diffractometer with Cu K_α radiation in 2θ range from 10° to 90° with 0.02° step size. Anisotropic magnetic susceptibility measurements upto $T = 1000$ K were measured on a collection of crystals with total mass ≈ 15 mg using the vibrating sample magnetometer(VSM) Oven option on a Quantum Design Physical Property Measurement System.

6.3 Crystal Structure and Chemical Analysis

We collected single crystal and powder x-ray diffraction (PXRD) data at room temperature (300 K). From the room temperature data, we conclude that all samples adopt the $P2_1/m$ space group. A full single crystal refinement was not possible because the crystals have multiple twins rotated around the c^* axis. However, it was possible to determine the space group and cell parameters using single crystal diffraction. These were used as starting points while performing Rietveld refinements of the PXRD patterns obtained on the crushed crystals. Figure 6.1 shows results of Rietveld refinement of the PXRD patterns for $(Li_{1-x}Na_x)_2RuO_3$ ($x = 0, 0.05$). The fractional atomic positions obtained from the refinement are given in Table 6.1. The unit cell parameters and the relevant bond lengths extracted from Rietveld refinement of the powder diffraction data are listed in Table 6.2. The cell parameters change significantly (specially the a-axis) as Li is partially replaced by Na. The presence of Na in the doped crystals and its concentration relative to Ru was confirmed using energy dispersive X-ray spectroscopy

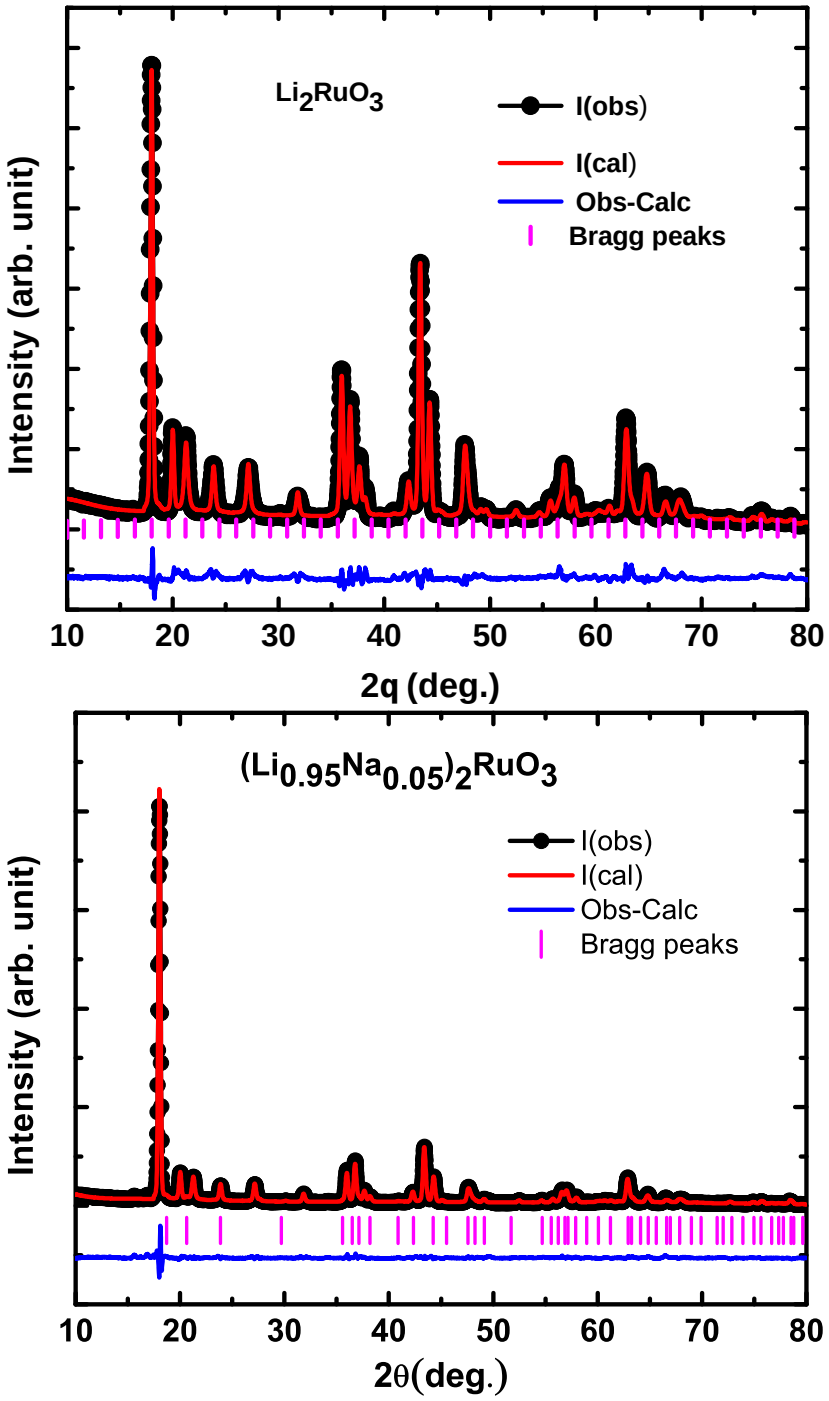

FIGURE 6.1: Rietveld refinements of powder x-ray diffraction data for $(Li_{1-x}Na_x)_2RuO_3$ ($x = 0, 0.05$). The solid circles represent the observed data, the solid lines through the data represent the fitted pattern, the vertical bars represent the peak positions, and the solid curve below the vertical bars is the difference between the observed and the fitted patterns.

on several spots on the same crystal and on several crystals and was found to be close to the nominal concentration targeted in the starting material.

The room temperature crystal structure of Li_2RuO_3 and Li viewed perpendicular to the

honeycomb planes is shown in Figure 6.2 to highlight the Ru-Ru dimerization pattern. For Li_2RuO_3 we found, consistent with previous work, that one (d_2) out of the three inequivalent Ru-Ru bonds is considerably shorter compared to the other two which are of similar lengths. Surprisingly, for just 5% Na substitution for Li, the dimerization pattern changes and we now have two short (d_2 and d_3) and one long bonds. The Ru-Ru bond lengths are given in Table 6.2 and the dimerization patterns shown in Figurs 6.2 (a) and (b), respectively. For Li_2RuO_3 as observed [12] and explained [8] previously the dimers on the d_2 bond form an armchair pattern. For the Na substituted sample, both d_2 and d_3 bonds dimerize and form inter-penetrating armchairs which run along the a-axis.

TABLE 6.1: Wyckoff position for $(Li_{1-x}Na_x)_2RuO_3$ ($x = 0, 0.05$) obtained from Rietveld refinements of polycrystal x-ray data at 300 K

.

Li_2RuO_3						
Atom	*Wyckoff*	*x*	*y*	*z*	*Occ*	*B* (Å)
Ru	4f	0.2665(7)	0.0762(7)	-0.0048(5)	1	0.0783
Li1	2e	0.6885(7)	0.25	-0.0237(8)	1	0.0229
Li2	4f	0.3806(3)	0.0807	0.5253(8)	1	0.00229
Li3	2e	0.7566(8)	0.25	0.6355(5)	1	0.0306
O1	4f	0.7875(6)	0.08556(7)	0.2976(8)	1	0.0043
O2	4f	0.7894(4)	0.0704(8)	0.8026(2)	1	0.1098
O3	2e	0.2529(7)	0.25	0.2114(6)	1	0.0046
O4	2e	0.2494(8)	0.25	0.7806(8)	1	0.0487
$(Li_{0.095}Na_{0.05})_2RuO_3$						
Atom	*Wyckoff*	*x*	*y*	*z*	*Occ*	*B* (Å)
Ru	4f	0.2467(7)	0.0776(8)	-0.0038(7)	1	0.0265
Li1	2e	0.7857(5)	0.25	-0.0295(8)	0.95	0.0800
Na1	2e	0.7857(5)	0.25	-0.0295(8)	0.05	0.0900
Li2	4f	0.0661(3)	0.25	0.6213(7)	1	0.0034
Li3	2e	0.6887(3)	0.0523(5)	0.4685(6)	1	0.0020
O1	4f	0.7812(6)	0.0644(7)	0.2831(8)	1	0.0043
O2	4f	0.7502(5)	0.0957(7)	0.7931(2)	1	0.0060
O3	2e	0.3124(7)	0.25	0.2688(5)	1	0.0088
O4	2e	0.2396(8)	0.25	0.2373(4)	1	0.0080

TABLE 6.2: Summary of Lattice Parameters and relevant bond lengths of $(Li_{1-x}Na_x)_2RuO_3$ $(x \approx 0, 0.05)$

Sample	Li_2RuO_3	$(Li_{0.95}Na_{0.05})_2RuO_3$
Space Group	$P2_1$ /m	$P2_1$ /m
a $(\AA)$	4.920(4)	4.934(5)
b $(\AA)$	8.781(7)	8.774(4)
c $(\AA)$	5.893(3)	5.895(6)
β (deg)	124.36(4)	124.42(6)
V $(\AA)$	210.452(5)	210.452(5)
$Ru-Ru$ $(\AA)$		
d_1	3.048	3.025
d_2	2.635	2.812
d_3	2.976	2.823

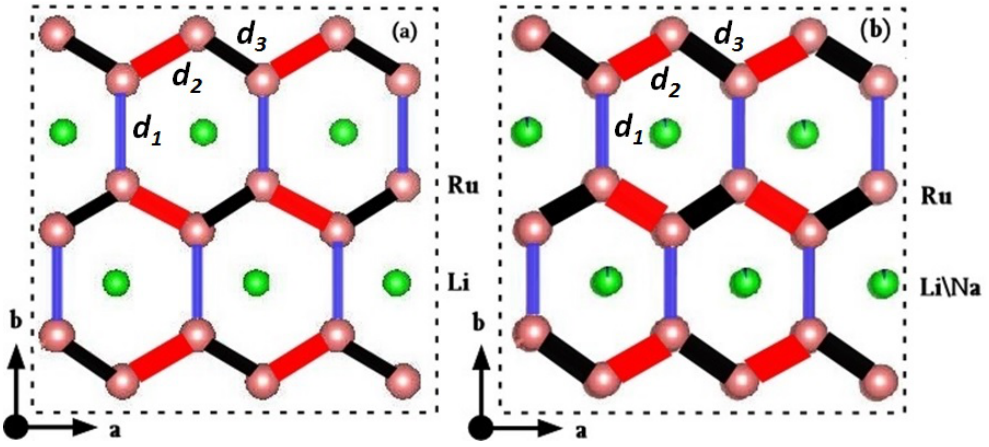

FIGURE 6.2: Room temperature structure of (a) Li_2RuO_3 and (b) $(Li_{0.95}Na_{0.05})_2RuO_3$ viewed perpendicular to the Ru honeycomb network in the *ab*-plane. There are three inequivalent Ru-Ru bonds in the honeycomb network labeled as d_1 (blue), d_2 (red), and d_3 (black). For Li_2RuO_3, the Ru-Ru dimerization happens on the d_2 bonds (shown as the thicker red bonds in (a)) which are considerably shorter than d_1 and d_3 which are of similar length. The armchair pattern observed for Li_2RuO_3 is consistent with that observed earlier [12]. For $(Li_{0.95}Na_{0.05})_2RuO_3$ the dimerization pattern changes and there are two short bonds d_2 (thick red) and d_3 (thick black) and one long bond d_1 (thin blue). The dimer arrangement can be viewed as two inter-penetrating armchair patterns.

6.4 Magnetic Properties

6.4.1 Li_2RuO_3

The magnetic susceptibility χ versus T data for Li_2RuO_3 measured in an applied magnetic field $H = 5$ T applied parallel to the honeycomb plane $(\chi_{||})$ and perpendicular to the honeycomb plane $(\chi_{\perp})$ are shown in Figure 6.3. The χ is anisotropic with $\chi_{||} > \chi_{\perp}$

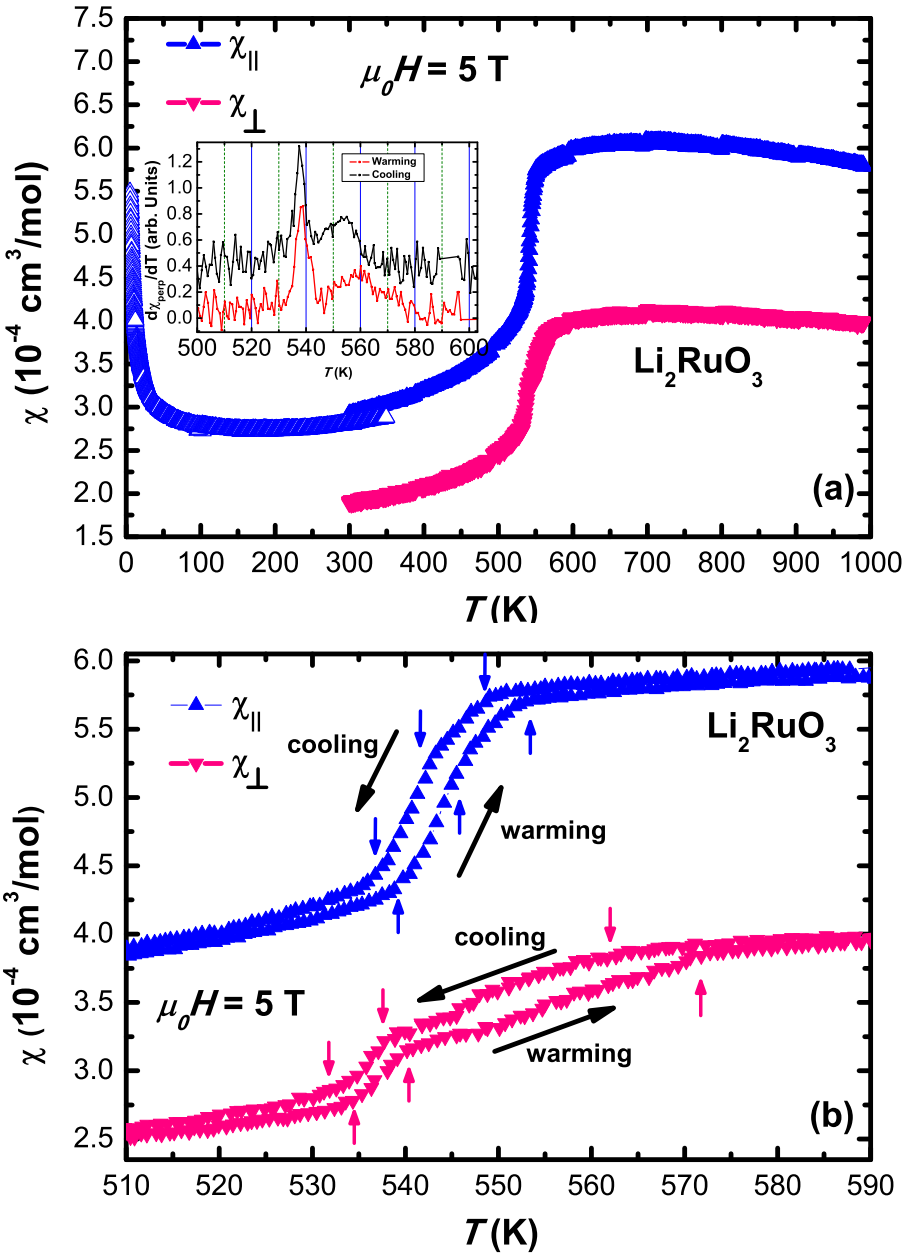

FIGURE 6.3: (a) Magnetic susceptibility $\chi_{||}$ and $\chi_{\perp}$ versus T measured in a magnetic field of 5 T for Li_2RuO_3 between $T = 2$ and 1000 K. (b) $\chi_{||}$ and $\chi_{\perp}$ versus T in the temperature range 510 to 590 K to highlight the behaviour near the transition. The arrows indicate the onset of the magnetic or structural transition in data recorded while warming or cooling. The inset in (a) shows the $d\chi_{\perp}/dT$ versus T data.

for all temperatures. Figure 6.3(a) shows the $\chi_{\perp}$ data from 300 K to 1000 K and the $\chi_{||}$ data from 2 K to 1000 K. The magnetic susceptibility data were measured during cooling down from 1000 K to 2 K and during warming from 2 K to 1000 K for both $\chi_{||}$ and $\chi_{\perp}$. The $\chi(T)$ behavior at high temperatures is not Curie-Weiss like as expected for a paramagnet. Instead the $\chi(T)$ behavior is consistent with a quasi-two-dimensional

TABLE 6.3: Temperatures of the peaks in $d\chi/dT$ for $\chi_{||}$ and $\chi_{\perp}$ of single crystalline Li_2RuO_3 at $H = 5$ T

	Magnetic susceptibilities	T_1	T_2
Li_2RuO_3			
	$\chi_{||}$ (heating)	543 K	548 K
	$\chi_{||}$ (cooling)	539 K	544 K
	$\chi_{\perp}$ (heating)	538.3 K	561 K
	$\chi_{\perp}$ (cooling)	537.8 K	555 K
$(Li_{0.095}Na_{0.05})_2RuO_3$			
	$\chi_{||}$ (heating)	542 K	
	$\chi_{||}$ (cooling)	535 K	
	$\chi_{\perp}$ (heating)	538 K	
	$\chi_{\perp}$ (cooling)	531 K	

magnetic system having stronger in-plane interactions. We also see evidence for a transition involving an abrupt drop in χ below about 550 K. This is a signature of the magneto-structural transition observed previously for polycrystalline samples [12]. The magneto-structural transition has been previously reported to involve a structural change below 540 K from $C2/m$ to $P2_1/m$ symmetry and a simultaneous Ru-Ru dimerizations with spin-singlet formation [12]. The abrupt drop in χ at the transition is consistent with Ru-Ru spin-singlet formation. The magnitude of the drop can be quantified by $\chi_{\rm min}/\chi_{\rm max}$ and is ≈ 0.45 for both $\chi_{||}$ and $\chi_{\perp}$. The magnitude of the drop in χ across the magneto-structural transition is similar to values found previously for polycrystalline samples [12, 56, 57]. Below 300 K, the $\chi(T)$ is T independent and small but finite. This T independent finite value ($\chi_{||} \approx 2.75 \times 10^{-4}$ cm^3/mol) is most likely a Van Vleck paramagnetic contribution [105]. At low temperatures there is an upturn in $\chi(T)$ which is most likely due to the presence of a small amount of paramagnetic impurities.

In Figure 6.3 (b) we show the $\chi_{\perp}$ and $\chi_{||}$ data on an expanded scale around the region of the phase transition. The $\chi(T)$ data were recorded while warming from 300 K to 1000 K and then while cooling back again at a rate of 5 K/min. We found that there is a thermal hysteresis between the warming and cooling data indicating the first order nature of the phase transition. The various transition temperatures are identified with peaks in the derivatives of the $\chi(T)$ data and are listed in Table 6.3. From the $\chi_{||}$ and $\chi_{\perp}$ data we get a two step transition as indicated by vertical arrows for cooling and warming measurements in the Figure 6.3 (b). A derivative of the $\chi_{\perp}$ data shown in the inset of Fig. 6.2 reveals two peaks which are taken as the approximate transition

temperatures and listed in Table 6.3. We note that the lower transition temperature in $\chi_\perp$ occurs at $T \approx 538$ K, is very sharp and is not accompanied by any significant thermal hysteresis. The higher temperature transition has an onset as high as $T > 570$ K and a mid-point around $T \approx 561$ K as seen by the peak in $d\chi_\perp/dT$ measured while warming up to 1000 K. This high temperature transition is broad and clearly hysteretic with a thermal hysteresis of 6 K indicating its first-order nature. These observations suggest that the higher temperature hysteretic transition is the structural dimerization transition while the lower temperature transition where we observe a sharp drop in χ is the magnetic transition involving Ru-Ru singlet formation. Thus for Li_2RuO_3 samples the two transitions (structural and magnetic) most likely occur at slightly different temperatures with the structural dimerization transition occurring first and triggering the magnetic Ru-Ru singlet formation.

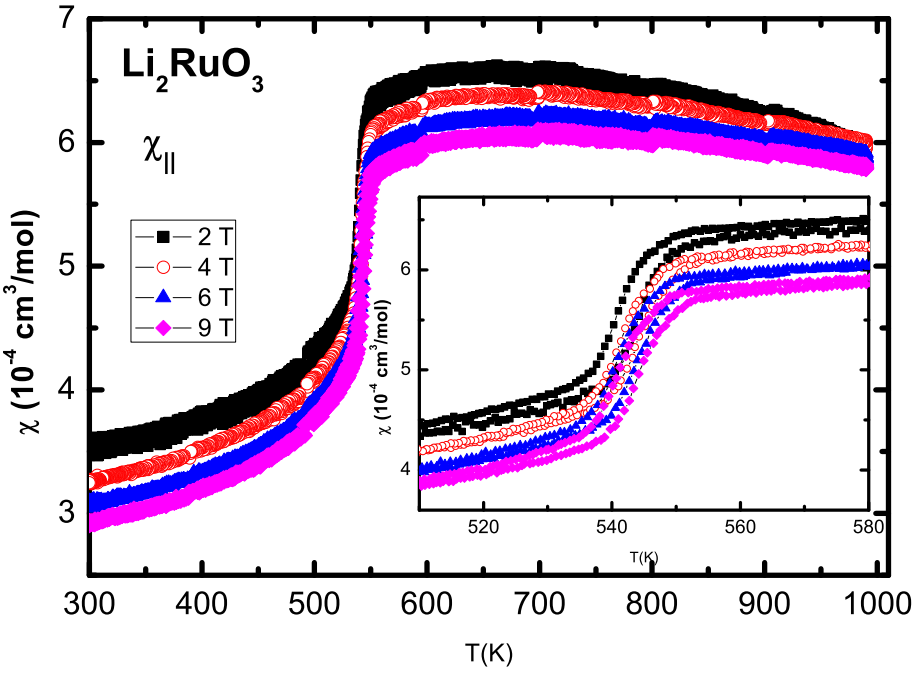

FIGURE 6.4: Magnetic susceptibility $\chi_{||}$ versus T measured at different applied field magnetic field of (H = 2 T, 4 T, 6 T, 9 T) for Li_2RuO_3 between $T = 300$ K and 1000 K. Tiny jumps seen in the data at 100 K temperature interval are due to auto centering of the sample.

We have also explored whether magnetic field has any effect on these transitions. The magnetic susceptibility $\chi_{||}(T)$ data at different applied fields ($H = 2$ T, 4 T, 6 T, 9 T) are shown in the given Figure 6.4. In the Figure, the χ at each increasing field has been shifted down by 0.5×10^{-4} cm^3/mol for clarity. The inset shows the data near the transition to show that there is no effect of the field on the transition temperature or

width. The jumps in the $\chi_{||}$ versus T data at some intervals of temperature are due to auto-centering not because of sample transition.

6.4.2 $(Li_{0.95}Na_{0.05})_2RuO_3$

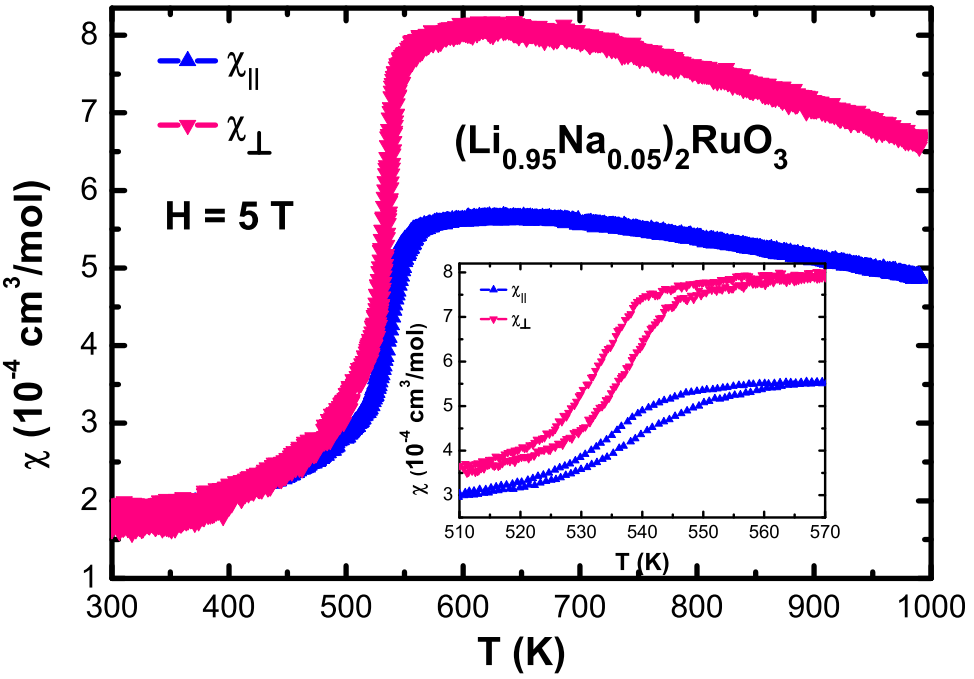

FIGURE 6.5: (Color online) Anisotropic Magnetic susceptibility $\chi_{||}$ and $\chi_{\perp}$ versus T measured at in a magnetic field of 5 T for $(Li_{0.95}Na_{0.05})_2RuO_3$ between $T = 300$ K and 1000 K. The inset shows the $\chi_{||}$ and $\chi_{\perp}$ versus T in the temperature range 510 K to 570 K to highlight the behaviour near the transition.

The magnetic susceptibility χ versus T data for $(Li_{0.95}Na_{0.05})_2RuO_3$ measured between 300 K to 1000 K in an applied magnetic field $H = 5$ T applied parallel to the honeycomb plane ($\chi_{||}$) or perpendicular to the honeycomb plane ($\chi_{\perp}$) are shown in Figure 6.5. Surprisingly we found that for only 5% Na substitution at Li site, the magnetic anisotropy is reversed ($\chi_{\perp} > \chi_{||}$) compared to what we observed for Li_2RuO_3 samples. The magneto-structural transition can be seen in data for both field directions. The Figure 6.5 inset shows the $\chi_{||}$ and $\chi_{\perp}$ data in the temperature range 510 K to 570 K to highlight the transition. Data were recorded while warming from 300 K to 1000 K and then while cooling back again at a rate of 5 K/min. We found that there is a thermal hysteresis between the warming and cooling data indicating that the first order nature of the phase transition persists in Na substituted samples. Peaks in the derivatives of the $\chi(T)$ data (not shown) are taken as the approximate transition temperatures and are given

in Table 6.3. The transition for the Na substituted crystals seems to be a single coupled magneto-structural transition. This could arise from the disorder introduced due to doping which probably smears out the two-step transition and merges them together.

6.5 Summary and Discussion

We have grown the first single crystals of $(Li_{1-x}Na_x)_2RuO_3$ ($x = 0, 0.05$) with monoclinic crystal symmetry $P2_1/m$ structure at room temperature and showing a magneto-structural transition at high temperatures. Using magnetic susceptibility χ measurements for temperatures $T \leq 1000$ K we observed that for Li_2RuO_3, $\chi_{||} > \chi_{\perp}$. Furthermore, we observe a first-order high temperature coupled magneto-structural transition which seems to occur in two steps for Li_2RuO_3 samples . This signature is most prominent in the $\chi_{\perp}$ data. The higher temperature phase transition occurs around $T \approx 570$ K with a thermal hysteresis of 6 K indicating its first-order nature while the low temperature transition has negligible hysteresis and involves a sharp drop in the magnitude of χ. These observations suggest that the higher temperature, hysteretic transition is the structural dimerization transition while the lower temperature transition is the magnetic transition involving Ru-Ru singlet formation. The onset temperature of 570 K is much higher than previously observed (≈ 540 K) and indicates the high quality of the Li_2RuO_3 crystals.

Just 5% substitution of Na for Li leads to interesting magnetic and structural changes. The high temperature $\chi(T)$ data show that the magnetic anisotropy is reversed compared to Li_2RuO_3 with $\chi_{\perp} > \chi_{||}$ for $(Li_{0.95}Na_{0.05})_2RuO_3$. The switching of the magnetic anisotropy of Na substituted sample is interesting. We do not have an understanding of the magnetic anisotropy and why it switches for the doped samples. The cause of anisotropy in solids can have various origins, mostly related to the local structure and co-ordination around the magnetic ion. However, it is complicated to predict anisotropy. For example, the magnetic anisotropy for Na_2IrO_3 and Li_2IrO_3 are opposite even though the global structure and oxygen octahedra around Ir are similar.

The magneto-structural transition for the Na substituted crystals also seems to happen in a single step. The arrangement of Ru-Ru dimers on the honeycomb lattice also changes for the Na substituted crystals. For Li_2RuO_3 Rietveld refinements of room temperature

powder X-ray data reveal that one (d_2) out of the three inequivalent Ru-Ru bonds on the honeycomb lattice is shortened compared to the other two which are almost equal to each other as can be seen in Table 6.2. For $(Li_{0.95}Na_{0.05})_2RuO_3$ we find that two (d_2 and d_3) out of the three Ru-Ru bonds are smaller and almost equal while the third is much larger. The armchair arrangement of the dimers in Li_2RuO_3 is consistent with previous reports [8, 12]. The dimer arrangement in $(Li_{0.95}Na_{0.05})_2RuO_3$ can be viewed as two inter-penetrating armchairs formed on the d_2 and d_3 bonds, respectively. This suggests a possible change in the orbital ordering pattern for the Na substituted sample.

Chapter 7

Crystal growth, structure, and magnetic properties of a new honeycomb lattice iridate K_2IrO_3

7.1 Introduction

The iridium-based honeycomb lattice materials A_2IrO_3 (A= Na, Li) have thus far been the most promising candidates for the realization of Kitaev physics [4]. The importance of Kitaev interactions in driving the unusual magnetism in these materials is well accepted now. For Na_2IrO_3 there is recent direct evidence of bond-dependent Kitaev-like interactions [13] and the unusual magnetic structure found in Li_2IrO_3 has been shown to be a result of competing Kitaev and Heisenberg terms [106]. Despite these exciting results however, it is a fact that both materials are magnetically ordered at low temperatures [1, 34], suggesting that while Kitaev interactions could be present or even dominant, there are residual isotropic exchange terms which lead to magnetic order being stabilized instead of the quantum spin liquid state expected in the strong Kitaev limit [5].

The Kitaev and Kitaev-Heisenberg models are strictly 2-dimensional models [4, 5, 31], while it is clear that the real materials have magnetic interactions in all three directions which eventually leads to the three-dimensional magnetic order being stabilized. One strategy to push the A_2IrO_3 materials towards the dominant Kitaev limit and to enhance

quantum fluctuations and nudge the materials closer to the QSL state would be to try to make them more two-dimensional. This could be achieved by trying to increase the separation between the Ir honeycomb layers. Increasing the separation between the honeycomb layers will also lead to a reduction in the distortion of the IrO_6 octahedra discussed in Chapter 1 and will result in a structure closer to the ideal one required for Kitaev exchange [4, 5]. The A_2IrO_3 (A = Na, Li) structure is made up of layers which contain only the A atoms with alternating layers of AIr_2O_6 stacked along the c-axis [1]. If one could replace the A atoms in the spacer layers by a larger element like potassium K, then the AIr_2O_6 layers would be separated by a larger distance compared to samples with A = Na or Li.

To this end, we have attempted to discover and synthesize new, previously unknown materials in related structures and to study their magnetic properties in search of Kitaev's QSL states. We have succeeded in producing single crystals of a new iridate K_2IrO_3 and have studied their crystal structure and magnetic properties. Our structural studies confirm the target layered structure with a honeycomb network of edge-shared IrO_6 octahedra. Additionally, our magnetic studies demonstrate that K_2IrO_6 is a new QSL candidate.

7.2 Experimental Details

Single crystals of K_2IrO_3 were grown using metallic K pieces (99.995% Alfa Aesar) and Ir powder (99.99% Alfa Aesar), by a method similar to the one discovered recently to produce single crystals of α–Li_2IrO_3 [87]. The starting materials taken in the ratio 2 : 1 were kept separately in an alumina crucible, with Ir at the bottom of the crucible and K stuck to sharp edges of broken pieces of alumina crucibles. The crucibles with lids were heated in a box furnace to a final temperature between T = 700 and 800 K and kept there for about 75 hrs. Crystals are found to grow as hexagonal plates randomly stacked on the edge of the alumina spikes. A scanning electron microscope (SEM) image of some typical crystals is shown in Figure 7.1. The crystals are very small with the largest crystals being $\approx 100\ \mu m$ in their largest dimension.

The chemical composition of resulting crystal were checked using energy dispersive x-ray (EDX) analysis with a JEOL SEM. EDX data shows that the K : Ir ratio is close to

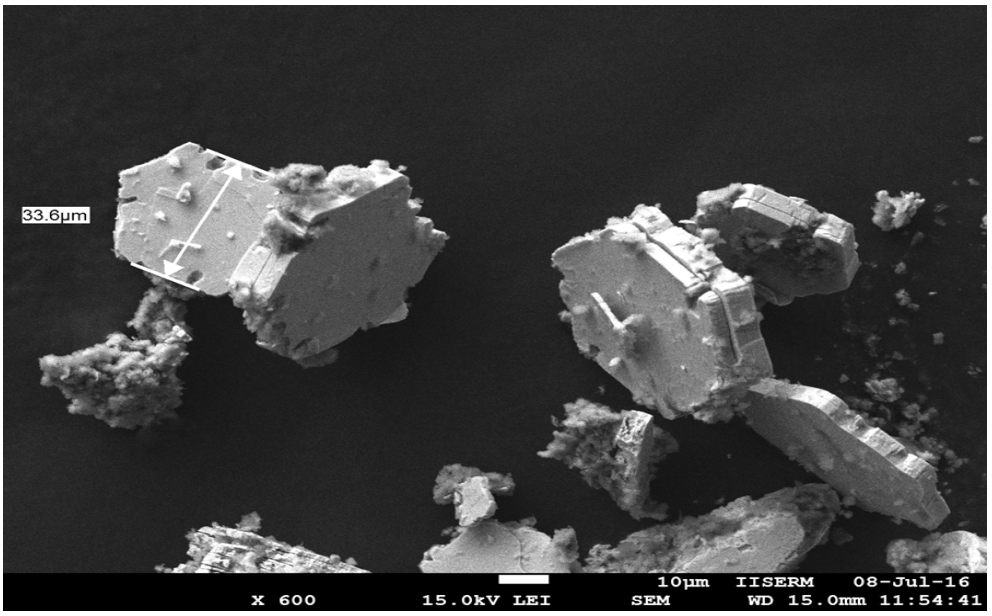

FIGURE 7.1: A scanning electron microscope image of as grown K_2IrO_3 single crystals. The hexagonal habit of the crystals and their layered nature is evident.

2 : 3. This value is different from the ratio 2 : 1 expected from the chemical formula. We note the structure if built up of K layers alternating with KIr_2O_6 layers. If the surface of the as grown crystal terminates on the KIr_2O_6 layers, then the ratio close to what we observe can be obtained.

The structural model below strongly points to K_2IrO_3 material. The structural analysis was performed in collaboration with the X-ray group at University of Oxford, England.

7.3 Crystal Structure

Over 30 single crystals have been studied by single crystal diffraction [107]. From a preliminary analysis it was found that most crystals adopt a hexagonal structure with two-layer stacking sequence of Ir honeycomb layers per unit cell and is consistent with the chemical formula K_2IrO_3. The structure shown in Figure 7.2 consists of a honeycomb lattice of edge-sharing IrO_6 octahedra nested around K sites in the *ab*-plane, stacked along *c*-axis and separated by hexagonal layers of K. The structure is therefore similar (but not same) to that of the previously studied iridates A_2IrO_3. One difference is that there are 2 Ir layers per unit cell for K_2IrO_3, while there were 3 such layers for A_2IrO_3. The separation between Ir layers in K_2IrO_3 is ≈ 7 $\AA$ whereas this distance for Na_2IrO_3 was ≈ 3 $\AA$. Thus, the Ir layer separation has been increased by more than a factor of

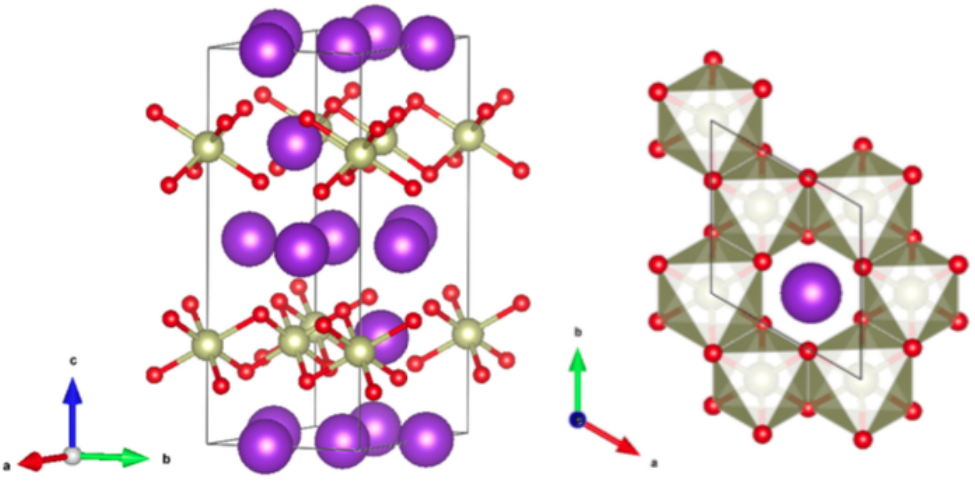

FIGURE 7.2: Left) 2–layer hexagonal crystal structure model for K_2IrO_3 with the unit cell indicated by black lines, Ir by green balls, K by purple and O by red. Right) The Ir layers consist of honeycombs formed by edge-sharing IrO_6 octahedra, with K in the honeycomb centres .

2. Thus we have succeeded in synthesizing a new material which matches our design goals of maintaining the edge shared IrO_6 octahedra and the honeycomb layer geometry while increasing the separation between these honeycomb layers. Thus we expect this new material to be closer to the Kitaev limit and to exhibit QSL behaviour.

7.4 Magnetic Susceptibility

The magnetic susceptibility χ versus temperature T data for K_2IrO_3 measured between $T = 1.8$ K and 395 K in an applied magnetic field $H = 2\ T$ are shown in Figure 7.3. The $\chi(T)$ behaviour is that of a local moment paramagnet with no signature of magnetic ordering down to $T = 1.8$ K.

The $1/\chi(T)$ data between $T = 100$ K and 380 K were fit by the Curie-Weiss expression $\chi(T) = \chi_0 + \frac{C}{T-\theta}$, where χ_0, C, and θ are fitting parameters. The fit, shown in Figure 7.4 as the solid and dashed curve (extrapolated upto T = 0 K) through the data, gave the values $\chi_0 = -2.23(4) \times 10^{-4}$ cm^3/mol, $C = 0.4$ cm^3 K/mol, and $\theta = -200(4)$ K, respectively. From the above value of C we estimate an effective moment $\mu_eff = 1.79(5)\ \mu_B$ which is close to the value ($1.73\ \mu_B$) expected for localized $S = 1/2$ moment with a g-factor $g = 2$. The value of $\chi_0 = -2.23(4) \times 10^{-4}$ cm^3/mol is the same order of magnitude as the total core diamagnetic susceptibility of the constituent ions. The core diamagnetic value for K_2IrO_3 system is $[(2 * -15 \times 10^{-6}) + (-29 \times 10^{-6}) + (3 *$

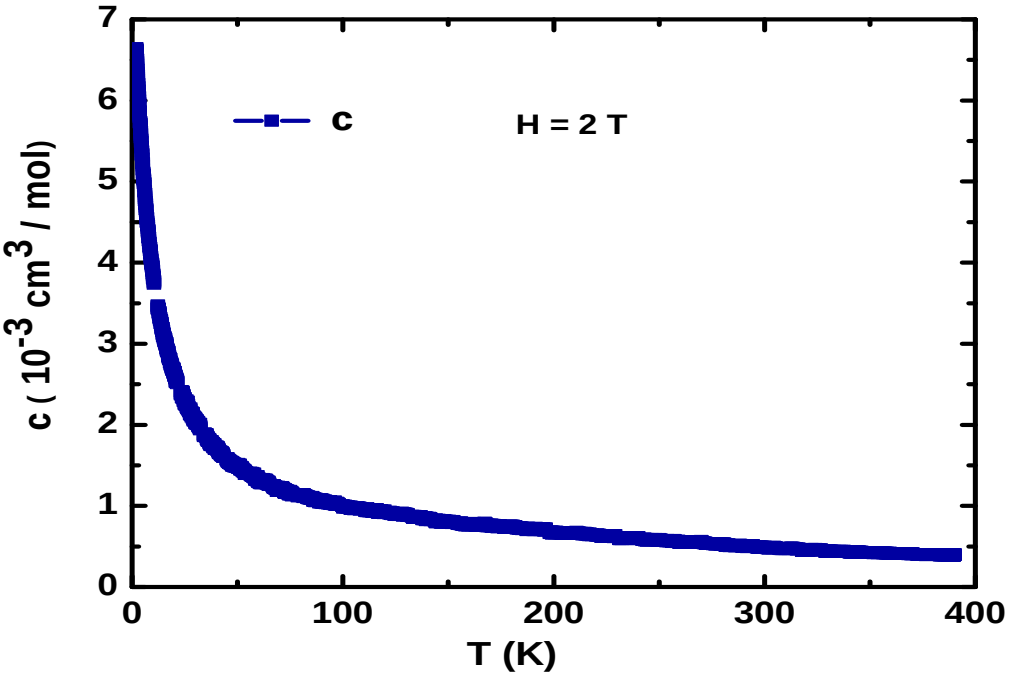

FIGURE 7.3: Magnetic susceptibility χ versus temperature T for K_2IrO_3 measured between $T = 1.8$ K and 395 K in an magnetic field of $H = 2$ T.

$-12 \times 10^{-6}) = -0.95 \times 10^{-4}\ cm^3/mol$]. The additional diamagnetic value of χ_0 found in experiments could be due to the diamagnetic contribution of the quartz sample holder. The large and negative $\theta = -200(6)$ K indicates strong antiferromagnetic exchange interactions between the localized moments. However, no signature of any magnetic order was observed down to the lowest temperature of our measurements $T = 1.8$ K. Thus, the magnetic susceptibility strongly points to the possibility of a quantum spin liquid state in K_2IrO_3.

7.5 Summary and Discussion

We have discovered a new material K_2IrO_3 and have successfully synthesized single crystals of the same. The structural determination studies show that K_2IrO_3 is built up of edge shared IrO_6 octahedra forming honeycomb layers in the *ab*-plane and these layers are stacked along the *c*-axis with honeycomb layers of K separating Ir layers. The new material has a much larger *c*-axis lattice parameter which matches our design goal of producing materials with a larger separation of iridium honeycomb layers. Measurements of the magnetic susceptibility indicate Mott insulating behaviour with localized $S = 1/2$ moment magnetism. An estimate of the Weiss temperature gave $\theta \approx -200$ K suggesting

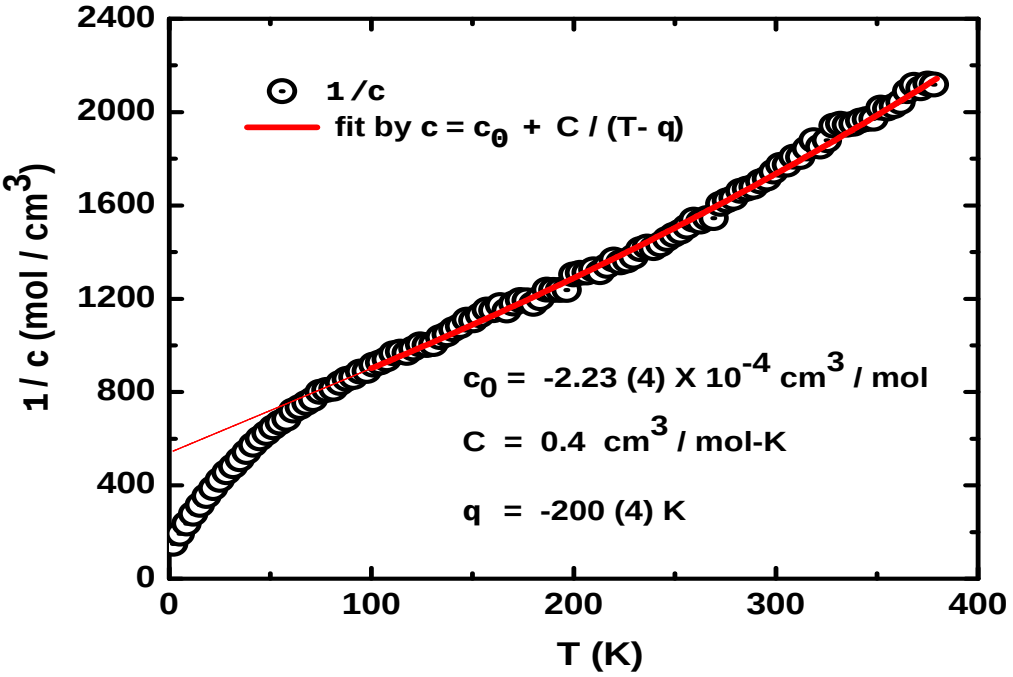

FIGURE 7.4: The $1/\chi(T)$ versus T data between $T = 1.8$ K and 380 K in a applied magnetic field $H = 2\ T$. The solid curves through the data are fits by the Curie-Weiss behavior and dashed curve is an extrapolated upto T = 0.

strong antiferromagnetic interactions. However, no signature of magnetic ordering was observed down to 1.8 K, a temperature smaller than $\theta/100$. This strongly points to the possibility of a quantum spin liquid state in this new material. The properties of this possible QSL phase and its relation to Kitaev's QSL will have to be explored in future measurements and on larger crystals and is left for the future. However, we reiterate that we have succeeded in discovering a new material which matches our design goals of maintaining the edge shared IrO_6 octahedra and the honeycomb layer geometry while increasing the separation between these honeycomb layers. Thus we expect this new material to be closer to the Kitaev limit and to exhibit QSL behaviour.

Chapter 8

Summary and Outlook

8.1 Summary

Kitaev-like bond-directional exchange interactions are novel and quite different from the ubiquitous Heisenberg interactions found in most magnets. These kind of interactions open up new possibilities in the exploration and designing of new quantum magnets which can host novel quantum ground states like spin-liquids. However, Kitaev-like interactions have remained only a theoretical construct until recently. Honeycomb iridates A_2IrO_3 (A = Na, Li), offer potential realizations of such novel exchange coupling. In this thesis I have synthesized single crystals of A_2TO_3 (A = Na, Li, K, and T = Ir, Ru) and studied their electrical transport, magnetic, and thermal properties. Our work provides several new results which we summarize below.

▶ Proximity of A_2IrO_3 to Kitaev's spin liquid state:- The Kitaev model has a spin liquid as its exact ground state. However, even though there is growing evidence that Kitaev-like interactions are present in the A_2IrO_3 materials, there seem to be additional isotropic Heisenberg interactions present as well. This leads to a long ranged ordered antiferromagnetic ground state for both materials instead of the spin liquid expected for the pure Kitaev model. So how near or far are the real materials to the Kitaev's spin liquid state? We address this problem by measuring and analyzing the temperature dependence of the magnetic heat capacity and entropy of the A_2IrO_3 materials. Our results provide the first thermodynamic evidence that A_2IrO_3 lie in close proximity to the spin liquid expected in the pure Kitaev limit.

► Range of magnetic exchange interactions and fragile magnetic order in A_2IrO_3:- The minimal Hamiltonian required to describe the observed magnetic properties of A_2IrO_3 materials is still under debate. In particular, the nature and range of magnetic interactions are still an open question. We have addressed the question about the range of magnetic interactions by performing partial magnetic impurity substitutions (Ru instead of Ir) in A_2IrO_3. We find that even for the smallest doping concentrations (5%), the long ranged magnetic order gives way to a spin-glass ground state. These results point to both the fragile nature of the magnetic order in the parent compound as well as the importance of nearest-neighbour exchange interactions is determining the magnetic properties of the parent compound A_2IrO_3.

► Tuning Na_2IrO_3 metallic by an unconventional doping technique:- There are several theoretical predictions of anomalous metallic properties including spin-triplet superconductivity and spin or charge density waves in the doped Kitaev-Heisenberg model relevant for the A_2IrO_3 materials. Conventional doping routes have failed to work for these materials and there are no successful doping studies so far. We succeeded in doping the surfaces of as-grown Na_2IrO_3 single crystals by high energy reactive ion etching. We were able to increase the conductivity of the samples by upto 11 orders of magnitude by varying the etching time. The metallic samples showed density wave like anomalies in transport measurements consistent with recent predictions. No superconductivity has thus far been observed down to 1.8 K.

► First order magneto-structural transition in single crystalline Li_2RuO_3:- We have synthesized the first single crystals of Li_2RuO_3 which crystallize at room temperature in the target $P2_1/m$ structure and show the expected high temperature magneto-structural transition. We are thus able to investigate for the first time the anisotropic properties of Li_2RuO_3 across this high temperature coupled transition. Our magnetic measurements between 2 and 1000 K reveal that the transition is first-order in nature and most likely occurs in two steps with the structural transition occurring first at a higher $T_d \simeq 570$ K and then drives the magnetic transition around $T_m \simeq 540$ K. The $\chi(T)$ behaviour above T_d is consistent with quasi-2-dimensional magnetism.

► Discovery of a new candidate Kitaev spin liquid material K_2IrO_3:- Although A_2IrO_3 materials are close to the pure Kitaev limit, both materials show magnetically ordered ground states and not the spin liquid expected in the pure Kitaev limit. Therefore, it is

of fundamental interest to design and discover new candidate materials. In this part we discuss our design strategy and demonstrate that we have successfully discovered a new material K_2IrO_3 which fulfills the structural design targets. The magnetic properties indeed point to the fact that we have a new spin liquid candidate.

8.2 Outlook

We hope that our work will enhance the understanding of the physics and magnetism in these intriguing materials. There are however several questions that remain unanswered about these materials. For example, (i) what is the sign of the Kitaev and Heinseberg interactions in the iridates, (ii) what is the origin of the broad Raman response in Na_2IrO_3, (iii) what are the detailed differences between the low energy spin Hamiltonians for Na_2IrO_3 and α–Li_2IrO_3, (iv) why is the insulating state in these iridates so robust against pressure and chemical doping, (v) why are the properties of the honeycomb lattice ruthenates A_2RuO_3 so different from the candidate Kitaev material α–$RuCl_3$, (vi) the potential spin liquid state in the newly discovered Kitaev material K_2IrO_3 needs to be studied in detail using microscopic probes and its relation to Kitaev's QSL needs to be determined.

We are sure that the above and many more questions will keep the community addicted to these fascinating materials for the foreseeable future.

Appendix A

Collaborative Work

In this appendix we briefly summarize highlights of other projects which have been done in collaboration with various groups.

A.1 Resonant X-Ray Scattering (RIXS) employed on single crystal of Na_2IrO_3

Honeycomb lattice iridates, A_2IrO_3 (A = Na, Li), are potential candidates for realization of Kitaev-like magnetic exchange interaction. Such bond-directional magnetic interactions are unusual and provide a novel route to a QSL in A_2IrO_3 (A= Na, Li). However, direct evidence of the same has remained elusive and so far they have remained a theoretical construct.

In collaboration with Prof. B. J. Kim's group at Max Planck Stuttgart, we performed diffuse magnetic x-ray scattering on Na_2IrO_3 single crystals. The results show strong broken spin rotational symmetry even above the magnetic ordering temperature, with the three spin components exhibiting nano-scale correlations along three different crystallographic directions. The direct evidence for predominant bond-directional interaction is revealed in Na_2IrO_3 via the measurement of equal time correlation of spin components above the magnetic ordering temperature. The spin-component separation in real space, and violation of the Goldstone theorem via the separation of long-wavelength spin waves provides direct evidence for dominant bond-directional interactions in Na_2IrO_3. These

observation establish a new route toward frustrated magnetism and provide direct connection between honeycomb lattice iridates and Kitaev physics. More details can be found in [10.1038/nphys3322] [13].

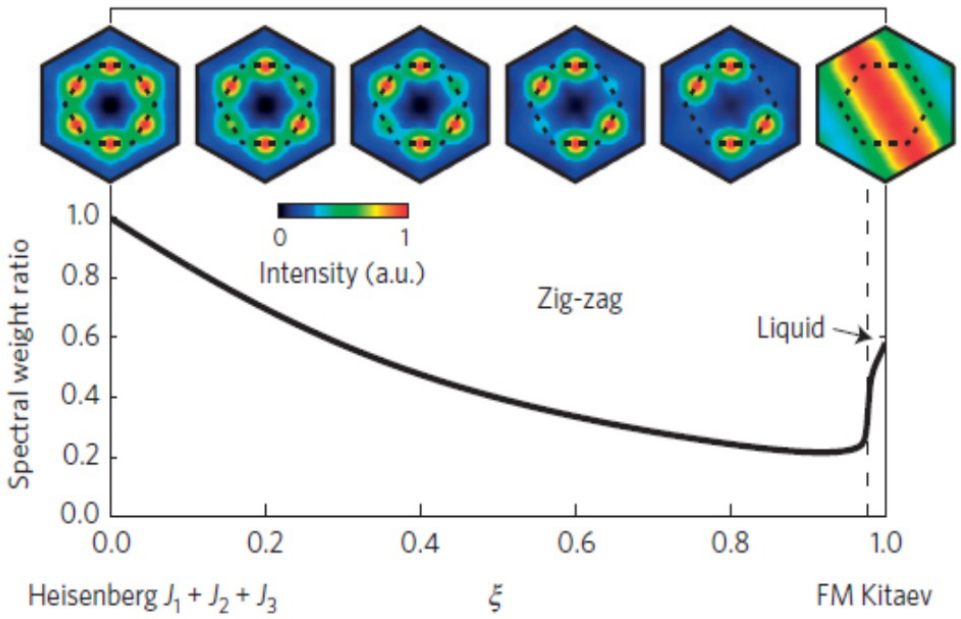

FIGURE A.1: "Simulation of spin component resolved correlation S_x as a function of the relative strength of Kitaev interaction strength. (From Ref.[13])".

A.2 Experiments and theory of Raman response in $(Na_{1-x}Li_x)_2IrO_3$

In collaboration with the group of Prof. A. K. Sood at IISC Bengaluru, we studied inelastic light scattering using Raman spectroscopy on freshly cleaved single crystals of $(Na_{1-x}Li_x)_2IrO_3$ ($x = 0, 0.05$ and 0.15). We observed a broad polarization independent broad band at ~ 2750 cm^{-1} with a large band-width ~ 1800 cm^{-1}. For Na_2IrO_3 the independent broad band is seen for temperatures $\leqslant 200$ K and persists inside the magnetically ordered state. Such response has recently been predicted (by Knolle et al.) [67] as a signature of the Kitaev spin liquid phase. The theory [67] also predicts a spike at low energies due to contributions of the "Z2-flux". At low energies however, several phonon peaks are observed in the experiments, making it impossible to disentangle any "Z2-flux" contribution unambiguously.

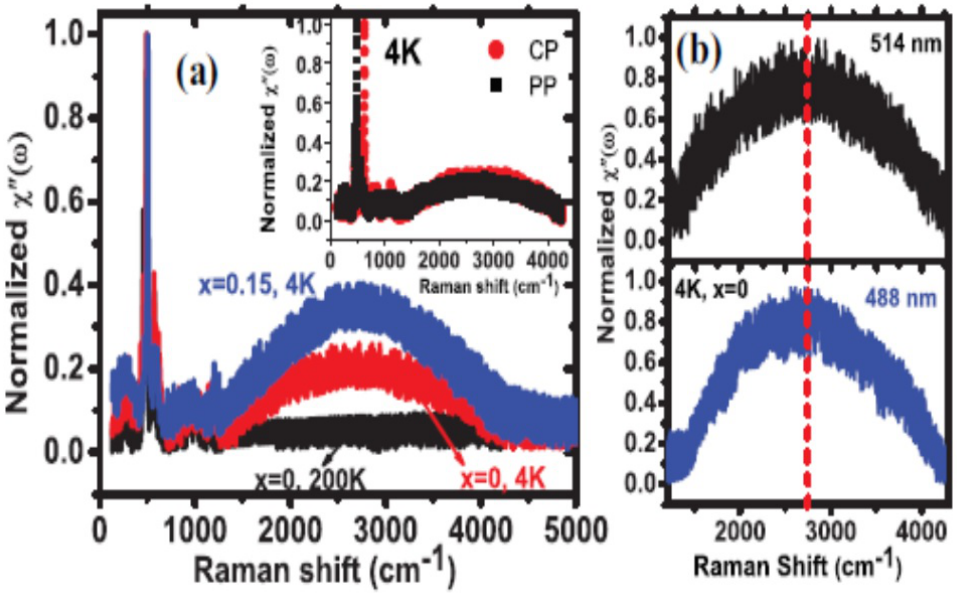

FIGURE A.2: "(a) Raman spectra of $(Na_{1-x}Li_x)_2IrO_3$ single crystals at 4K and 200K (for x = 0). Inset shows polarization dependence of the Raman spectra of Na_2IrO_3 at 4K. (b) BRB with two different laser lines 514 nm and 488 nm. The dashed line shows that BRB does not shift with change in lase wavelength. (From [14])".

The broad band was seen even inside the magnetically ordered state below T_N and suggest that dynamically fluctuating magnetic moments survive even below T_N. We compared experimental observation with mean-field calculation of the Raman response in the Kitaev-Heisenberg model with model parameters chosen to reproduce magnetic order found in the real material. The Raman response calculated in mean-field theory also support that the broad band predicted for the QSL state survives in the magnetically ordered state near the zigzag order–spin liquid phase boundary. A comparison with the theoretical model gives an estimate of the Kitaev exchange interaction parameter to be $J_K \approx 57$meV. More details can be found in [EPL, **114**, 47004 (2016).] [14].

A.3 High Pressure measurement on A_2IrO_3 (A= Na, Li)

The honeycomb lattice ruthenates and iridates are situated close to structural and magnetic instabilities. For example Li_2RuO_3 shows a novel magneto-structural transition involving dimerization and spin-singlet formation below 540 K. Since Li_2RuO_3 has smaller lattice parameters than A_2IrO_3 it would be interesting to ask whether A_2IrO_3 might also show such a magneto-structural transitions under pressure.

To this end, we have studied the structural properties under high pressure of the honeycomb lattice iridates A_2IrO_3 (A= Na, Li) in collaboration with the high pressure X-ray group at Tel Aviv University, Israel and Prof. Young-June Kim's group at the University of Toronto. The preliminary powder x-ray diffraction data on A_2IrO_3 (A = Na, Li) measured at room temperature at various pressures is shown in Figure A.3. We find that at pressures $\sim 3-4$ GPa both Na_2IrO_3 and Li_2IrO_3 show structural transitions very similar to the dimerized phase transition which occurs in Li_2RuO_3 [12].

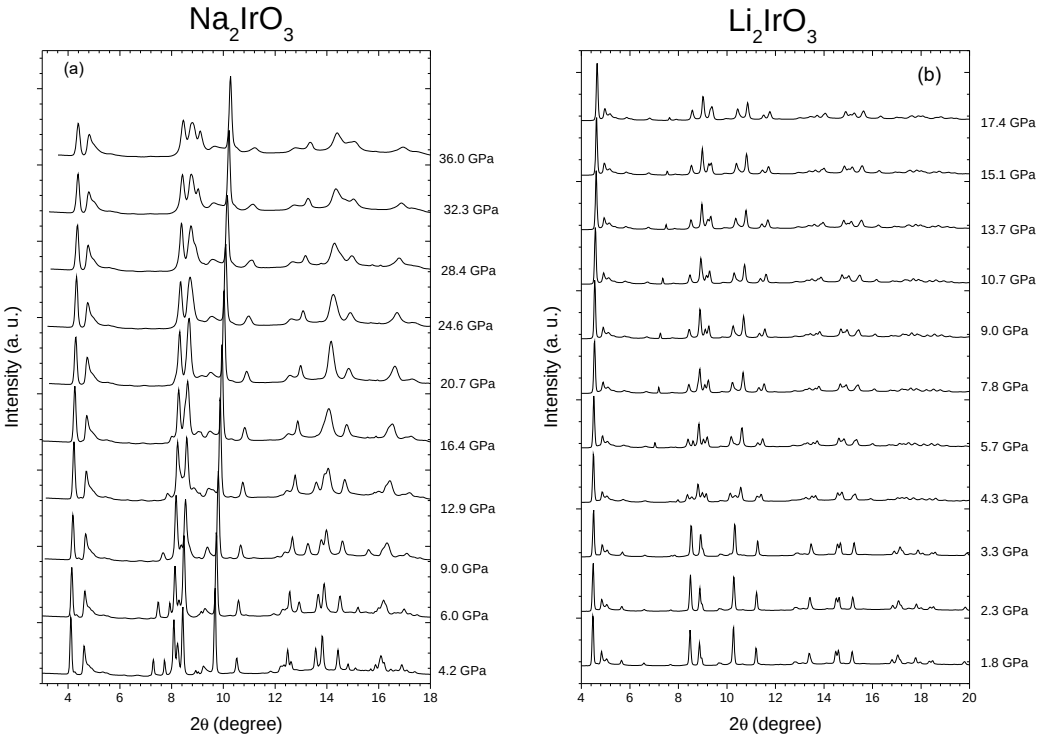

FIGURE A.3: High pressure x-ray diffraction data of (a) Na_2IrO_3 and (b) Li_2IrO_3 polycrystalline samples [15].

Bibliography

[1] Yogesh Singh and P. Gegenwart. Antiferromagnetic mott insulating state in single crystals of the honeycomb lattice material Na_2IrO_3. *Phys. Rev. B*, 82:064412, Aug 2010. URL http://link.aps.org/doi/10.1103/PhysRevB.82.064412.

[2] Feng Ye, Songxue Chi, Huibo Cao, Bryan C. Chakoumakos, Jaime A. Fernandez-Baca, Radu Custelcean, T. F. Qi, O. B. Korneta, and G. Cao. Direct evidence of a zigzag spin-chain structure in the honeycomb lattice: A neutron and x-ray diffraction investigation of single-crystal Na_2IrO_3. *Phys. Rev. B*, 85:180403, May 2012. URL http://link.aps.org/doi/10.1103/PhysRevB.85.180403.

[3] B. J. Kim, Hosub Jin, S. J. Moon, J.-Y. Kim, B.-G. Park, C. S. Leem, Jaejun Yu, T. W. Noh, C. Kim, S.-J. Oh, J.-H. Park, V. Durairaj, G. Cao, and E. Rotenberg. Novel $J_{\text{eff}} = 1/2$ mott state induced by relativistic spin-orbit coupling in Sr_2IrO_4. *Phys. Rev. Lett.*, 101:076402, Aug 2008. URL http://link.aps.org/doi/10.1103/PhysRevLett.101.076402.

[4] G. Jackeli and G. Khaliullin. Mott insulators in the strong spin-orbit coupling limit: From heisenberg to a quantum compass and kitaev models. *Phys. Rev. Lett.*, 102:017205, Jan 2009. URL http://link.aps.org/doi/10.1103/PhysRevLett.102.017205.

[5] Ji ří Chaloupka, George Jackeli, and Giniyat Khaliullin. Kitaev-heisenberg model on a honeycomb lattice: Possible exotic phases in iridium oxides A_2IrO_3. *Phys. Rev. Lett.*, 105:027204, Jul 2010. URL http://link.aps.org/doi/10.1103/PhysRevLett.105.027204.

[6] Ji ří Chaloupka, George Jackeli, and Giniyat Khaliullin. Zigzag magnetic order in the iridium oxide Na_2IrO_3. *Phys. Rev. Lett.*, 110:097204, Feb 2013. URL http://link.aps.org/doi/10.1103/PhysRevLett.110.097204.

[7] S. K. Choi, R. Coldea, A. N. Kolmogorov, T. Lancaster, I. I. Mazin, S. J. Blundell, P. G. Radaelli, Yogesh Singh, P. Gegenwart, K. R. Choi, S.-W. Cheong, P. J. Baker, C. Stock, and J. Taylor. Spin waves and revised crystal structure of honeycomb iridate Na_2IrO_3. *Phys. Rev. Lett.*, 108:127204, Mar 2012. URL http://link.aps.org/doi/10.1103/PhysRevLett.108.127204.

[8] G. Jackeli and D. I. Khomskii. Classical dimers and dimerized superstructure in an orbitally degenerate honeycomb antiferromagnet. *Phys. Rev. Lett.*, 100:147203, Apr 2008. URL http://link.aps.org/doi/10.1103/PhysRevLett.100.147203.

[9] Quantum design. physical property measurement system resistivity option user's manual, part number 1076-100a. technical report.

[10] Daniel D. Scherer, Michael M. Scherer, Giniyat Khaliullin, Carsten Honerkamp, and Bernd Rosenow. Unconventional pairing and electronic dimerization instabilities in the doped kitaev-heisenberg model. *Phys. Rev. B*, 90:045135, Jul 2014. URL http://link.aps.org/doi/10.1103/PhysRevB.90.045135.

[11] Alien space science news-wordpress.com.

[12] Yoko Miura, Yukio Yasui, Masatoshi Sato, Naoki Igawa, and Kazuhisa Kakurai. New-type phase transition of Li_2RuO_3 with honeycomb structure. *Journal of the Physical Society of Japan*, 76(3):033705, 2007. URL http://dx.doi.org/10.1143/JPSJ.76.033705.

[13] Sae Hwan Chun, Jong-Woo Kim, Jungho Kim, H. Zheng, Constantinos C. Stoumpos, C. D. Malliakas, J. F. Mitchell, Kavita Mehlawat, Yogesh Singh, Y. Choi, T. Gog, A. Al-Zein, M. Moretti Sala, M. Krisch, J. Chaloupka, G. Jackeli, G. Khaliullin, and B. J. Kim. Direct evidence for dominant bond-directional interactions in a honeycomb lattice iridate Na_2IrO_3. *Nature*, 11(6):462–466, 2015. ISSN 1745-2473. doi: 10.1038/nphys3322. URL http://dx.doi.org/10.1038/nphys3322.

[14] Satyendra Nath Gupta, P. V. Sriluckshmy, Kavita Mehlawat, Ashiwini Balodhi, D. K. Mishra, S. R. Hassan, T. V. Ramakrishnan, D. V. S. Muthu, Yogesh Singh, and A. K. Sood. Raman signatures of strong kitaev exchange correlations in $(Na_{1-x}Li_x)_2IrO_3$ experiments and theory. *Europhysics Letters*, 114:47004, 2016. URL http://stacks.iop.org/0295-5075/114/i=4/a=47004.

[15] J · P · Clancy and S · Layek private communication.

[16] Masatoshi Imada, Atsushi Fujimori, and Yoshinori Tokura. Metal-insulator transitions. *Rev. Mod. Phys.*, 70:1039–1263, Oct 1998. URL http://link.aps.org/doi/10.1103/RevModPhys.70.1039.

[17] Patrick A. Lee, Naoto Nagaosa, and Xiao-Gang Wen. Doping a mott insulator: Physics of high-temperature superconductivity. *Rev. Mod. Phys.*, 78:17–85, Jan 2006. URL http://link.aps.org/doi/10.1103/RevModPhys.78.17.

[18] Myron B. Salamon and Marcelo Jaime. The physics of manganites: Structure and transport. *Rev. Mod. Phys.*, 73:583–628, Aug 2001. URL http://link.aps.org/doi/10.1103/RevModPhys.73.583.

[19] M. R. Norman. *Colloquium* : Herbertsmithite and the search for the quantum spin liquid. *Rev. Mod. Phys.*, 88:041002, Dec 2016. URL http://link.aps.org/doi/10.1103/RevModPhys.88.041002.

[20] B. J. Kim, H. Ohsumi, T. Komesu, S. Sakai, T. Morita, H. Takagi, and T. Arima. Phase-sensitive observation of a spin-orbital mott state in Sr_2IrO_4. *Science*, 323 (5919):1329–1332, 2009. ISSN 0036-8075. URL http://science.sciencemag.org/content/323/5919/1329.

[21] H. Okabe, M. Isobe, E. Takayama-Muromachi, A. Koda, S. Takeshita, M. Hiraishi, M. Miyazaki, R. Kadono, Y. Miyake, and J. Akimitsu. Ba_2IrO_4: A spin-orbit mott insulating quasi-two-dimensional antiferromagnet. *Phys. Rev. B*, 83:155118, Apr 2011. URL http://link.aps.org/doi/10.1103/PhysRevB.83.155118.

[22] M. K. Crawford, M. A. Subramanian, R. L. Harlow, J. A. Fernandez-Baca, Z. R. Wang, and D. C. Johnston. Structural and magnetic studies of Sr_2IrO_4. *Phys. Rev. B*, 49:9198–9201, Apr 1994. URL http://link.aps.org/doi/10.1103/PhysRevB.49.9198.

[23] Jason S. Gardner, Michel J. P. Gingras, and John E. Greedan. Magnetic pyrochlore oxides. *Rev. Mod. Phys.*, 82:53–107, Jan 2010. URL http://link.aps.org/doi/10.1103/RevModPhys.82.53.

[24] Kai-Yu Yang, Yuan-Ming Lu, and Ying Ran. Quantum hall effects in a weyl semimetal: Possible application in pyrochlore iridates. *Phys. Rev. B*, 84:075129, Aug 2011. URL http://link.aps.org/doi/10.1103/PhysRevB.84.075129.

[25] Songrui Zhao, J. M. Mackie, D. E. MacLaughlin, O. O. Bernal, J. J. Ishikawa, Y. Ohta, and S. Nakatsuji. Magnetic transition, long-range order, and moment fluctuations in the pyrochlore iridate $Eu_2Ir_2O_7$. *Phys. Rev. B*, 83:180402, May 2011. URL http://link.aps.org/doi/10.1103/PhysRevB.83.180402.

[26] S. J. Moon, H. Jin, K. W. Kim, W. S. Choi, Y. S. Lee, J. Yu, G. Cao, A. Sumi, H. Funakubo, C. Bernhard, and T. W. Noh. Dimensionality-controlled insulator-metal transition and correlated metallic state in $5d$ transition metal oxides $Sr_{n+1}Ir_nO_{3n+1}$ ($n = 1$, 2, and ∞). *Phys. Rev. Lett.*, 101:226402, Nov 2008. URL http://link.aps.org/doi/10.1103/PhysRevLett.101.226402.

[27] Yoshihiko Okamoto, Minoru Nohara, Hiroko Aruga-Katori, and Hidenori Takagi. Spin-liquid state in the $s = 1/2$ hyperkagome antiferromagnet $Na_4Ir_3O_8$. *Phys. Rev. Lett.*, 99:137207, Sep 2007. URL http://link.aps.org/doi/10.1103/PhysRevLett.99.137207.

[28] Yogesh Singh, Y. Tokiwa, J. Dong, and P. Gegenwart. Spin liquid close to a quantum critical point in Na_2IrO_3. *Phys. Rev. B*, 88:220413, Dec 2013. URL http://link.aps.org/doi/10.1103/PhysRevB.88.220413.

[29] Dmytro Pesin and Leon Balents. Mott physics and band topology in materials with strong spin-orbit interaction. *Nature*, 6(5):376–381, 2015. ISSN 1745-2473. URL http://dx.doi.org/10.1038/nphys1606.

[30] Xiangang Wan, Ari M. Turner, Ashvin Vishwanath, and Sergey Y. Savrasov. Topological semimetal and fermi-arc surface states in the electronic structure of pyrochlore iridates. *Phys. Rev. B*, 83:205101, May 2011. URL http://link.aps.org/doi/10.1103/PhysRevB.83.205101.

[31] Alexei Kitaev. Anyons in an exactly solved model and beyond. *Annals of Physics*, 321(1):2 – 111, 2006. ISSN 0003-4916. URL http://www.sciencedirect.com/science/article/pii/S0003491605002381. January Special Issue.

[32] Hong-Chen Jiang, Zheng-Cheng Gu, Xiao-Liang Qi, and Simon Trebst. Possible proximity of the mott insulating iridate Na_2IrO_3 to a topological phase: Phase diagram of the heisenberg-kitaev model in a magnetic field. *Phys. Rev. B*, 83:245104, Jun 2011. URL http://link.aps.org/doi/10.1103/PhysRevB.83.245104.

[33] Atsuo Shitade, Hosho Katsura, Jan Kuneš, Xiao-Liang Qi, Shou-Cheng Zhang, and Naoto Nagaosa. Quantum spin hall effect in a transition metal oxide Na_2IrO_3. *Phys. Rev. Lett.*, 102:256403, Jun 2009. URL http://link.aps.org/doi/10.1103/PhysRevLett.102.256403.

[34] Yogesh Singh, S. Manni, J. Reuther, T. Berlijn, R. Thomale, W. Ku, S. Trebst, and P. Gegenwart. Relevance of the heisenberg-kitaev model for the honeycomb lattice iridates A_2IrO_3. *Phys. Rev. Lett.*, 108:127203, Mar 2012. URL http://link.aps.org/doi/10.1103/PhysRevLett.108.127203.

[35] H. Gretarsson, J. P. Clancy, X. Liu, J. P. Hill, Emil Bozin, Yogesh Singh, S. Manni, P. Gegenwart, Jungho Kim, A. H. Said, D. Casa, T. Gog, M. H. Upton, Heung-Sik Kim, J. Yu, Vamshi M. Katukuri, L. Hozoi, Jeroen van den Brink, and Young-June Kim. Crystal-field splitting and correlation effect on the electronic structure of A_2IrO_3. *Phys. Rev. Lett.*, 110:076402, Feb 2013. URL http://link.aps.org/doi/10.1103/PhysRevLett.110.076402.

[36] R. Comin, G. Levy, B. Ludbrook, Z.-H. Zhu, C. N. Veenstra, J. A. Rosen, Yogesh Singh, P. Gegenwart, D. Stricker, J. N. Hancock, D. van der Marel, I. S. Elfimov, and A. Damascelli. Na_2IrO_3 as a novel relativistic mott insulator with a 340-mev gap. *Phys. Rev. Lett.*, 109:266406, Dec 2012. URL http://link.aps.org/doi/10.1103/PhysRevLett.109.266406.

[37] Itamar Kimchi and Yi-Zhuang You. Kitaev-heisenberg-J_2-J_3 model for the iridates A_2IrO_3. *Phys. Rev. B*, 84:180407, Nov 2011. URL http://link.aps.org/doi/10.1103/PhysRevB.84.180407.

[38] S. Manni, Y. Tokiwa, and P. Gegenwart. Effect of nonmagnetic dilution in the honeycomb-lattice iridates Na_2IrO_3 and Li_2IrO_3. *Phys. Rev. B*, 89:241102, Jun 2014. URL http://link.aps.org/doi/10.1103/PhysRevB.89.241102.

[39] Vamshi M Katukuri, S Nishimoto, V Yushankhai, A Stoyanova, H Kandpal, Sungkyun Choi, R Coldea, I Rousochatzakis, L Hozoi, and Jeroen van den Brink.

Kitaev interactions between j = 1/2 moments in honeycomb Na_2IrO_3 are large and ferromagnetic: insights from ab initio quantum chemistry calculations. *New Journal of Physics*, 16(1):013056, 2014. URL http://stacks.iop.org/1367-2630/16/i=1/a=013056.

[40] Jeffrey G. Rau, Eric Kin-Ho Lee, and Hae-Young Kee. Generic spin model for the honeycomb iridates beyond the kitaev limit. *Phys. Rev. Lett.*, 112:077204, Feb 2014. URL http://link.aps.org/doi/10.1103/PhysRevLett.112.077204.

[41] X. Liu, T. Berlijn, W.-G. Yin, W. Ku, A. Tsvelik, Young-June Kim, H. Gretarsson, Yogesh Singh, P. Gegenwart, and J. P. Hill. Long-range magnetic ordering in Na_2IrO_3. *Phys. Rev. B*, 83:220403, Jun 2011. URL http://link.aps.org/doi/10.1103/PhysRevB.83.220403.

[42] K. W. Plumb, J. P. Clancy, L. J. Sandilands, V. Vijay Shankar, Y. F. Hu, K. S. Burch, Hae-Young Kee, and Young-June Kim. α-$RuCl_3$: A spin-orbit assisted mott insulator on a honeycomb lattice. *Phys. Rev. B*, 90:041112, Jul 2014. URL http://link.aps.org/doi/10.1103/PhysRevB.90.041112.

[43] M. Majumder, M. Schmidt, H. Rosner, A. A. Tsirlin, H. Yasuoka, and M. Baenitz. Anisotropic Ru^{3+} $4d^5$ magnetism in the α-$RuCl_3$ honeycomb system: Susceptibility, specific heat, and zero-field nmr. *Phys. Rev. B*, 91:180401, May 2015. URL http://link.aps.org/doi/10.1103/PhysRevB.91.180401.

[44] Yumi Kubota, Hidekazu Tanaka, Toshio Ono, Yasuo Narumi, and Koichi Kindo. Successive magnetic phase transitions in α-$RuCl_3$: Xy-like frustrated magnet on the honeycomb lattice. *Phys. Rev. B*, 91:094422, Mar 2015. URL http://link.aps.org/doi/10.1103/PhysRevB.91.094422.

[45] Heung-Sik Kim, Vijay Shankar V., Andrei Catuneanu, and Hae-Young Kee. Kitaev magnetism in honeycomb α-$RuCl_3$ with intermediate spin-orbit coupling. *Phys. Rev. B*, 91:241110, Jun 2015. URL http://link.aps.org/doi/10.1103/PhysRevB.91.241110.

[46] J. A. Sears, M. Songvilay, K. W. Plumb, J. P. Clancy, Y. Qiu, Y. Zhao, D. Parshall, and Young-June Kim. Magnetic order in α-$RuCl_3$: A honeycomb-lattice quantum magnet with strong spin-orbit coupling. *Phys. Rev. B*, 91:144420, Apr 2015. URL http://link.aps.org/doi/10.1103/PhysRevB.91.144420.

[47] Luke J. Sandilands, Yao Tian, Anjan A. Reijnders, Heung-Sik Kim, K. W. Plumb, Young-June Kim, Hae-Young Kee, and Kenneth S. Burch. Spin-orbit excitations and electronic structure of the putative kitaev magnet α-$RuCl_3$. *Phys. Rev. B*, 93:075144, Feb 2016. URL http://link.aps.org/doi/10.1103/PhysRevB.93.075144.

[48] A. Banerjee, C. A. Bridges, J.-Q. Yan, A. A. Aczel, L. Li, M. B. Stone, G. E. Granroth, M. D. Lumsden, Y. Yiu, J. Knolle, S. Bhattacharjee, D. L. Kovrizhin, R. Moessner, D. A. Tennant, D. G. Mandrus, and S. E.. Nagler. Proximate kitaev quantum spin liquid behaviour in a honeycomb magnet. *Nature*, 15(7):733–740, 2016. ISSN 1476-1122. URL http://dx.doi.org/10.1038/nmat4604.

[49] Stephen Blundell. Magnetism in condensed matter, oxford master esries in condensed matter physics.

[50] I. I. Mazin, Harald O. Jeschke, Kateryna Foyevtsova, Roser Valentí, and D. I. Khomskii. Na_2IrO_3 as a molecular orbital crystal. *Phys. Rev. Lett.*, 109:197201, Nov 2012. URL http://link.aps.org/doi/10.1103/PhysRevLett.109.197201.

[51] I. I. Mazin, S. Manni, K. Foyevtsova, Harald O. Jeschke, P. Gegenwart, and Roser Valentí. Origin of the insulating state in honeycomb iridates and rhodates. *Phys. Rev. B*, 88:035115, Jul 2013. URL http://link.aps.org/doi/10.1103/PhysRevB.88.035115.

[52] Kailash M. Mogare, Karen Friese, Wilhelm Klein, and Martin Jansen. Syntheses and crystal structures of two sodium ruthenates: Na_2RuO_4 and Na_2RuO_3. *Zeitschrift für anorganische und allgemeine Chemie*, 630(4), 2004. URL http://dx.doi.org/10.1002/zaac.200400012.

[53] J. C. Wang, J. Terzic, T. F. Qi, Feng Ye, S. J. Yuan, S. Aswartham, S. V. Streltsov, D. I. Khomskii, R. K. Kaul, and G. Cao. Lattice-tuned magnetism of $Ru^{4+}(4\,d^4)$ ions in single crystals of the layered honeycomb ruthenates Li_2RuO_3 and Na_2RuO_3. *Phys. Rev. B*, 90:161110, Oct 2014. URL http://link.aps.org/doi/10.1103/PhysRevB.90.161110.

[54] Yoko Miura, Masatoshi Sato, Youichi Yamakawa, Tatsuro Habaguchi, and Yoshiaki Ono. Structural transition of Li_2RuO_3 induced by molecular-orbit formation. *Journal of the Physical Society of Japan*, 78(9):094706, 2009. URL http://dx.doi.org/10.1143/JPSJ.78.094706.

[55] Kavita Mehlawat and Yogesh Singh. First-order magnetostructural transition in single crystals of the honeycomb lattice ruthenate Li_2RuO_3. *Phys. Rev. B*, 95:075105, Feb 2017. URL http://link.aps.org/doi/10.1103/PhysRevB.95.075105.

[56] Simon A. J. Kimber, I. I. Mazin, Juan Shen, Harald O. Jeschke, Sergey V. Streltsov, Dimitri N. Argyriou, Roser Valentí, and Daniel I. Khomskii. Valence bond liquid phase in the honeycomb lattice material Li_2RuO_3. *Phys. Rev. B*, 89:081408, Feb 2014. URL http://link.aps.org/doi/10.1103/PhysRevB.89.081408.

[57] Junghwan Park, Teck-Yee Tan, D. T. Adroja, A. Daoud-Aladine, Seongil Choi, Deok-Yong Cho, Sang-Hyun Lee, Jiyeon Kim, Hasung Sim, T. Morioka, H. Nojiri, V. V. Krishnamurthy, P. Manuel, M. R. Lees, S. V. Streltsov, D. I. Khomskii, and Je-Geun. Park. Robust singlet dimers with fragile ordering in two-dimensional honeycomb lattice of Li_2IrO_3. *Scientific Reports*, 6(25238), 2016. URL http://dx.doi.org/10.1038/srep25238.

[58] Marco-Polo Jimenez-Segura, Atsutoshi Ikeda, Shingo Yonezawa, and Yoshiteru Maeno. Effect of disorder on the dimer transition of the honeycomb-lattice compound Li_2RuO_3. *Phys. Rev. B*, 93:075133, Feb 2016. URL http://link.aps.org/doi/10.1103/PhysRevB.93.075133.

[59] A. Biffin, R. D. Johnson, I. Kimchi, R. Morris, A. Bombardi, J. G. Analytis, A. Vishwanath, and R. Coldea. Noncoplanar and counterrotating incommensurate magnetic order stabilized by kitaev interactions in γ- Li_2IrO_3. *Phys. Rev. Lett.*, 113:197201, Nov 2014. URL http://link.aps.org/doi/10.1103/PhysRevLett.113.197201.

[60] Itamar Kimchi, Radu Coldea, and Ashvin Vishwanath. Unified theory of spiral magnetism in the harmonic-honeycomb iridates α, β, and γ-Li_2IrO_3. *Phys. Rev.*

B, 91:245134, Jun 2015. URL http://link.aps.org/doi/10.1103/PhysRevB.91.245134.

[61] Youhei Yamaji, Takafumi Suzuki, Takuto Yamada, Sei-ichiro Suga, Naoki Kawashima, and Masatoshi Imada. Clues and criteria for designing a kitaev spin liquid revealed by thermal and spin excitations of the honeycomb iridate Na_2IrO_3. *Phys. Rev. B*, 93:174425, May 2016. URL http://link.aps.org/doi/10.1103/PhysRevB.93.174425.

[62] Kavita Mehlawat, G. Sharma, and Yogesh Singh. Fragile magnetic order in the honeycomb lattice iridate Na_2IrO_3 revealed by magnetic impurity doping. *Phys. Rev. B*, 92:134412, Oct 2015. URL http://link.aps.org/doi/10.1103/PhysRevB.92.134412.

[63] Hechang Lei, Wei-Guo Yin, Zhicheng Zhong, and Hideo Hosono. Structural, magnetic, and electrical properties of $Li_2Ir_{1-x}Ru_xO_3$. *Phys. Rev. B*, 89:020409, Jan 2014. URL http://link.aps.org/doi/10.1103/PhysRevB.89.020409.

[64] Kavita Mehlawat and Yogesh Singh. First-order density-wave-like transitions in surface-doped Na_2IrO_3. *Phys. Rev. B*, 94:041109, Jul 2016. URL http://link.aps.org/doi/10.1103/PhysRevB.94.041109.

[65] Kavita Mehlawat and Yogesh Singh. Density wave like transport anomalies in surface doped Na_2IrO_3. *AIP Advance*, 7, 2017.

[66] Z. V. Pchelkina, A. L. Pitman, A. Moewes, E. Z. Kurmaev, Teck-Yee Tan, D. C. Peets, Je-Geun Park, and S. V. Streltsov. Electronic structure of Li_2RuO_3 studied by lda and lda+dmft calculations and soft x-ray spectroscopy. *Phys. Rev. B*, 91:115138, Mar 2015. URL http://link.aps.org/doi/10.1103/PhysRevB.91.115138.

[67] J. Knolle, Gia-Wei Chern, D. L. Kovrizhin, R. Moessner, and N. B. Perkins. Raman scattering signatures of kitaev spin liquids in A_2IrO_3 iridates with A = Na or Li. *Phys. Rev. Lett.*, 113:187201, Oct 2014. URL http://link.aps.org/doi/10.1103/PhysRevLett.113.187201.

[68] R. A. West. Solid state chemistry and its applications. john wiley and sons. 1984.

[69] G. Dudley, K. Byrappa, V Prasad, and M. Dudley. Handbook of crystal growth. (springer).

[70] C. J Brice. Crystal growth processes john wiley and sons. 1986.

[71] Cullityl D. B. Element of x-ray diffraction, addison-wesley publishing company inc. 1978.

[72] Kittel C. Introduction to solid state physics, john wiley and sons ltd. 1996.

[73] C. A. Larson, Dreele, and B. R. Von. General structure analysis system (gsas). technical report, los alamos national laboratory,. 2000.

[74] EXPGUI. Graphical user interface for gsas. j. appl. crystallography. 34:210–2013.

[75] Simon Foner. Versatile and sensitive vibrating-sample magnetometer. *Review of Scientific Instruments*, 30, 1959.

[76] Quantum design. magnetic property measurement system manual, part number 1004-100a. technical report.

[77] Quantum design. physical property measurement system heat capacity option user's manual, part number 1085-150, h-1. technical report.

[78] K. T. Barron and G K. Heat capacity and thermal expansion at low temperatures.

[79] H. Gretarsson, J. P. Clancy, X. Liu, J. P. Hill, Emil Bozin, Yogesh Singh, S. Manni, P. Gegenwart, Jungho Kim, A. H. Said, D. Casa, T. Gog, M. H. Upton, Heung-Sik Kim, J. Yu, Vamshi M. Katukuri, L. Hozoi, Jeroen van den Brink, and Young-June Kim. Crystal-field splitting and correlation effect on the electronic structure of A_2IrO_3. *Phys. Rev. Lett.*, 110:076402, Feb 2013. URL http://link.aps.org/doi/10.1103/PhysRevLett.110.076402.

[80] Kateryna Foyevtsova, Harald O. Jeschke, I. I. Mazin, D. I. Khomskii, and Roser Valentí. Ab initio. *Phys. Rev. B*, 88:035107, Jul 2013. URL http://link.aps.org/doi/10.1103/PhysRevB.88.035107.

[81] Youhei Yamaji, Yusuke Nomura, Moyuru Kurita, Ryotaro Arita, and Masatoshi Imada. First-principles study of the honeycomb-lattice iridates Na_2IrO_3 in the presence of strong spin-orbit interaction and electron correlations. *Phys. Rev. Lett.*,

113:107201, Sep 2014. URL http://link.aps.org/doi/10.1103/PhysRevLett.113.107201.

[82] Yuriy Sizyuk, Craig Price, Peter Wölfle, and Natalia B. Perkins. Importance of anisotropic exchange interactions in honeycomb iridates: Minimal model for zigzag antiferromagnetic order in Na_2IrO_3. *Phys. Rev. B*, 90:155126, Oct 2014. URL http://link.aps.org/doi/10.1103/PhysRevB.90.155126.

[83] Zhanybek Alpichshev, Fahad Mahmood, Gang Cao, and Nuh Gedik. Confinement-deconfinement transition as an indication of spin-liquid-type behavior in Na_2IrO_3. *Phys. Rev. Lett.*, 114:017203, Jan 2015. URL http://link.aps.org/doi/10.1103/PhysRevLett.114.017203.

[84] Joji Nasu, Masafumi Udagawa, and Yukitoshi Motome. Thermal fractionalization of quantum spins in a kitaev model: Temperature-linear specific heat and coherent transport of majorana fermions. *Phys. Rev. B*, 92:115122, Sep 2015. URL http://link.aps.org/doi/10.1103/PhysRevB.92.115122.

[85] V. Hardy, S. Lambert, M. R. Lees, and D. McK. Paul. Specific heat and magnetization study on single crystals of the frustrated quasi-one-dimensional oxide $Ca_3Co_2O_6$. *Phys. Rev. B*, 68:014424, Jul 2003. URL http://link.aps.org/doi/10.1103/PhysRevB.68.014424.

[86] S. Manni. Synthesis and investigation of frustrated honeycomb lattice iridates and rhodates. Ph · D · thesis, (2014).

[87] F. Freund, S. C. Williams, R. D. Johnson, R. Coldea, P. Gegenwart, and A. Jesche. Single crystal growth from separated educts and its application to lithium transition-metal oxides. *Scientific Reports*, 6:35362, Oct 2016. URL http://dx.doi.org/10.1038/srep35362.

[88] P. N. Breznay, A. Ruiz, Alex Frano, Wenli. Bi, J. R. Birgeneau, D. Haskel, and G. James Analytis. Resonant x-ray scattering reveals possible disappearanca of magnetic order under hydrostatic presssure in the kitaev candidate γ- Li_2IrO_3. *arXiv*, 1703:00499v, Mar 2017. URL http://arXiv:1703.00499v.

[89] Eric C. Andrade and Matthias Vojta. Magnetism in spin models for depleted honeycomb-lattice iridates: Spin-glass order towards percolation. *Phys. Rev. B*,

90:205112, Nov 2014. URL http://link.aps.org/doi/10.1103/PhysRevB.90.205112.

[90] J. A. Mydosh. Spin glasses: An experimental introduction (taylor and francis, london/washington, dc, 1993. 1993.

[91] C. A. M. Mulder, A. J. van Duyneveldt, and J. A. Mydosh. Susceptibility of the Cu Mn spin-glass: Frequency and field dependences. *Phys. Rev. B*, 23, Feb 1981. URL http://link.aps.org/doi/10.1103/PhysRevB.23.1384.

[92] T. F. Qi, O. B. Korneta, L. Li, K. Butrouna, V. S. Cao, Xiangang Wan, P. Schlottmann, R. K. Kaul, and G. Cao. Spin-orbit tuned metal-insulator transitions in single-crystal $Sr_2Ir_{1-x}Rh_xO_4$ ($0 \leq x \leq 1$). *Phys. Rev. B*, 86:125105, Sep 2012. URL http://link.aps.org/doi/10.1103/PhysRevB.86.125105.

[93] Sujit Das, Jia Er Guo, and Krishanu Roychowdhuary. Doping effects on the magnetic frustration in the honeycomb iridates. *arxiv*, 2015. URL arxiv:1506.08279.

[94] Heung-Sik Kim, Choong H. Kim, Hogyun Jeong, Hosub Jin, and Jaejun Yu. Strain-induced topological insulator phase and effective magnetic interactions in Li_2IrO_3. *Phys. Rev. B*, 87:10, Apr 2013. URL http://link.aps.org/doi/10.1103/PhysRevB.87.165117.

[95] Yi-Zhuang You, Itamar Kimchi, and Ashvin Vishwanath. Doping a spin-orbit mott insulator: Topological superconductivity from the kitaev-heisenberg model and possible application to $(Na_{1-x}Li_x)_2IrO_3$. *Phys. Rev. B*, 86:085145, Aug 2012. URL http://link.aps.org/doi/10.1103/PhysRevB.86.085145.

[96] Timo Hyart, Anthony R. Wright, Giniyat Khaliullin, and Bernd Rosenow. Competition between d-wave and topological p-wave superconducting phases in the doped kitaev-heisenberg model. *Phys. Rev. B*, 85:140510, Apr 2012. URL http://link.aps.org/doi/10.1103/PhysRevB.85.140510.

[97] Satoshi Okamoto. Global phase diagram of a doped kitaev-heisenberg model. *Phys. Rev. B*, 87:064508, Feb 2013. URL http://link.aps.org/doi/10.1103/PhysRevB.87.064508.

[98] Tianhan Liu, Cécile Repellin, Benoît Douçot, Nicolas Regnault, and Karyn Le Hur. Triplet fflo superconductivity in the doped kitaev-heisenberg honeycomb model. *Phys. Rev. B*, 94:180506, Nov 2016. URL http://link.aps.org/doi/10.1103/PhysRevB.94.180506.

[99] X. Yao, J. M. Honig, T. Hogan, C. Kannewurf, and J. Spałek. Electrical properties of $NiS_{2-x}Se_x$ single crystals: From mott insulator to paramagnetic metal. *Phys. Rev. B*, 54:17469–17475, Dec 1996. URL http://link.aps.org/doi/10.1103/PhysRevB.54.17469.

[100] G. Gruener. Density waves in solids westview, boulder, co. 2000.

[101] G. R. Stewart. Heavy-fermion systems. *Rev. Mod. Phys.*, 56:755–787, Oct 1984. URL http://link.aps.org/doi/10.1103/RevModPhys.56.755.

[102] H. D. Yang, P. Klavins, and R. N. Shelton. Low-temperature physical properties of $R_5Ir_4Si_{10}$ (R =Dy, Ho, Er, Tm, and Yb) compounds. *Phys. Rev. B*, 43:7688–7694, Apr 1991. URL http://link.aps.org/doi/10.1103/PhysRevB.43.7688.

[103] Yogesh Singh, Dilip Pal, S. Ramakrishnan, A. M. Awasthi, and S. K. Malik. Phase transitions in $Lu_2Ir_3Si_5$. *Phys. Rev. B*, 71:045109, Jan 2005. URL http://link.aps.org/doi/10.1103/PhysRevB.71.045109.

[104] Yogesh Singh, R. Nirmala, S. Ramakrishnan, and S. K. Malik. Competition between superconductivity and charge-density-wave ordering in the $Lu_5Ir_4(Si_{1-x}Ge_x)_{10}$ alloy system. *Phys. Rev. B*, 72:045106, Jul 2005. URL http://link.aps.org/doi/10.1103/PhysRevB.72.045106.

[105] Giniyat Khaliullin. Excitonic magnetism in van vleck˘type d^4 mott insulators. *Phys. Rev. Lett.*, 111:197201, Nov 2013. URL http://link.aps.org/doi/10.1103/PhysRevLett.111.197201.

[106] S. C. Williams, R. D. Johnson, F. Freund, Sungkyun Choi, A. Jesche, I. Kimchi, S. Manni, A. Bombardi, P. Manuel, P. Gegenwart, and R. Coldea. Incommensurate counterrotating magnetic order stabilized by kitaev interactions in the layered honeycomb α- Na_2IrO_3. *Phys. Rev. B*, 93:195158, May 2016. URL https://link.aps.org/doi/10.1103/PhysRevB.93.195158.

[107] R. Coldea. Private communication.